Vigdis Olden

FE modelling of hydrogen induced stress cracking in 25% Cr duplex stainless steel

Thesis for the degree of Philosophiae Doctor

Trondheim, August 2008

Norwegian University of Science and Technology
Faculty of Engineering Science and Technology
Department of Engineering Design and Materials

NTNU
Norwegian University of
Science and Technology

NTNU
Norwegian University of Science and Technology

Thesis for the degree of Philosophiae Doctor

Faculty of Engineering Science and Technology
Department of Engineering Design and Materials

ISBN 978-82-471-8611-4 (printed ver.)
ISBN 978-82-471-8625-1 (electronic ver.)
ISSN 1503-8181

Doctoral theses at NTNU, 2008:129

Printed by NTNU-trykk

If we listened to our intellect, we'd never have a love affair.
We'd never have a friendship. We'd never go into business,
because we'd be cynical. Well, that's nonsense. You've got to jump off
cliffs all the time and build your wings on the way down.

-Ray Bradbury

Preface

This PhD has been performed within the project “Construction integrity – environmentally assisted fracture mechanics” at NTNU Department of Engineering Design and Materials and was initiated in May 2004. The work has also been closely linked with the international joint industry research projects “Hydrogen Induced Stress Cracking I, II and III” at SINTEF Materials and Chemistry.

Acknowledgements
To do a PhD study after the age of 40 is a blessing. However, before you can recognise this there are few obstacles to overcome. First there is this overwhelming sense that the challenge is just too big. Second, as you get older there is a growing reluctance towards changes in your life. You need also to be convinced that your children, who aren't really children any more, in fact do not need looking after 24 hours a day and that they also have a father must be kept in mind.

In a situation like this, there is great support from people that really do believe that you can make it and they do their best to convince you of the same. If their stubborn enough, then you gradually realise that this genuinely is the chance of your lifetime and that it would be foolish not to take it.

For this achievement I would like to thank my previous boss at SINTEF, Jack Ødegård, who presented me with this opportunity and supported me 100%. Then there is NTNU professor Christian Thaulow that managed to convince me that FE simulation using ABAQUS was a piece of cake. And then there is my husband Trond Inge who has been cheering me on for more than 25 years.

There are several people who have been crucial for the progress of my work. First and foremost; Torodd Berstad for implementing the user defined cohesive element in ABAQUS and for making it able to handle the influence of hydrogen. The possibility of just stepping by the office of my other colleagues at SINTEF Department of Applied Mechanics and Corrosion and at NTNU Department of Engineering Design and Materials cannot be underestimated. I would especially like to thank my office neighbour Erling Østby, who has this almost magical ability of giving a whole new perspective on things. I would also like to thank Mario Polanco Loria and Odd Magne Akselsen for clarifying topics related to cohesive elements and physical metallurgy and Professor Roy Johnsen for guidance on the electrochemical topics. Then there is once again my ever supporting supervisor Christian Thaulow who has given me the space to move, but also has got me back on track when needed. I would also like to show my deepest gratitude to Lisbeth Irene R. Støen, who cautiously carried out the SENT testing. Finally thanks to fellow PhD student Eric André Jenssen and master student Marit Øverland for working together with me on parts of the thesis. Thanks to you all!

Due to openness and financial support from the joint internationals research project HISC II and the NTNU project PETROMAKS there is an experimental part to this thesis. The possibility of being able to use test results and to perform testing for the verification of my simulations has been crucial as well as for the fracture investigation part of the thesis.

Editing and proofreading of papers and thesis is a tedious business and without the effort of my fellow authors and colleagues carefully reading, raising questions and making suggestions, it would have been hard to manage.

Finally, thanks to my family for the wonderful inspiration of having a life beyond the walls of SINTEF and NTNU, that contains everything but materials science and FE simulations.

CONTENTS

1 Introduction

1.1 Structure of the thesis

This thesis consists of four journal papers [1-4]. Additionally the results have been presented at three international conferences [5-7].

Paper 1 is a literature review and is a state of the art of the main topics of the thesis. Paper 2 presents the user defined cohesive elements and the first application in finite element (FE) models of notched tensile specimens with hydrogen influence. Paper 3 deals with the influence of element size and cohesive law (TSL) shape on the stress distribution and fracture. Finally paper 4 handles the influence of hydrogen from trapping due to plastic strain on a fatigue cracked tensile specimen model. All simulations are compared with laboratory test results.

Fig. 1 gives a schematically presentation of the main topics and results of the four papers and the development of the thesis from the first decision to use cohesive zone modelling to a final good fit with laboratory experiments. A summary of paper 1- 4 and some additional results and major trends are given in section 1.4 of the introduction.

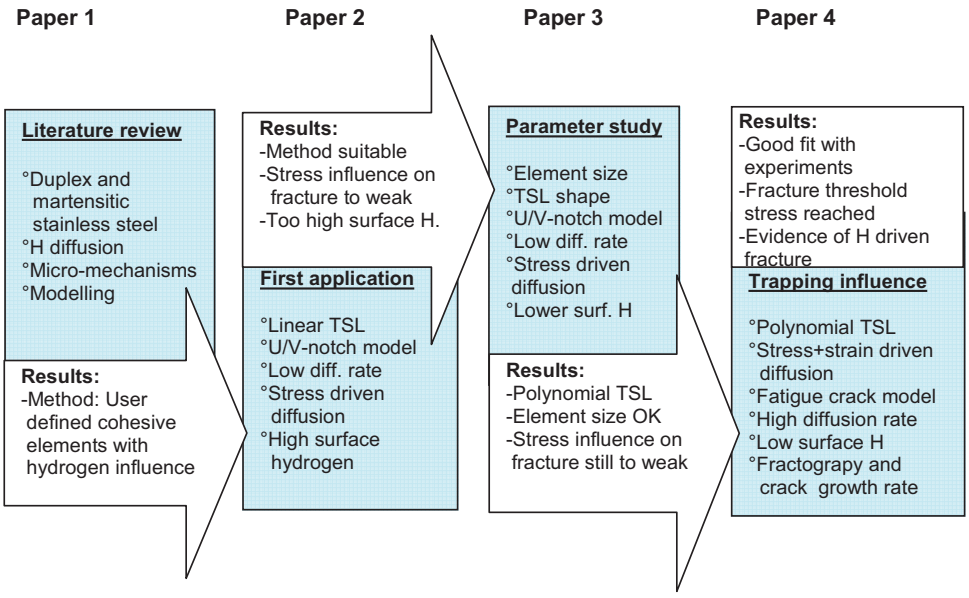

Fig. 1 Overview of papers and progress of Thesis.

1.2 Hydrogen induced stress cracking - HISC

Hydrogen embrittlement, in short HE is the most general term used for cracking influenced by hydrogen. The traditional definition of HE is that it requires the presence of hydrogen, stress and a sensitive microstructure to occur. This is the case also for HISC. However the HISC term is more frequently applied within the oil and gas community on hydrogen induced failures occurring subsea. The term usually implies a strong influence of the environment and load conditions. Fig. 2 gives an overview of different factors that can influence HISC fracture. Note that the HISC term does not include stress corrosion cracking in the presence of sulphide which implies that anodic dissolution takes place in the crack tip [7].

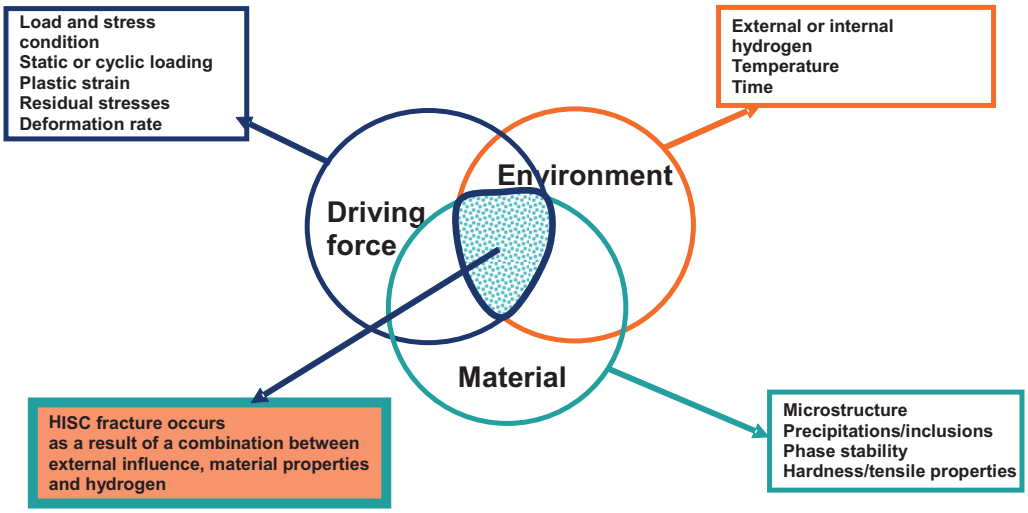

Fig. 2 Illustration of the definition of HISC

Stresses and strains typically originate from movements on the seabed, internal pressure or it can be thermo mechanically induced due to shut downs and re-start, however also residual stresses from welding and pipe laying can be involved. The environmental factor includes hydrogen and temperature. The external hydrogen is normally due to Cathodic Protection (CP) and the internal hydrogen originates from welding or steel manufacturing. Temperature influence is a "wild card" because it influences stress and strain conditions as well as the diffusion rate of hydrogen. Coarse microstructure, brittle precipitations and unstable residual austenite typically makes steel HISC sensitive. Regarding duplex stainless steel, high ferrite content and a coarse microstructure with large austenite spacing[1] is unfortunate [7]. Hydrogen diffusion in duplex stainless steel is slow; therefore HISC also is a relatively slow cracking process, which introduces the influence of time. Also the time factor in deformation rate plays a major role since the

[1] Large intermediate distance between the austenite phase islands

deformation rate influences the diffusion rate and trapping tendency of hydrogen. It is important to be aware of the interconnected relation between stress conditions, hydrogen and material properties. Hydrogen influences the internal condition of the material; stresses increase and microstructural changes occur which again influences the distribution and diffusion of hydrogen [9] .

1.3 Examples of HISC failures in duplex stainless steel

Duplex stainless steel (DSS) is often a preferred choice when a combination of high strength, good toughness and corrosion resistance is required. Typical applications offshore are oil and gas pipelines, pipeline connectors (hubs) and manifold/template pipings. Duplex stainless steels have traditionally been regarded a safe choice also in the presence of hydrogen, due to the high ductility and toughness of the austenite phase. However, HISC failures have occurred, which has given an increased focus on the safety of DSS. Fig. 3 shows an example of a failure from a forged 25%Cr duplex stainless steel hub with welded pipe connectors from the BP Amoco Foinaven Field [10]. A HISC crack occurred during service on the hub side close to the weld. The failure was due to stress concentration in the radii between the hub and the pipe and an unfortunate microstructure. In addition the hub was not coated. The microstructure had coarse elongated grains oriented through the wall thickness, giving reduced toughness as well as easy access of hydrogen from the CP system. Extremely large austenite spacings above 100µm were also found.

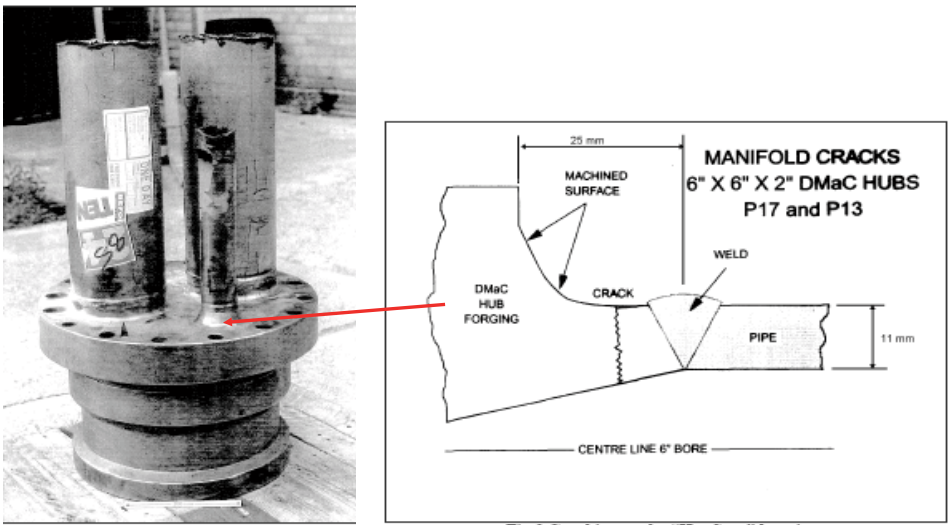

Fig. 3 Example of HISC failure in 25% Cr duplex stainless steel pipeline coupling (HUB) from the BP Amoco Foinhaven field. HISC cracking occurred on the hub side close to the weld in the radii between the hub and the pipe. The microstructure had coarse elongated grains oriented through the wall thickness, giving reduced toughness as well as easy access for hydrogen [10].

A similar HUB failure occurred at Shells Garn West field, where a circumferential crack was observed during start up after a planned production shut down [11]. As Fig. 4 shows the crack has initiated externally at a point of local high stress. The microstructure was coarse with austenite spacing in the range 50 – 100 μm. The incident caused a repair project that lasted 1 year and had a cost of 500 MNOK, where all 25% Cr duplex stainless steel hubs in a 200 ton subsea manifold were repaired or replaced [12].

These examples illustrate the importance of a fine grained microstructure and reducing local stress raisers when hydrogen is present.

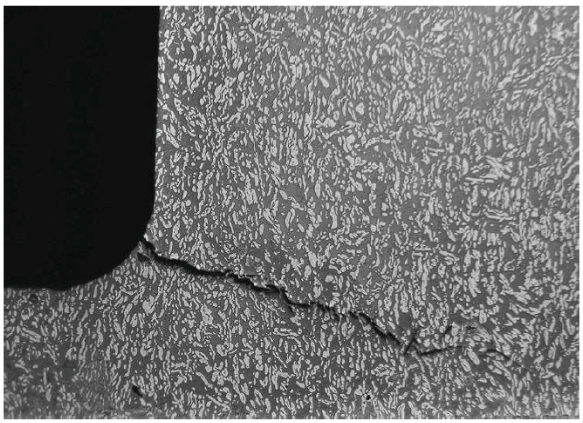

Fig. 4 HISC crack at the flange of a 25% Cr stainless steel HUB failed after a sequence of production shut down and start up [11].

1.4 Summary of papers 1 - 4

A note regarding the terms used for the material that is the objective of this work is called for. Whereas in the first paper the steel is named super duplex stainless steel or short SDSS, later papers applies the term 25%Cr duplex stainless steel. All terms are correct, but the last term is preferred and will be used also in this summary.

Paper 1 [1] is an introduction to hydrogen diffusion, micromechanical models of hydrogen assisted cracking and numerical modelling of the phenomenon. The topics are described in general and also more specifically related to supermartensitic, 22% Cr and 25% Cr duplex stainless steels. It is a literature review based on classical and newly published literature.

The mathematical basis for all diffusion processes are Fick's law. The basic equation as well as the modifications describing the influence of stress and strain rate on the hydrogen diffusion and trapping is presented. Theoretical aspects are supplemented with examples from published laboratory results.

Two micromechanical models for hydrogen assisted fracture are presented; the hydrogen enhanced decohesion model (HEDE) and the hydrogen enhanced local plasticity model (HELP). The HEDE model considers hydrogen assisted fracture as a result of reduced decohesion forces in the crack plane and focus on purely brittle mechanism. The HELP mechanism considers hydrogen as promoting local plasticity through enhanced dislocation mobility. The mechanisms are discussed and illustrated with reported laboratory observations.

Finally a new cohesive zone modelling approach to hydrogen cracking is presented. Special cohesive elements able to take transient changes in hydrogen content into account are discussed. Hydrogen fracture is modelled by reducing the required cohesive energy for fracture as a function of the hydrogen content. It is concluded that an approach by Serebrinsky et al. [13] is well suited for finite element simulations of hydrogen induced stress cracking and is chosen as a main tool in the further work of this thesis.

Paper 2 [2] describes the first application of user defined cohesive elements with hydrogen influence implemented in the FE code ABAQUS [14]. The FE models represent constant loaded U- and V-notched tensile specimens of 25%Cr duplex stainless steel in sea water with cathodic protection. The main objectives are to evaluate the implementation of the user defined elements and to establish the parameters for a bilinear cohesive law (maximum critical stress $\sigma(0)_c$ and maximum separation δ_c) best suited to reproduce results from laboratory experiments.

A diffusion coefficient for 25%Cr duplex stainless steel based on standardized electrochemical permeation measurements was applied. The chosen value represents a diffusion rate close to the diffusion rate in austenitic stainless steel which is very low, close to $1 \cdot 10^{-16}$ m^2/s. The applied sub surface hydrogen content was 40 ppm, based on uptake of hydrogen in the austenite phase as well as in the ferrite. The main results are summarized in Fig. 5.

The simulated time to fracture is within the time frame of the experiments. However, the simulations show less sensitivity to the stress level compared to the experiments. The main reason is the high surface hydrogen content. A surface hydrogen level of 40 ppm yields a critical cohesive surface stress well below the surface stress resulting from the applied load, regardless of the stress level. As a consequence the crack initiation process starts immediately when hydrogen is applied to the surface.

The fact that the fracture initiation starts at the surface and not at the stress peak in front of the notch is in itself an important result. The observation was confirmed by microscope investigation of not fractured tensile specimens containing surface microcracks in the ferrite phase at the notch surface. Simulation with hydrogen evenly distributed in the bulk material showed fracture initiation at the location of the stress peak, which is consistent with theory.

The cohesive parameters giving the best fit were: $\sigma(0)_c = 3.5 \cdot \sigma_y$ (2100 MPa) and $\delta_c = 0.0002$ mm giving a HISC fracture threshold stress intensity factor of 2.7 MPa$\sqrt{m}$.

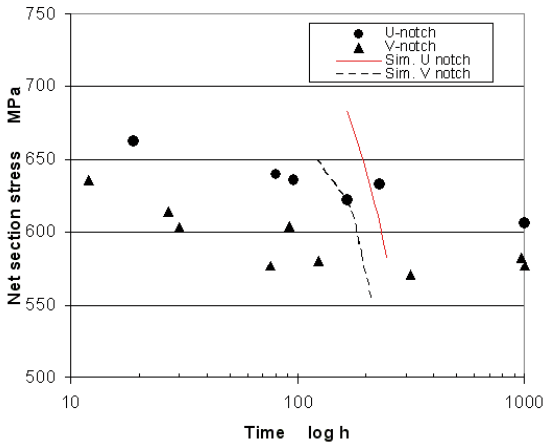

Fig. 5 Time to HISC fracture of U- and V-notched tensile specimens as a function of net section stress – laboratory and simulated results with 40 ppm surface hydrogen. The simulations with yield weak sensitivity to stress compared to the experiments [2].

In paper 3 [3] an evaluation of the influence of element size and shape of the cohesive law on the simulated results is presented. The same model system as described in paper 2 was applied. The investigated cohesive element lengths were 0.5µm, 5µm, 10µm and 20 µm. A bilinear and a polynomial shaped cohesive law were evaluated.

A surface hydrogen concentration of 10 ppm was applied, representing the maximum hydrogen level measured in ferrite steel [15]. Fig. 6 presents the main results regarding the influence of element size on the time to fracture in the cohesive simulations.

The most stable analyses and consistent results were obtained for element sizes of 0.5µm and 5 µm and a polynomial cohesive law. In more general terms the results suggest that an element size should be chosen in order to keep the resolution of the activated cohesive zone length (R/Δ) larger than 4.

Despite the lower hydrogen surface content of 10 ppm, the results did still not reflect the same stress sensitivity as the experiments. Additional simulations with 7 ppm gave some improvement indicating that the hydrogen content should be even lower to be able to obtain a lower bound stress level as reflected in the experimental results; see Fig. 7. 10 ppm hydrogen concentration yields a critical surface stress that is higher than in paper 2 but still well below the stress level in the U- and V- notches. The accompanying threshold stress intensity factor was 3.5 MPa$\sqrt{m}$.

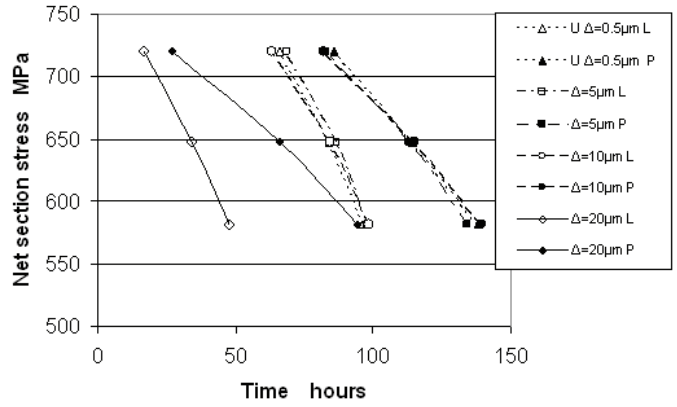

a)

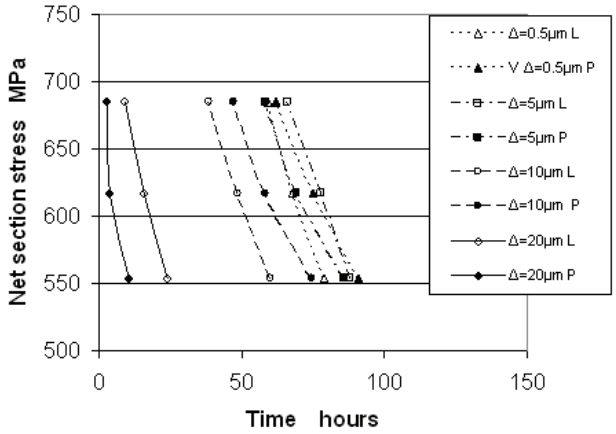

b)

Fig. 6 Time to fracture as a function of net section stress and element size a) U-notch b) V-notch. P and L denotes the polynomial and linear cohesive law. Element sizes of 0.5 and 5 µm yield consistent results for both geometries [3].

The experimental values used for comparison in paper 2 and 3 have a load history before the constant stress level reflected in Fig. 6 and Fig. 7 was reached. The stress was stepped up over a period of several days. To avoid the influence of the stepwise increasing load and diffusion history, the uploading of the constant load SENT specimens with a fatigue pre-crack described in the next paper was done continuously within half an hour.

Paper 4 [4] describes testing and simulation of SENT specimens under similar environment as the U- and V-notch testing. These specimens have a fatigue cracked notch and are the most severe of the three geometries regarding stress intensity at the notch tip. Fracture topography and microstructural investigations was performed in addition to calculation of the crack rate and the fracture threshold stress.

Three major modifications were implemented in the FE model. A higher diffusion coefficient was applied and the surface hydrogen was reduced to 1 ppm. The most influential modification was the implementation of trapping of hydrogen due to plastic strain based on work by Taha and Sofronis [16].

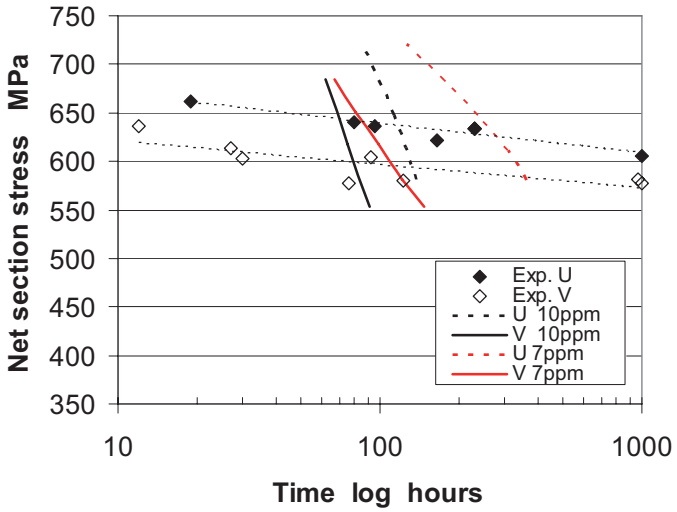

Fig. 7 Time to HISC fracture of U- and V-notched tensile specimens as a function of net section stress – comparison between laboratory and simulated results. The surface hydrogen is reduced to 10 and 7 ppm but the stress dependency is still too weak compared with experiments [3].

The trapping model implies that exceeding a plastic strain of about 2%, trapping has a dominating influence on the hydrogen concentration compared to the influence of stress. Since the plastic strain in the notch area is much higher than 2%, trapping totally dominated the hydrogen distribution. In the cohesive analyses the modifications now yielded high sensitivity to stress and also gave a lower bound stress level where fracture did not occur, see Fig. 8.

The lower bound is 480 MPa or 0.8% of the yield strength. Best fit to the experiments was obtained for the cohesive parameters $\sigma(0)_c$= 2200 MPa (~3.7· σ_y) and δ_c= 0.005 giving a threshold stress intensity of 20 MPa$\sqrt{m}$.

Calculations of the crack growth rate during experimental SENT-testing gave a linear dependency between stress level and crack growth rate, Fig. 9. The lowest crack growth rate was about two decades higher than the applied lattice diffusion rate. This and the fact that the fracture surfaces showed clear evidence of hydrogen presence suggests that stresses and strains at the crack tip increases the diffusion rate in the fracture process zone.

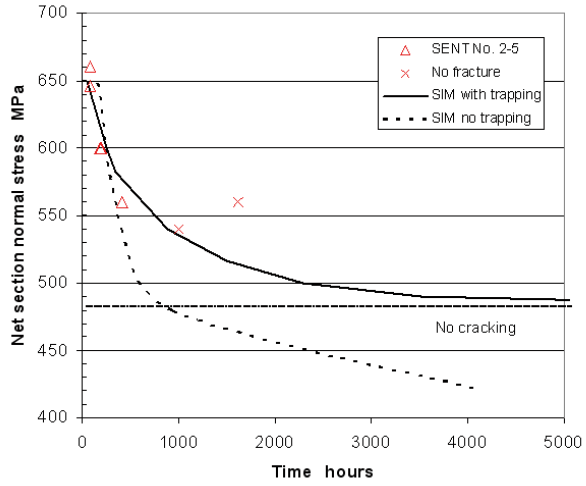

Fig. 8 Time to fracture, comparison between experiments and simulations including the influence of trapping due to plastic strain. Surface hydrogen is 1ppm. Suggested lower bound stress level which below simulated fracture initiation does not occur is 480 MPa [4].

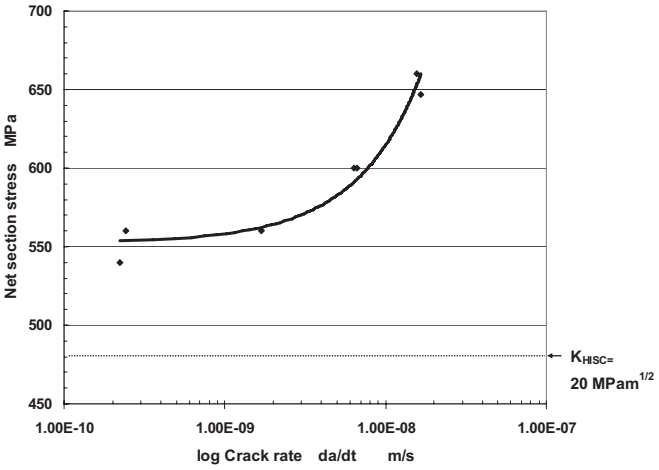

Fig. 9 Crack propagation rate calculated as a function of net section stress; the crack rate is much higher than the applied lattice diffusion rate of $3.7 \cdot 10^{-12}$ m/s suggesting that stress and plastic strain influence the diffusion rate in the fracture process zone. HISC induced fracture threshold stress intensity calculated from the cohesive analyses is 20 MPa$\sqrt{m}$ [4].

1.5 Additional results

To investigate the effect of trapping on the U- and V- notch models as well, a re-calculation simulating the step up loading procedure was performed. The details of these simulations are not included in the thesis papers but can be found in a separate conference paper [6]. Main findings are presented in Fig. 10. Good fit between time to fracture for experiments (lines) and simulations (squares and triangles) was now observed. Constant load simulations indicated that the net section stress should be kept below 580 MPa for the V-notch and below 620 MPa for the U-notch to avoid fracture. The applied cohesive parameters were $\sigma(0)_c = 2.5 \cdot \sigma_y$ for the U-notch, $3.5 \cdot \sigma_y$ for the V-notch and the critical opening was 0.001mm.

Based on the results presented in paper 4 and in Fig. 10 the critical net section stress can be plotted as a function of notch geometry, see Fig. 11. The notch geometry is normalized by dividing the notch radius by the net section specimen width (W-a), a being the notch depth. This figure is not presented in the journal papers and can be regarded as summary of the results regarding the susceptibility of HISC cracking of 25% Cr duplex stainless steel with different levels of constraint under the applied environmental conditions.

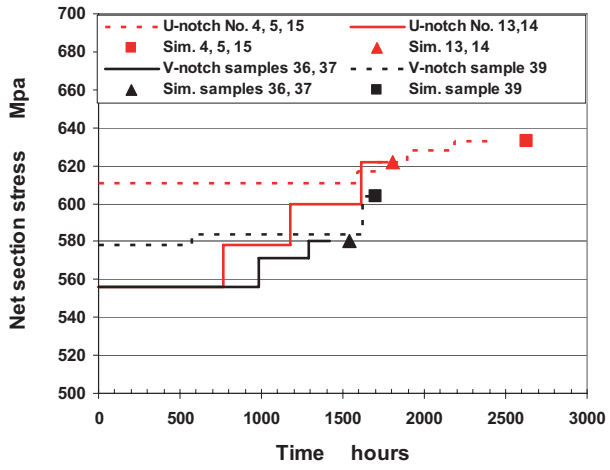

Fig. 10 Time to fracture vs. stepwise increasing net section stress for laboratory experiments and simulations. The simulations followed the same load history as the experiments. Fracture initiation of simulations is denoted with squares and triangles while the end of the curves represents fracture in the laboratory specimens [6].

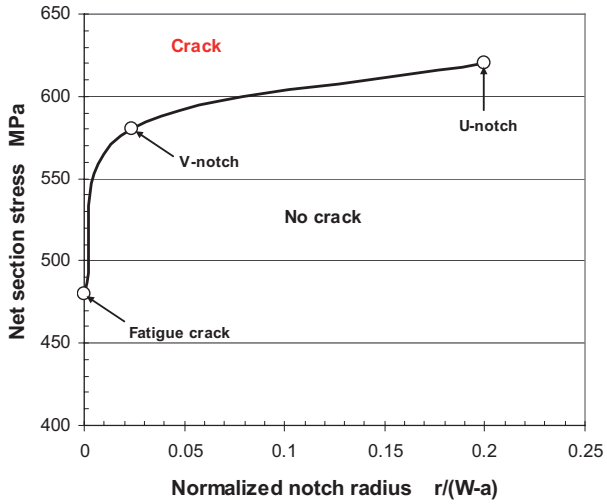

Fig. 11 Critical net section stress for initiation of HISC as a function of notch geometry for 25% Cr duplex stainless steel in synthetic sea-water with a CP potential of -1050 mV_{SCE} and T = 4°C.

References:

[1] Olden, V., Thaulow, C., Johnsen R., Modelling of hydrogen diffusion and hydrogen induced cracking in supermartensitic and duplex stainless steel, accepted for publication in Materials and Design, 2008

[2] Olden, V., Thaulow, C., Johnsen, R. Østby, E., Cohesive zone modeling of hydrogen-induced stress cracking in 25% Cr duplex stainless steel, Scripta Materialia 57, 2007, p. 615-618.

[3] Olden, V., Thaulow, C., Johnsen, R., Østby, E., Berstad, T., Application of hydrogen influenced cohesive laws in the prediction of hydrogen induced stress cracking in 25%Cr duplex stainless steel, Engineering Fracture Mechanics, 75 (8), 2008, p. 2333-2351

[4] Olden, V., Thaulow, C., Johnsen, R., Østby, E., Berstad, T., Influence of hydrogen from cathodic protection on the fracture susceptibility of 25%Cr duplex stainless steel – constant load SENT testing and FE-modelling using hydrogen influenced cohesive zone elements, submitted to Engineering Fracture Mechanics for review, 09.04.2008.

[5] Olden, V., Thaulow, C., Johnsen, R., Østby, E., A cohesive zone modelling approach to hydrogen induced stress cracking in 25%Cr duplex stainless steel, in proceedings of OMAE 2007, San Diego, California, June 10-15, 2007, paper no OMAE2007-29194.

[6] Olden, V., Thaulow, C., Østby, E., Berstad, T., Nyhus, B., Influence of hydrogen from CP on the fracture susceptibility of 25%Cr duplex stainless steel – FE modeling of constant load testing using hydrogen influenced cohesive zone elements, in proceedings of ISOPE 2008, Vancouver, Canada, July 6-11, 2008, paper no. ISOPE-2008-TPC-341.

[7] Olden, V., Thaulow C., Johnsen R., Hydrogen induced stress cracking in 25% Cr duplex stainless steel simulated using cohesive zone modelling, In proceedings of: 2008 International Hydrogen Conference, Effects of Hydrogen on Materials, September 7-10, 2008, Jackson Lake Lodge, Grand Teton National Park, Wyoming, USA

[8] Cassagne, T., Busschaert F., A review oh hydrogen embrittlement of duplex stainless steels, in proceedings of NACE2005, Paper no. 05098

[9] Comprehensive Structural Integrity- Fracture of materials from Nano to Macro, Vol. 6, Elsevier (2003) p. 65-101

[10] Taylor, T.S., Pendington, T. Bird, R., Foinaven Super Duplex Materials Cracking Investigation, In conference proceedings of Offshore Technology Conference (OTC), Houston Texas, 1999, paper 10965

[11] Huitzinga, S., McLoughlin, B., Hannah, I.M., Paterson, S.J. and Snedden, B.N.W., Failure of a subsea super duplex manifold hub by HISC and implications for design, in proceedings of NACE2006, Paper no. 06145

[12] Bill Snedden, Shell: "Garn West Repair Project - HISC of subsea components", presented during HISC2 meeting in Oslo, September 21st 2004.

[13] Serebrinsky, S., Carter, E. A., Ortiz, M., A quantum-mechanically informed continuum model of hydrogen embrittlement, Journal of Mechanics Physics and Solids, 52, 2004, p. 2403-2430

[14] ABAQUS Standard, Version 6.5, ABAQUS Inc., 2004

[15] Grong, Ø., Metallurgical Modelling of Welding -2nd edition, The institute of Materials, 1997

[16] Taha, A. and Sofronis, P., A micromechanics approach to the study of hydrogen transport and embrittlement, Engineering Fracture Mechanics 68 , 2001, p. 803-837

Paper I

MODELLING OF HYDROGEN DIFFUSION AND HYDROGEN INDUCED CRACKING IN MARTENSITIC AND DUPLEX STAINLESS STEELS

V. Olden [1, 2], C. Thaulow[1], R. Johnsen[1]

[1]Department of Engineering Design and Materials, Norwegian University of Science and Technology, 7465 Trondheim, Norway [2]Department of Applied Mechanics and Corrosion, SINTEF Materials and Chemistry, 7465 Trondheim, Norway

Abstract

This is a review based on classic and recent published literature regarding hydrogen diffusion and hydrogen assisted cracking in stainless steels. The majority of the reviewed literature is related to supermartensitic, duplex and super duplex stainless steels. Recent models for hydrogen diffusion and hydrogen assisted fracture in the presence of sharp notches are presented and discussed. New approaches in cohesive FE modelling of hydrogen assisted cracking are presented as a possible method for building a bridge between the modelling of micro mechanisms in the fracture process zone and the global fracture response.

Keywords: stainless steels, hydrogen, diffusion, fracture, modelling, cohesive zone

1 Introduction

The occurrence of cracks in offshore structures and pipelines can cause catastrophic failures. Over the last years several incidents of hydrogen induced failure have been reported in sub sea oil and gas pipelines and installations in the North Sea. The main hydrogen sources are cathodic protection and hydrogen in weld metal.

Hydrogen induced stress cracking from cathodic protection is a result of interconnected mechanisms involving electrochemistry, diffusion, metallurgy, micro mechanisms and external load.

Local stress and strain concentrations in notches as well as residual stresses after welding cause local accumulation of hydrogen. For austenitic and duplex stainless steels the bulk hydrogen content can be measured with reasonable accuracy with established methods like e.g. melt extraction. It has however proven difficult to establish experimental methods for measurement of local hydrogen concentration. Up to the present date the hydrogen assisted local fracture mechanisms in the vicinity of a crack are not well understood either.

Numerical modelling of hydrogen diffusion and hydrogen assisted cracking is thus an alternative method of investigation. By modifications of Fick's law the effect of different parameters on the time dependant hydrogen distribution can be investigated. The local hydrogen dependant fracture toughness can be calculated from the local hydrogen concentration. One of the most attractive approaches is offered by using cohesive zone modelling.

An introduction to supermartensitic and duplex stainless steels is given in Chapter 2. In Chapter 3, available models for hydrogen diffusion will be presented. Chapter 4 gives

an overview of reported diffusion coefficients for selected steels as well as methods for the calculation of the material specific diffusion coefficient. Micromechanical models of hydrogen induced cracking is presented in Chapter 5. Finally in Chapter 6 some recent approaches in FE modelling of hydrogen assisted fracture, with focus on cohesive element simulation are presented.

2 Materials

This chapter presents chemical composition, mechanical properties and microstructure of duplex (DSS), super- duplex (SDSS) and supermartensitic (SMSS) stainless steels.

2.1 Duplex and super duplex stainless steels

DSS and SDSS have been used in offshore applications for many years. These steels offer high strength and toughness as well as excellent corrosion resistance. The steels are characterized by the two phase microstructure of ferrite (α) and austenite (γ), Figure 1. To maintain the mechanical and corrosion properties it is essential to have a dual phase structure as close to the 50/50 percentage distribution as possible. This can often be a challenge, especially in welds where the brittle ferritic structure tends to dominate. According to NORSOK M630 ferrite content in the range 35-55 percent is acceptable for base metal and 35-65 percent for weld metal [1]. Reported chemical compositions of commercial DSS and SDSS are presented in Table 1.

The yield strength is normally in the range 450 – 600 MPa for DSS and 550 – 700 MPa for SDSS with the tensile strength above 620 MPa for DSS and 750 for SDSS.

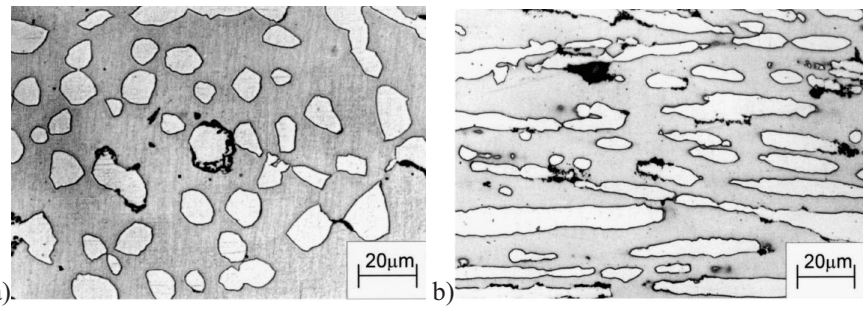

a). b)

Figure 1 Microstructure of a SDSS (H25N5M), γ = white, α = grey a) transverse direction b) longitudinal direction [2].

Despite its general superior toughness and corrosion resistance, DSS and SDSS can suffer from hydrogen embrittlement. It is a well known fact that hydrogen cracking can occur in the heat affected zone after welding. The susceptibility of hydrogen sulphide cracking in the weld root of oil and gas pipes is well documented. Over the last years also cracking incidents related to cathodic protection (CP) and hydrogen induced stress cracking (HISC) have been reported.

Table 1 Chemical composition of DSS and SDSS.

Material	Chemical composition (wt %)											
	C	Si	Mn	P	S	Ni	Cr	Mo	Cu	W	V	N
Sandvik SAF 2205 [2]	<0.03	<1.0	<2.0	<0.03	<0.015	5	22	3.2	-	-	-	0.18
Sandvik SAF2507 [3]	0.018	0.21	0.40	0.018	0.001	7.4	24.9	3.9	-	-	-	0.28
H25N5M [4] [3]	0.04	0.51	1.46	0.038	0.024	5.6	24.9	1.4	0.23	0.11	0.09	-
X2CrNi MoN 25-7-4 [4]	0.018 - 0.026	0.29 - 0.47	1.18-1.34	0.018 - 0.027	.001	6.00 - 6.85	24.7 - 25.4	2.73 - 3.02	0.11 - 0.16	-	-	0.157 - 0.226

2.2 Supermartensitic stainless steel

Low carbon martensitic stainless steels are an economical option to the demand for high strength and corrosion performance offshore. The steels offer sufficient corrosion resistance for sweet and mildly sour environment, but will suffer corrosion under sour conditions.

SMSS are a new generation of the classical 13%Cr martensitic steels, lower in carbon and with additional alloying of nickel and molybdenum offering better weldabilty and low temperature toughness. The alloying with nickel depresses the Ac1-temperature. This can be utilized in tempering treatment just above Ac1, giving partly reaustenization without transformation to martensite. The result is fine dispersed temperature and stable retained austenite between the martensite laths offering enhanced ductility and toughness. Dependent on the tempering cycle the percentage of retained austenite can vary in the range of 5 – 30 %. High tempering temperatures (well above the Ac1) should be avoided due to the formation of unstable austenite [5]. The microstructure of a SMSS with 29 % retained austenite is presented in Figure 2.

SMSS are divided into three alloy grades, lean, medium and high [6]. The high alloy grade has the lowest martensite transformation start temperature M_s (~200°C) and hence, the most stable retained austenite. Examples of chemical compositions of the three grades are presented in Table 2.

Mechanical properties will vary with chemical composition and tempering procedures. The yield strength is in the range Re=550-650 MPa and the tensile strength Rm ≈ 850 MPa [3].

Due to its primary martensitic structure the SMSS are susceptible to hydrogen embrittlement both related to welding, H_2S and CP. The steels are especially sensitive in the non-heat-treated condition, containing untempered martensite and unstable retained austenite. This is often the case in weld heat affected zones, where most of the hydrogen assisted cracking incidents occur.

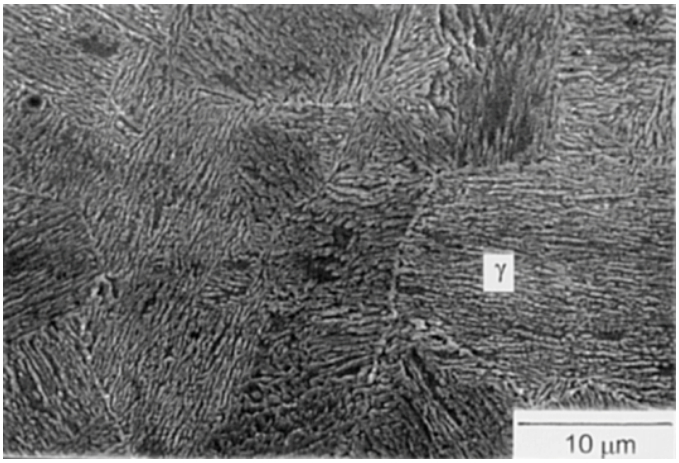

Figure 2 SEM micrograph of retained (white) austenite between martensite laths in SMSS. The austenite content is 29 percent as a result of two-stage tempering, Re=638 MPa [5].

Table 2 Chemical composition of supermartensitic stainless steels [6].

Element	Alloy grade		
	11Cr2Ni (lean)	**12Cr4.5Ni1.5Mo (medium)**	**12Cr6.5Ni2.5Mo (high alloyed)**
C (max.%)	0.015	0.015	0.015
Mn (max.%)	2.0	2.0	2.0
P (max.%)	0.030	0.030	0.030
S (max.%)	0.002	0.002	0.002
Si (max.%)	0.4	0.4	0.4
Cu (max.%)	0.2-0.6	0.2-0.6	0.2-0.6
Ni (%)	1.5-2.5	4.0-5.0	6.0-7.0
Cr (%)	10.5-11.5	11.0-13.0	11.0-13.0
Mo (%)	0.1	1.0-2.0	2.0-3.0
N (max.%)	0.012	0.012	0.012

3 Hydrogen diffusion

Lattice diffusion by interstitial jumps is the main diffusion mechanism for hydrogen in steel. A ferritic base centred cubic (bcc) structure enables a high diffusion rate and a low solubility due to its open lattice structure. In contrast, the austenitic face centred cubic (fcc) structure gives a lower diffusion rate and a higher solubility due to its close packed lattice. Martensite is basically body centred tetragonal (bct), but a tendency of hexagonal martensite formation (hcp) increases with the carbon content. These structures are closer packed than bcc. As a result the diffusion rate of hydrogen in martensite is between ferrite and austenite. The lattice diffusion coefficient D can be described by relations of the Arrhenius form:

$D = D_0 \exp(-E/RT)$ (1)

where E is the activation energy (J/mol) and R is the gas constant (8.314J/molK) and T the temperature in Kelvin. Fast [7] reports values for D_0 in the range 0.076 - 0.22 mm^2/s for ferrite and in the range 1.1-1.5 mm^2/s for austenite. The related activation energy for lattice diffusion is given as 12.5 J/mol for ferrite and about 42 J/mol for austenite. (Additional reported diffusion coefficients for iron are presented in Table 4.)

Fick's first law describes the diffusion of hydrogen (the flux of hydrogen atoms) from a region with high concentration to one with low concentration:

$$J_x = -D \cdot (\nabla C)_t \quad (2)$$

$(\nabla C)_t$ is the concentration gradient at a specific time t.

In ideal metals without trapping the transient (time dependant) diffusion process is described by Fick's second law[1]:

$$\frac{\partial C}{\partial t} = D\left[\frac{\partial^2 C}{\partial x^2} + \frac{\partial^2 C}{\partial y^2} + \frac{\partial^2 C}{\partial z^2}\right] \quad (3)$$

Solution of Fick's second law is the main basis for calculation of the distribution of hydrogen (or other interstitial elements) in metals. Analytical solutions of the equation can be handled for uniaxial diffusion. The solutions are also dependent on the initial and final concentrations and input data for the diffusion coefficients. The one dimensional (1D) form of Fick's second law is:

$$\frac{\partial C}{\partial t} = D\frac{\partial^2 C}{\partial x^2} \quad (4)$$

Crank [8] has published solutions of Eq. 4 for a range of boundary conditions provided that the diffusion coefficient is constant. In the following three solutions of the 1D Fick's second law will be presented.

3.1 The thick plate solution

The assumption for the thick plate solution is that the exit side conditions have marginal or no influence on the hydrogen concentration. A practical example would be slow diffusion of external hydrogen into a thick wall or pipe section. The thick plate solution for constant surface hydrogen concentration C_i and uniform initial bulk hydrogen distribution (C_0), is described by the following equation [8] [9]:

$$\frac{C(x,t) - C_0}{C_i - C_0} = 1 - erf\left(\frac{x}{\sqrt{4Dt}}\right) \quad (5)$$

---

[1] Note that Fick's second law is Fick's first law applied on a control volume and can be derived from [8]: $\frac{\partial C}{\partial t} = -\frac{\partial}{\partial x} J = \frac{\partial}{\partial x}\left(D\frac{\partial}{\partial x} C\right) = D\frac{\partial^2 C}{\partial x^2}$

where

$$erf(u) = \frac{2}{\sqrt{\pi}} \int_0^u \exp(-u^2)du \text{ and } u = \frac{x}{\sqrt{4Dt}} \quad (6)$$

C(x, t) is the sought concentration of hydrogen and C_0 the bulk concentration. A sketch of the model is presented in Figure 3. L denotes the wall thickness, which according to the assumptions is not included in the model.

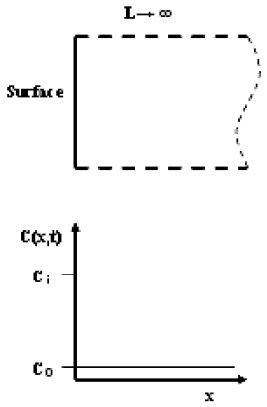

Figure 3 Thick plate diffusion model

By implementing the appropriate values into a spread sheet, the hydrogen distribution can be calculated as a function of distance from the surface and time. Figure 4 presents the result from calculations using a diffusion coefficient of $1.0 \cdot 10^{-13}$ m^2/s based on [2] for SDSS, a hydrogen concentration of 30 ppm at the surface and 2 ppm in the bulk.

3.2 The thin plate solution

The thin plate solution of Fick's second law is applicable for constant and equal surface hydrogen concentration on both sides and uniform initial bulk concentration and is described by the converging series [8], [9]:

$$\frac{C(x,t) - C_0}{C_i - C_0} = 1 - \frac{4}{\pi} \sum_{n=0}^{\infty} \frac{(-1)^n}{2n+1} \exp\left\{ -D(2n+1)^2 \frac{\pi^2 t}{4l^2} \right\} \cos\frac{(2n+1)\pi x}{2l} \quad (7)$$

The plate thickness is *2l*. By introducing dimensionless groups for hydrogen concentration, time and distance the equation reduces to:

$$\theta = 1 - \frac{4}{\pi} \sum_{n=0}^{\infty} \frac{(-1)^n}{2n+1} \exp\left\{ -(2n+1)^2 \frac{\pi^2 \tau}{4} \right\} \cos\frac{(2n+1)\pi\xi}{2} \quad (8)$$

where:

$$\theta = \frac{C(x,t) - C_0}{C_i - C_0}, \quad \tau = \frac{Dt}{l^2} \; and \quad \xi = \frac{x}{l} \tag{9}$$

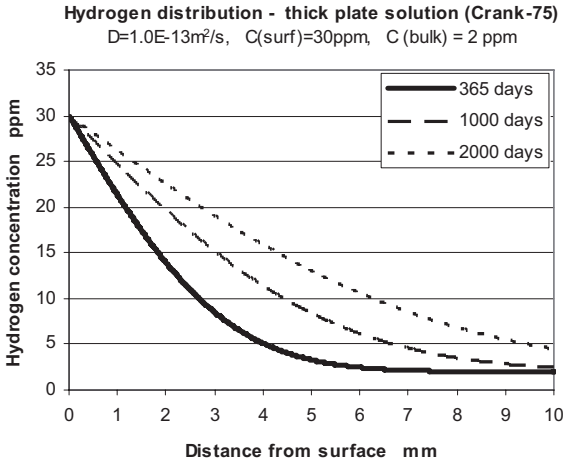

Figure 4 Hydrogen distribution in a thick plate at different times. Results from solving the thick plate solution of Fick's second law, assuming a initial hydrogen content of 2 ppm, a diffusion coefficient of $1.0 \cdot 10^{-13}$ m^2/s and a sub surface hydrogen level of 30 ppm

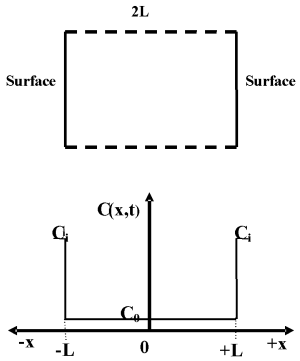

Figure 5 Thin plate diffusion model.

This solution is somewhat more complicated than the thick plate solution, but can still fairly easily be implemented in a spread sheet. Since the solution is given as a converging series, the solution has to be performed for a sufficient number of n ensuring correct θ-values. Note that the solution is symmetrical about the centre axis of a plane, see Figure 5.

The following example is presented: Given a wall thickness of 20 mm, a diffusion coefficient of $1.0 \cdot 10^{-13}$ m^2/s, a surface hydrogen concentration of 30 ppm and an initial bulk concentration of 2 ppm. The hydrogen distribution is calculated for n=1-15 for different values of the normalized time τ.

The calculated results are presented in Figure 6. Note that about 3 years are needed to obtain an H-concentration close to the surface level of hydrogen throughout the wall.

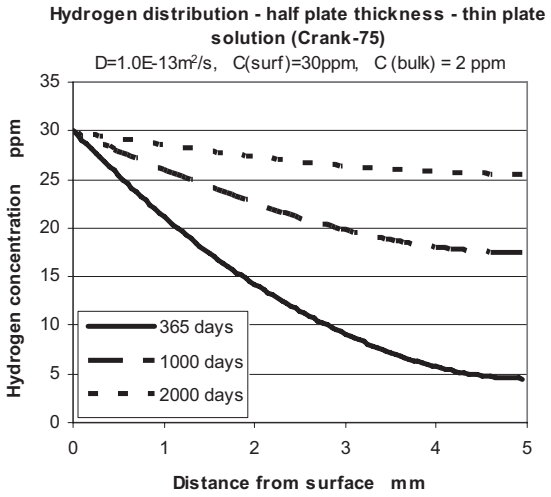

Figure 6 Hydrogen distribution in a thin plate at different times. Calculated using the thin plate diffusion model, assuming a initial hydrogen content of 2 ppm, a diffusion coefficient of $1.0 \cdot 10^{-13}$ m^2/s and a sub surface hydrogen level of 30 ppm

3.3 The uniaxial solution for diffusion in butt welds

Hydrogen diffusion into a heat affected zone from the weld metal can be estimated using the uniaxial diffusion model presented in Eq. 10 and 11 [8] [9].

$$\frac{C(x,t)-C_0}{C_i-C_0}=\frac{1}{2}\left[erf\left(\frac{x+l}{\sqrt{4Dt}}\right)-erf\left(\frac{x-l}{\sqrt{4Dt}}\right)\right] \tag{10}$$

Along the weld centreline, where x=0, the solution simplifies to

$$\frac{C(x,t)-C_0}{C_i-C_0}=erf\left(\frac{L}{\sqrt{4Dt}}\right) \tag{11}$$

A principal sketch of the model is presented in Figure 7. *2l* is the width of the weld zone and C_i and C_0 denote the initial hydrogen level in the weld and heat affected zone (HAZ), respectively. Using this simple model, quick assessments of hydrogen content in the HAZ can be performed. Assuming that the weld hydrogen is available for diffusion, the HAZ hydrogen content can be calculated as a function of time (after welding) and distance from the fusion line.

Figure 8 presents the hydrogen concentration in the heat affected zone after welding given a weld bead width of 20 mm, a weld hydrogen concentration of 9.6 ppm, a bulk hydrogen concentration of 2 ppm and a diffusion coefficient representative of SMSS; $D=8.0 \cdot 10^{-11}$ m^2/s. The results show that close to the fusion line (0.1mm) the hydrogen

content increases from 2 to 4 ppm immediately after welding. A maximum of 5 (ppm) is reached after about 15 hours before the concentration decreases again. Further away from the fusion line, the maximum concentration level is reached some hours later.

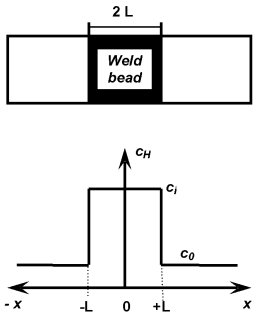

Figure 7 Uniaxial diffusion model [5]

This example demonstrates the importance of keeping the weld metal hydrogen content low. A hydrogen concentration of 4 ppm close to the fusion line (in coarse grained HAZ) in as welded condition could easily cause hydrogen cracking in the heat affected zone of SMSS.

A backward calculation using the referred solution can be applied also to make assessments of the initial weld metal (WM) hydrogen content if the hydrogen content in HAZ and WM in a specific time after welding is known. This could provide vital information regarding the cause of failure in a welded joint.

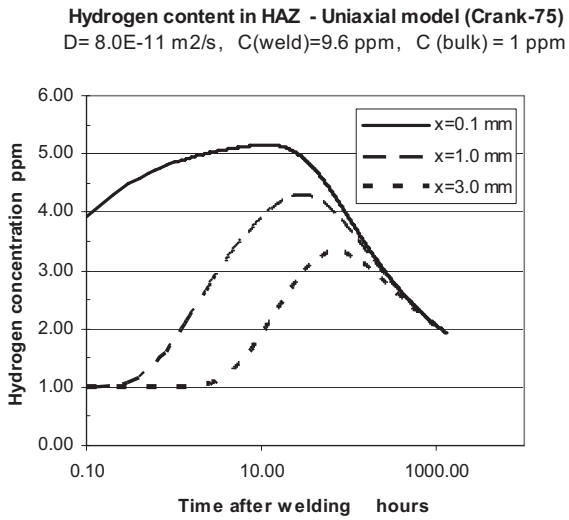

Figure 8 Calculated hydrogen concentration in heat affected zone after welding as a function of time representative of welding of supermartensitic stainless steel ($D=8.0 \cdot 10^{-11} m^2/s$), and weld metal hydrogen concentration of 9.6 ppm.

The three referred solutions of Fick's second law and the accompanying examples illustrate that quick assessments of the hydrogen distribution in steel exposed to hydrogen can be obtained by solving analytical solutions in a spread sheet. Note that the solutions are based on uniaxial diffusion and the use of constant diffusion coefficients.

Diffusion calculations in finite element-codes as ABAQUS [10] are based on solution of Fick's law and should be used when complicated geometries and diffusion conditions are considered. 2D and 3D diffusion, transient temperature conditions or unequal distribution of hydrogen concentration or stress are typical examples.

3.4 Effect of local stress and strain gradients on hydrogen accumulation

The effect of local stress and strain fields on the hydrogen diffusion is a topic of special interest related to the mechanical properties and fracture toughness.

A notch or crack subjected to a plane opening stress will, in mechanical terms, be described by a local stress and strain field ahead of the notch tip. The strain field is at it's highest at the notch tip and then gradually decreases with increasing distance from the notch tip. The hydrostatic stress field reaches maximum a short distance ahead of the crack tip, Figure 9. The diffusible lattice hydrogen will accumulate at sites of increased hydrostatic stress due to dilatation of the lattice. Hydrogen also accumulates at trapping sites caused by local plastic deformation [11].

One of the main challenges is to link the micromechanical and diffusion processes present in the fracture process zone, with the global behaviour of the component or structure.

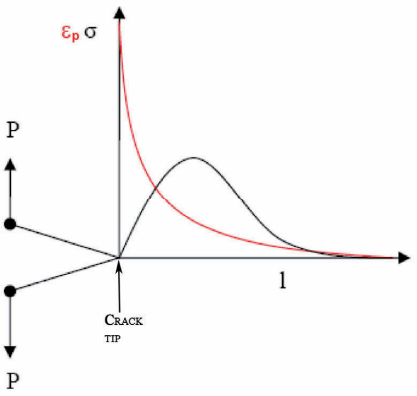

Figure 9 Illustration of stress and strain field ahead of a notch tip in plane mode I loading.

3.4.1 Influence of stress on hydrogen diffusion

Hydrostatic stress is traditionally viewed as the main driving force of hydrogen diffusion from the bulk material towards a crack tip. The governing equation for the stress driven diffusion as implemented in ABAQUS is:

$$J = -sD\nabla\left(\phi + \kappa_p \cdot p\right) \tag{12}$$

Note that hydrostatic pressure (p = -σ_m) is applied. ϕ is the normalized hydrogen concentration C/s, where s is the solubility. κ_p is the stress factor to be linked with gradients in hydrostatic pressure , ∇ p , and is expressed as:

$$\kappa_p = \frac{\overline{V}_H \phi}{R(T - T^z)} \tag{13}$$

Where $\overline{V}_H$ =2.0x10^3 mm^3/mol is the partial molar volume of hydrogen in iron-based alloys [10]. T^Z is the absolute zero temperature (0K or -273°C).

The normalized concentration ϕ is dependent on the hydrostatic pressure:

$$\phi = \phi_0 \exp\left(\frac{-\overline{V}_H p}{R(T - T^Z)}\right) \tag{14}$$

ϕ_0 is the normalized hydrogen concentration in the unstressed state. The mass conservation equation requires:

$$\frac{\partial C}{\partial t} = -J \cdot \nabla \tag{15}$$

Inserting Eq. 12 into Eq. 15 and applying s $\cdot$ ϕ = C gives a modified Fick's law with respect to hydrostatic pressure:

$$\frac{\partial C}{\partial t} = D\nabla^2 C + D \cdot \frac{V_H}{R \cdot \left(T - T^Z\right)} \nabla C \cdot \nabla p + D \cdot \frac{V_H}{R \cdot \left(T - T^Z\right)} C \nabla^2 p \tag{16}$$

By implementing material specific parameters for superduplex stainless steel, the following example can be given: a 12 mm single edge notch tensile specimen (SENT) with a 2mm crack is loaded in tension. The surface hydrogen concentration is 30 ppm and the diffusion coefficient is D=2.9·10^{-16} m^2/s calculated by Eq. 28 [3] for 4°C. All loads and boundary conditions are presented in Table 3. Figure 10 shows the hydrogen distribution in front of the crack tip after periods of 20 days to 11 years. We clearly observe the hydrogen accumulation in front of the crack tip at the location of maximum hydrostatic stress.

3.4.2 Trapping

In addition to the diffusible hydrogen atoms, hydrogen can be trapped in the structure. Typical trapping sites are dislocations, vacations, grain boundaries, phase boundaries, inclusions and precipitates. Trapping reduce the amount of mobile hydrogen and hence, delay the hydrogen transport [11].

The ability of a trap site to hold a hydrogen atom is associated with hydrogen binding energy and the activation energy for hydrogen release. Trapping sites are normally divided in two categories, reversible and irreversible traps. At reversible traps, hydrogen can typically be released by tempering. The binding energy for reversible traps is

typically below 60-70 kJ/mol [4]. At irreversible traps the energy barrier for regaining the mobility is higher and not possible to overcome by normal tempering procedures. Hydrogen is typically irreversibly trapped at the interface between non-metallic inclusions and precipitates like MnS, Al_2O_3 and TiC [12].

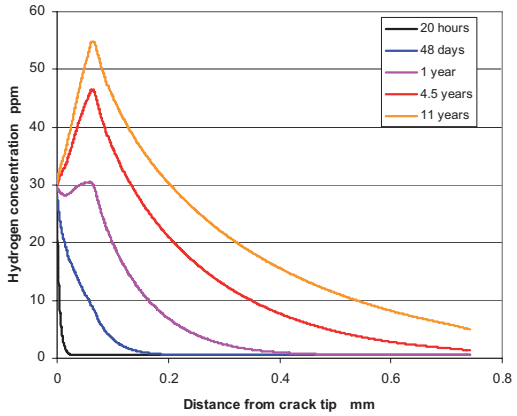

Figure 10 Distribution of hydrogen concentration in front of the crack in a in a SENT specimen calculated using ABAQUS.

Table 3 Loads and boundary conditions in ABAQUS FE analyses.

Parameters for diffusion analyses		**Parameters for stress analyses**	
Solubility (ppm·mm·$N^{-1/2}$)	0.033	Yield strength (MPa)	600
Diffusion coefficient ($mm^2 \cdot s^{-1}$)	$2.9 \cdot 10^{-10}$	Youngs modulus (MPa)	200 000
Initial bulk H concentration (ppm)	0.5	Poisson's ratio	0.3
Surface H concentration (ppm)	30	Uniaxial tension stress (MPa)	510
Temperature (°C)	4		
Pressure stress factor, κ_p ($mmN^{-1/2}$)	$8.64 \cdot 10^{-4} \cdot \phi$		

Of special interest in the stainless steels are the trapping ability of austenite in two phase steels such as duplex steels and the retained austenite in martensitic stainless steels. Due to its low diffusion coefficient it can be argued that austenite; in the general sense is an irreversible trap. The effective diffusion coefficient (D_{eff}) under the influence of reversible traps is described by Eq. 17 [4] [12].

$$D_{eff} = \frac{D_0 \, e^{\frac{-E_L}{RT}}}{1 + \frac{N_T}{N_L} e^{\frac{-E_T}{RT}}} \tag{17}$$

where N_L and N_T is the number of sites for hydrogen in the lattice and at reversible traps, respectively. E_L and E_T are the binding energy in lattice and at reversible traps (J/mol). Notice that the influence of reversible trapping decrease as the temperature increases. Hence, Eq. 17 reduces to Eq. 1 in the absence of reversible traps.

3.4.3 Influence of strain on the trapping of hydrogen

The treatment of crack tip hydrogen concentration has traditionally been based on the accumulation of hydrogen in areas of high hydrostatic stress as calculated by Eq. 16. Sofronis and McMeeking [13] and later Krom and Bakker [14] described models reflecting a competition between the hydrostatic stress field and the highly strained area at the notch tip with respect to the hydrogen diffusion and concentration in blunting crack tips. Their models are based on the principle that populations of hydrogen in trapping sites and in lattice always are in equilibrium, as described by Oriani [15]:

$$\frac{\theta_T}{1-\theta_T} = \frac{\theta_L}{1-\theta_L} K_T \tag{18}$$

where θ_L denotes the occupancy of interstitial lattice sites, θ_T the occupancy of trapping sites and $K_T = e^{\frac{-E_T}{RT}}$. The concentration in lattice and traps can be written

$$C_L = \theta_L N_L \tag{19}$$

$$C_T = \theta_T N_T \tag{20}$$

From Eq. 19 and 20 and assuming $\theta_L << \theta_T$, the equilibrium concentration of hydrogen can be written:

$$C_T = \frac{N_T}{1 + \frac{1}{K_T \theta_L}} \tag{21}$$

The number of traps is however dependant of the level of plastic strain. Sofronis and McMeeking [13] proposed a fitted relation between N_T and plastic strain based on experimental data for iron from Kumnick and Johnson [16].

$$\log N_T = 23.26 - 2.33 e^{-5.5\varepsilon_p} \tag{22}$$

Regarding the lattice sites a constant, the partial derivative of the hydrogen concentration in traps (Eq. 21) as a function of time becomes:

$$\frac{\partial C_T}{\partial t} = \frac{\partial C_T}{\partial C_L} \cdot \frac{\partial C_L}{\partial t} + \frac{\partial C_T}{\partial N_T} \cdot \frac{dN_T}{d\varepsilon_p} \cdot \frac{\partial \varepsilon_p}{\partial t} \tag{23}$$

Representing $\frac{\partial C_T}{\partial C_L}$ with $\frac{C_T(1-\theta_T)}{C_L}$, $\frac{\partial C_T}{\partial N_T}$ with θ_T and implementing it into Eq. 23, the total Fick's law including the effect of hydrostatic pressure and the plastic strain rate becomes:

$$\frac{C_L + C_T(1-\theta_T)}{C_L} \frac{\partial C_L}{\partial t} = \nabla \cdot (D_L \nabla C_L) - \nabla \cdot \left(\frac{D_L C_L V_H}{R\left(T - T^Z\right)} \nabla p \right) - \theta_T \frac{dN_T}{d\varepsilon_p} \frac{\partial \varepsilon_p}{\partial t} \tag{24}$$

The influence of strain on hydrogen concentration is not a standard option in commercial available FE-codes and must be implemented by user sub routines. The finite element formulation of Eq. 24 can be found in Krom et al. [14].

3.5 Reported diffusion coefficients for selected steel alloys

The diffusion coefficient can be established for different electrochemical charging conditions and metals by permeation measurements in electrochemical cells, as the Devanathan & Stachursky cell [17]. The principle is based on hydrogen diffusion through a thin metal foil mounted between two electrochemical compartments. In the entrance cell the specimen surface is cathodic polarized so that adsorbed hydrogen forms on the surface. The adsorbed atomic hydrogen either form hydrogen gas, or absorbs in the metal as atomic hydrogen. In the exit cell the surface of the sample is anodic polarized, oxidizing the absorbed hydrogen to H-ions and electrons.

The difference in electric current between the inlet and the exit side gives an indirect measure of the number of hydrogen atoms that has diffused through the sample. The results are normally presented as permeation transients, giving the hydrogen permeation flux as a function of time. Thorough descriptions of the method can be found in British Standard BS 7886 [18].

Diffusion coefficients for different types of steels reported in the literature are summarized in Table 4. There is large discrepancy in the reported diffusivities within the same categories of stainless steels. The variation reflects the differences in charging conditions, temperature, surface oxide/ deposits, chemical composition and microstructure. The values probably also reflect the problems with quantifying the diffusion coefficient through an indirect method as the Devanathan & Stachursky cell.

Nevertheless, some trends are observed. Pure α-iron and ferritic stainless steel have the highest reported diffusion coefficient followed by low alloy steel and martensitic stainless steels. The lowest diffusion coefficients are reported for duplex steel and austenitic stainless steel. For SMSS and DSS a decreased diffusivity with increasing austenite content can be observed.

Knowledge of the specific diffusion coefficient is necessary in calculations of the hydrogen concentration or distribution. The large scatter in reported diffusion coefficient for the same types of stainless steel is thus a matter of concern (and often a source of confusion), since the diffusion coefficient has a large influence on the calculated results.

4 Hydrogen diffusion in duplex and supermartensitic stainless steels

4.1 Duplex and super duplex stainless steels

The reported diffusion coefficient of DSS and SDSS, regardless of the charging conditions, varies between $1.8 \cdot 10^{-12}$- $4.6 \cdot 10^{-16}$ m^2/s, ref. Table 4.

Diffusion in the austenite phase in DSS/SDSS has an insignificant influence on the effective diffusion coefficient. The diffusion is however slower in DSS/SDSS than in ferritic steels. This is considered to be an effect of:

1. Increased diffusion length in the ferrite due to the austenite islands. This is referred to as an increased tortuous path for the hydrogen.
2. Trapping in the austenite phase or at the austenite phase boundaries.

Turnbull and Beylegaard [3],[19] carried out permeation measurements according to [18] at different temperatures on 0.1mm thick samples of one DSS (SAF 2205) and one SDSS (SAF 2507) and reported a tortuous factor of ω=0.24. The permeation direction was perpendicular to the rolling direction of the steel. Eq. 25 is a modification of Eq. 17, taking the tortuousity factor into account.

$$D_{eff} = \frac{\omega D_0 e^{\frac{-E_L}{RT}}}{1 + \frac{N_R}{N_L} e^{\frac{-E_R}{RT}}} \qquad (25)$$

Zakroczymski and Owczarek [4] reported a tortuousity factor between 0.21 and 0.59 for DSS. During degassing of hydrogenated samples the diffusion coefficient of trapped hydrogen was $1.4 \cdot 10^{-16}$ m^2/s, which is close to values reported for austenitic steel. Based on this observation it can be argued that the austenitic phase it self act as a trap. Turnbull et al report the following regression equations for the effective diffusion coefficients [3] [19]:

SAF 2205 (DSS)

Lattice diffusion: $D_{eff} = 2.8 \cdot 10^{-8} \exp[(-39.3kJ/mol)/RT]$ (m^2/s) (26)

Including reversible traps: $D_{eff} = 1.2 \cdot 10^{-6} \exp[(-50.7kJ/mol)/RT]$ (m^2/s) (27)

SAF 2507 (SDSS)

Lattice diffusion: $D_{eff} = 1.3 \cdot 10^{-7} \exp[(-45.9kJ/mol)/RT]$ (m^2/s) (28)

Including reversible traps: $D_{eff} = 4.3 \cdot 10^{-6} \exp[(-55.7kJ/mol)/RT]$ (m^2/s) (29)

Table 4 Reported diffusion coefficients for iron and selected steel alloys.

Steel	Alloy	Diffusion coefficient (m^2/s)	Charging conditions	Test temp. (°C)	Aust. Cont. (%)	Ref.
Pure α- iron		$7.2 \cdot 10^{-9}$	-	25	-	[7] [3][4][19]
		$7.2 \cdot 10^{-9}$	-	22	-	"
		$8.7 \cdot 10^{-9}$	-	50	-	"
		$1.0 \cdot 10^{-8}$	-	80	-	"
Low alloy steel	X65	$1\text{-}2 \cdot 10^{-9}$	20 A/m^2 in 0.1N NaOH	25	-	[20]
		$4\text{ -}5 \cdot 10^{-10}$	40 A/m^2 in 0.1N NaOH	25	-	"
	M520	$1.1 \cdot 10^{-10}$	-1050 mV SCE in	22	-	[20]
		$1.9 \cdot 10^{-11}$	0.5M NaCl	22	-	"
		$3.0 \cdot 10^{-11}$	-900 mV "	22	-	"
		$5.5 \cdot 10^{-11}$	-800 mV "	4	-	"
		$2.5 \cdot 10^{-11}$	-1050 mV "	4	-	"
		$2.0 \cdot 10^{-13}$	-900 mV "	4	-	"
			-800 mV "		-	
	HSLA 80	$1.3 \cdot 10^{-12}$		25	-	[21]
	HSLA 100	$4.5 \cdot 10^{-13}$	10mA in 0.1 M NaOH	25		"
			"			
Ferritic stainless steel (heat treated)	Fe-Cr	$2.9 \cdot 10^{-5}$	-	70	-	[4]
	AL 29-4-2	$6.1 \cdot 10^{-7}$	-	70	-	"
	SAF 2205	$4.9\text{-}5.5 \cdot 10^{-13}$	1mA/cm^2 in 0.1M NaOH	22	-	[3]
Martensitic stainless steel	PH 13-8	$6.7 \cdot 10^{-13}$	1mA/cm^2 in 0.1 M	-	-	[4]
	AISI 410	$1.8 \cdot 10^{-12}$	NaOH	-	-	"
			"			
Supermartensitic stainless steel	13%Cr	$2.5 \cdot 10^{-13}$	0.046 mA/cm^2 in 0.1M NaOH	-	12	[4]
		$3.0 \cdot 10^{-13}$		22	-	[22]
		$6.1 \cdot 10^{-14}$	-1050 mV SCE in 0.5 M NaCl	4	-	"
	12CrNi Mo	$1.6 \cdot 10^{-9}$	"	25	-	[23]
		$6.9 \cdot 10^{-10}$		4	-	"
		$8.2 \cdot 10^{-10}$	-1050 mV SCE in 3(%) NaCl	4	-	"
	13%CrNiMo	$1.3 \cdot 10^{-11}$	"	70	<2	[5]
		$1.2 \cdot 10^{-12}$	-900 mV SCE in 3(%)	70	4.8	"
		$1.0 \cdot 10^{-12}$	NaCl	70	8.5	"
		$7.2 \cdot 10^{-13}$		70	19.2	"
		$6.0 \cdot 10^{-13}$	H_2 gas, 10^5Pa	70	25	"
			"			
			"			
			"			
			"			
Duplex stainless steel						
Lattice diffusion	SAF 2205	$2.8\text{-}3.0 \cdot 10^{-15}$	1mA/cm^2 in 0.1M	22	49	[3][19]
		$1.0\text{-}1.5 \cdot 10^{-14}$	NaOH	50	49	"
		$3.8\text{-}4.5 \cdot 10^{-14}$	"	80	49	"
			"			
with influence of traps		$1.1\text{-}1.4 \cdot 10^{-14}$		22	49	"
			"	50	49	"
		$5.2\text{-}9.5 \cdot 10^{-15}$	"			

Superduplex stainless steel						
lattice diffusion	SAF2507	$1.1 \cdot 10^{-15}$	$1mA/cm^2$ in 0.1M	22	49	[3][19]
		$4.5\text{-}5.2 \cdot 10^{-15}$	NaOH	50	49	"
		$1.8\text{-}2.5 \cdot 10^{-14}$	"	80	49	"
			"			
with influence of traps		$4.6 \cdot 10^{-16}$		22	49	"
			"			
	H25N5M	$1.8 \cdot 10^{-12}$		25	40	[2]
		$1.0 \cdot 10^{-13}$	$10\ mA/cm^2$ in 0.1M NaOH	"	"	"
			"			
Austenitic stainless steel		$1.8\text{-}8.0 \cdot 10^{-16}$	-	-	-	[2]

The equations including reversible traps yield diffusion coefficients close to the diffusion coefficient of pure austenite: $5.2\text{-}9.5 \cdot 10^{-15}$ m^2/s, which is close to the degassing values obtained by Zakroczymski et al. [2][4].

Zakroczymski et al. report permeation diffusion coefficients in the range of $1.8 \cdot 10^{-12}$ - $1.0 \cdot 10^{-13}$ m^2/s for DSS, which is 10 - 20 times higher than reported by Turnbull et al. Zakroczymski used a permeation direction *parallel* with the rolling direction of the steel promoting a straighter diffusion path along the ferrite grains. This will contribute to a faster diffusion rate.

Aspects as the shape, size and spacing of the austenite islands influence both the tortousity, H trapping tendency and crack stop properties of the steel. Fine dispersed austenite islands promote longer diffusion paths and more trapping compared to a structure consisting of coarse austenite island and larger intermediate ferrite "paths". With respect to fracture resistance short austenite spacing is normally preferable due to the crack stop properties of the more ductile austenite phase. However, this also depends on the austenite shape. Woollin and Gregory [24] reported a better capacity of preventing H assisted cracking in duplex steel with elongated austenite islands perpendicular to the loading direction compared to fine equiaxed particles.

A model presented by Gesnouin et al. [5] is based on viewing the duplex microstructure as organized in a parallel or series pattern gives fairly good estimates of the overall diffusion coefficient. The austenite islands are pictured as long parallel platelets. In the parallel configuration, the hydrogen moves in the ferrite along and between these platelets. The permeation coefficient can then be calculated (as in a parallel electric coupling):

$$\Phi = \Phi_\gamma X_\gamma + \Phi_\alpha (1 - X_\gamma) \tag{30}$$

Hydrogen permeation perpendicular to the phase platelets can be calculated (as a series coupling):

$$\Phi = \frac{1}{\frac{X_\gamma}{\Phi_\gamma} + \frac{1 - X_\gamma}{\Phi_\alpha}} \tag{31}$$

Φ_γ and Φ_α is the permeation coefficient (molH/cm s $bar^{1/2}$) for the austenite and ferrite and X_γ is the volume fraction of austenite. The relation between the permeation coefficient Φ and the diffusion coefficient D is described by: Φ=S x D, where S (molH/$m^3 bar^{1/2}$) is the solubility of hydrogen in the different phases.

If all soluble hydrogen mainly is regarded present in the austenite ($\Phi=S_\gamma \cdot D$), the diffusion coefficient for the two orientations can easily be calculated. By applying a diffusion coefficients for α iron ($7 \cdot 10^{-9}$ m^2/s) and austenite ($5 \cdot 10^{-16}$ m^2/s),Table 4, and solubility for the phases equal to 6.7×10^{-3} for ferrite and 6.9 for austenite [5], the diffusion coefficients can be presented as a function of the austenite content and configuration, see Figure 11. (Where no exact austenite content is given, a volume fraction of 0.5 is assumed.) Observe that the main part of diffusion coefficients for duplex steel from Table 4 fall within the presented scatter band. Hence, the proposed method can be a suited tool for quick assessment of the diffusion rate for the material at hand when exact diffusion data are not available.

Despite the reported observations regarding the influence of the amount, orientation and trapping tendency of the austenitic phase on diffusivity, there seem to be a lack of systematic studies on this topic.

4.2 Supermartensitic stainless steels

The hydrogen diffusion constant in martensitic steels regardless of the material type and charging conditions is reported to be in the range $1.6 \cdot 10^{-9}$- $6.1 \cdot 10^{-14}$ m^2/s, according to Table 4.

SMSS can also be regarded as a two phase steels, with a martensite matrix (α) containing austenite islands (γ). Turnbull et al. [3] [19] has estimated a tortuousity factor ω= 0.8 for martensitic stainless steel with 12 percent retained austenite. The hydrogen diffusion in SMSS as a function of the retained austenite content has also been investigated by Gesnouin et al [25]. Compared to low tempered martensitic 13%Cr steel with less than 2 percent retained austenite, introducing about 5 retained austenite was found to delay the diffusion coefficient with an order of magnitude. The diffusion was further 50 percent delayed, as the amount of retained austenite increased from 5 to 25 percent. Results from the work by Gesnouin are given in Table 4.

The diffusion coefficients for given austenite contents for SMSS in Table 4 are plotted in Figure 11. All except one value falls within the scatter band given by the series and parallel configuration.

The stability of the retained austenite is a key argument for the quality of these steels. Transformation of retained austenite to martensite causes volumetric expansion and hence local stress concentrations in the matrix. The transformed martensite is brittle and in the presence of hydrogen, the transformation itself can introduce micro-cracks.

Park et al [12] argues that during welding retained austenite can act as a reservoir for hydrogen and that martensite transformation will supply hydrogen to the surrounding martensitic matrix.

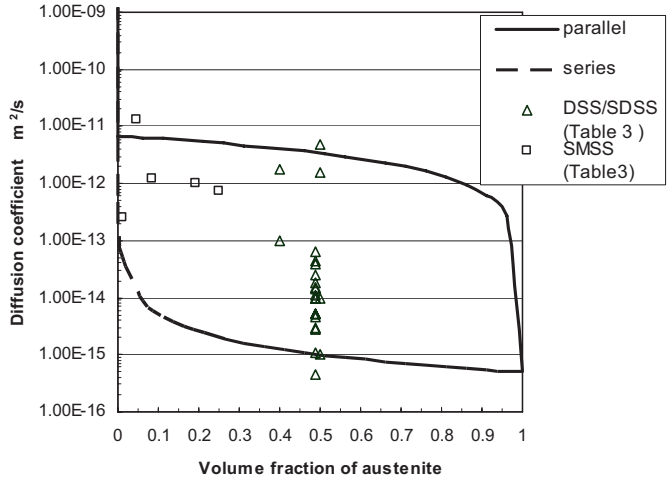

Figure 11 H diffusion coefficient as a function of austenite content and orientation of the structure.

5 Micromechanical models of hydrogen assisted cracking

There are a wide range of proposed analytical and FE – models aiming to describe hydrogen assisted micromechanical behaviour in front of a crack tip. The models are often based on the assumption of a large number of parameters and boundary conditions, and they are difficult to compare due to the different approaches regarding the calculation of stress and hydrogen distribution and the definition of the crack critical stresses.

In general the models are based on established elastic-plastic fracture mechanics theory. Since the hydrogen influence is active within the highly deformed area (process zone) close to the crack tip, and hence outside the range where classical small strain theory is valid, descriptions of strain based plasticity should be included. However, no complete fracture mechanics model describing both the crack tip stress and strain within the hydrogen affected process zone exists. This is due to the fact that the mechanisms within the process zone are complex and still not very well understood.

Therefore, some assumptions regarding the micromechanical behaviour in front of the crack have to be done. The most cited approaches in this respect are the hydrogen enhanced decohesion (HEDE) and the hydrogen enhanced local plasticity (HELP).

5.1 Hydrogen enhanced decohesion - HEDE

The hydrogen enhanced decohesion mechanism was first proposed by Troiano in 1960 [26] and further developed by Oriani et al and Gerberich et al. [15] [27]. HEDE is

based on the hypothesis that interstitial hydrogen lowers the cohesive strength by dilatation of the atomic lattice and hence lowers the fracture energy. This implies that hydrogen decreases the energy barrier for either grain boundary or cleavage plane decohesion. The notion is that fracture will initiate in the area of maximum hydrostatic stress some distance ahead of the crack tip. The "global" fracture toughness is described as a function of a local (crack tip) fracture toughness and local hydrogen content as described by [27] [28]:

$$K_{I_{th}} = \frac{1}{\beta'} \exp\left\{ \frac{\left(k_{IG} - \alpha C_H\right)^2}{\alpha'' \sigma_{ys}} \right\} \tag{32}$$

K_{Ith} is the "global" fracture toughness threshold while k_{IG} is the critical local fracture toughness. C_H is the local hydrogen concentration (atom fraction) and σ_{ys} the yield strength. α is taken as 0.5 MPa $m^{1/2}$ /atom fraction. The constants α'' and β' are parameters that can be determined by FE-calculations by fitting to experimental results. The local hydrogen content is found as a function of hydrogen gas pressure, p, heat of solution for hydrogen in iron, H_s (J/mol), and the local trap binding energy, β (J/mol), using the following expression:

$$C_H = \frac{c' \sqrt{p} \exp\left(\frac{\beta - H_s}{RT} \right)}{1 + c' \sqrt{p} \exp\left(\frac{\beta - H_s}{RT} \right)} \tag{33}$$

c' is the Sieverts coefficient ($Pa^{-1/2}$). FE-results have proven to fit well with experiments on Fe-3wt percent Si and Mo single crystals and for 4340 steel. The following situations were found to decrease the local and hence the global fracture toughness:

- Crack Mode I dominance
- High yield strength
- Increasing hydrogen pressure or internal concentration
- High grain boundary segregation of metalloids
- Decreased elastic modulus

5.2 Hydrogen enhanced local plasticity - HELP

Hydrogen enhanced local plasticity (HELP) is characterized by atomic hydrogen enhancing the mobility of dislocation movement in preferred crystallographic planes at the crack tip. This "local softening" results in cracking by micro void coalescence along these planes, see Figure 12. The mechanism was first introduced by Birnbaum and co-workers in 1990 [29]. Later Sofronis [30] and Delafosse & Magnin [31] quantified the stress field surrounding the hydrogen atoms causing enhanced dislocation glide. The mechanism can be described as local plasticity that is macroscopically brittle [11]. A HELP crack will tend to initiate from slip planes at the crack tip.

Sofronis and co-workers [30][32][33] introduced a theoretical framework describing the localization of slip (shear localization) on a limited number of slip planes in presence of

hydrogen in fcc metals. This is expressed in a continuum approach by Liang, Sofronis and Aravas in [33]:

$$\sigma_y\left(\varepsilon_p, c\right) = \sigma_0(c)\left(1 + \varepsilon^p / \varepsilon_0\right)^N \tag{34}$$

$\sigma_0(c)$ is the yield stress in the presence of hydrogen, hence $\sigma_0(0)$ is the yield stress in the absence of hydrogen. The corresponding yield strain is $\varepsilon_0 = \sigma_0/E$ with E being the Young's modulus. N is the hardening exponent (which is taken as independent of hydrogen in the lack of experimental evidence). A linear expression for the hydrogen dependant yield stress is suggested:

$$\sigma_0(c) = \left[(\xi - 1)c + 1\right]\sigma_0 \tag{35}$$

where $\xi \leq 1$ is a softening parameter. Figure 13 shows the local normalized effective Mises stress σ_e/σ_0 versus effective plastic strain at various initial bulk hydrogen concentrations with $\xi = 0.1$ and N= 0.1. The local stress decreases with increasing hydrogen concentration. Note that the equations 34-35 are presented as an attempt to quantify the hydrogen effect on dislocation movement in a continuum sense and can not be viewed as a precise material response. The notion of the micro-mechanism behind this local softening is based on the concept of a hydrogen "atmosphere" surrounding each dislocation. The hydrogen atmosphere of two parallel edge dislocations will interact and pull the dislocations together, while the hydrogen atmosphere of dislocations with opposite burger vectors will repel each other. Positive forces between the hydrogen atmospheres of dislocations in the same slip plane will give a high dislocation density and a higher hydrogen concentration and the local shear stress needed to initiate slip will be lower than in a hydrogen free material. Delafosse & Magnin [31] obtained similar results regarding interaction forces between dislocations in the same slip plane, see Figure 14. It is observed however, that in stainless steel severe localized slip is accompanied by an increase in the macroscopic flow stress. On the other hand localized slip could, especially at the surface, act as fracture initiation sites.

In a situation with increased hydrogen concentration at a crack tip it is clear that the crack propagation is promoted whether it is by the HEDE or the HELP mechanism. In that sense it can be argued that the crack tip response to stress under hydrogen influence is a competition between atomic lattice decohesion and dislocation emission, between the brittle and ductile response, but at a lower (local) stress level than without hydrogen influence.

The micro mechanisms active at a sharp notch or crack in the presence of hydrogen are far from understood. A large number of parameters, related to the material, the load history and the environment affect the behaviour. The mutual influence between hydrogen and the material properties complicates the picture even further. There is also the need for more reliable input to and verification of the models from experiments and practical experience.

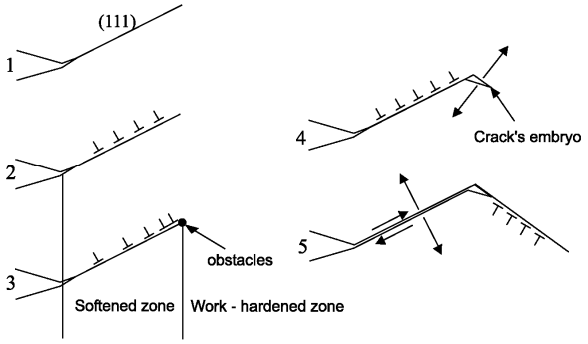

Figure 12 Successive steps in hydrogen enhanced local plasticity, HELP: 1) Slip planes activated at the crack tip 2) enhanced plasticity on (111) planes due to hydrogen absorption, 3) pile up of dislocations near obstacle, 4) initiation of crack or micro void due to the local stress increase and 5) crack opens by shear decohesion along the slip plane [31].

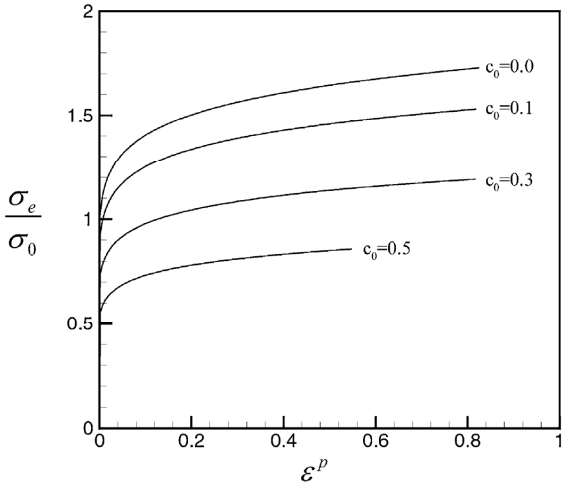

Figure 13 Normalized effective Mises stress versus effective plastic strain at various hydrogen concentrations [35].

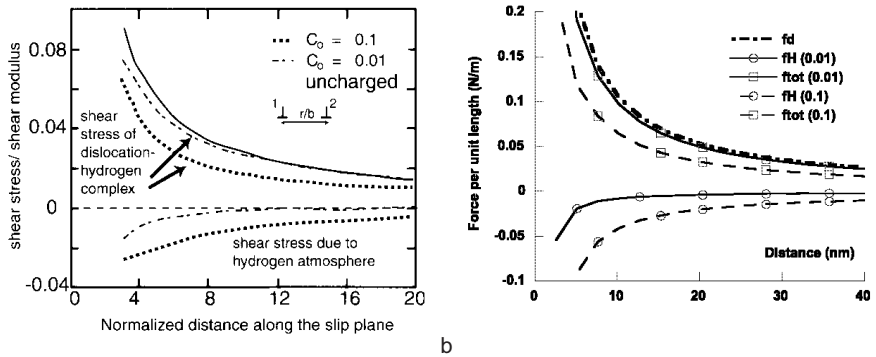

a b

Figure 14 Hydrogen influence on the stress situation in a slip plane – reduction of stress experienced by one edge dislocation due to the presence of the other. The H concentration (0.1 and 0.01) is given as a partial molar volume a) Robertson [34] b) Delafosse [20].

5.3 Experimental observations

Both the HEDE and the HELP mechanism are debated due to the lack of supporting experimental evidence. However, in the recent years several observations supporting the HELP mechanism have been reported. Robertson [34] reported in situ observations of plastic deformation of thin samples in high voltage TEM and found an increasing amount of dislocation pile ups in austenitic 310s stainless steel when introducing hydrogen gas, see Figure 15. An interesting qualitative observation regarding the diffusion of hydrogen in front of a moving crack tip in stainless steel was performed by Oltra & Bouillot [35].

In straining experiments of a SDSS charged with gaseous hydrogen (H_2) an increasing amount of hydrogen in the austenitic phase in front of the crack tip was observed compared to the austenite islands in other parts of the matrix. The investigation of the hydrogen distribution close to the crack tip was performed using an ion microprobe (SIMS). Hydrogen was segregated to the austenite grains in the crack tip path. Typical slip lines were observed in the austenite, and the crack was propagating in a zigzag manner, see Figure 16**.** It was suggested that this feature is related to the interaction of mobile dislocations emitted at the crack tip in the austenite phase which enhance the hydrogen mobility into the austenite phase. This was checked by removing the hydrogen from the vacuum chamber for gaseous charging which resulted in crack arrest in the austenite. This implies that the austenite phase acts as a barrier for crack propagation only if it is not weakened by hydrogen before it's subjected to deformation. Micrographs of a crack passing the transition between ferrite and austenite in duplex steel are presented in Figure 17.

Abraham & Altstetter [35] performed tensile experiments of thin 310s stainless steel hydrogen charged specimens and found a hardening effect with increasing hydrogen content up to 5 at % hydrogen. Above this value a discontinuity in yield and loss in hardening was observed, see Figure 18. This stress relaxing behaviour is consistent with the initiation of slip band behaviour (localized shear) and the easy glide of dislocations as soon as the slip is initiated.

Barnoush & Vehoff [37] employed the nano-indention technique to perform in situ measurements of the hydrogen effect on nickel. Hydrogen was applied by cathodic charging in 0.05M Na_2SO_4 at potential of -1000mV. A reduction of the shear stress of approx. 28% was found. A typical load displacement curve showing hydrogen induced pop-in behaviour is presented in Figure 19. The pop-ins are representative of dislocation glide at the point of maximum shear stress, hence these results also supports the HELP-mechanism.

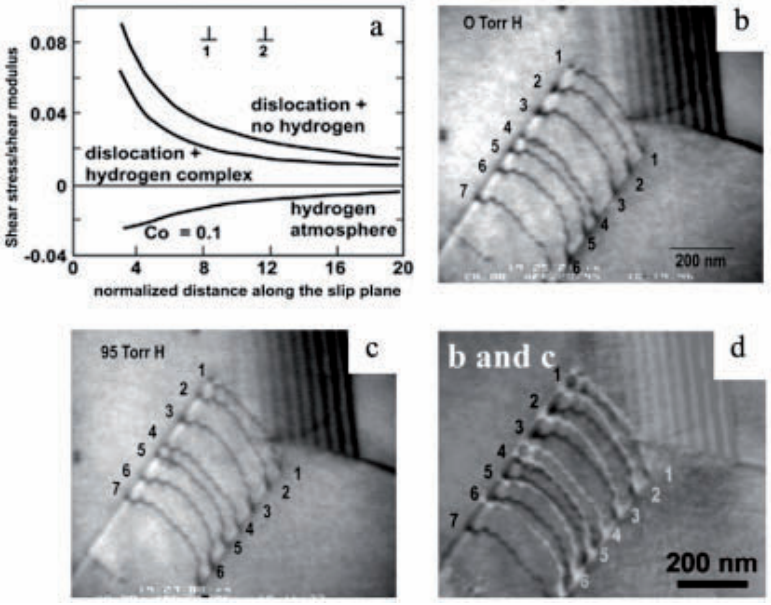

Figure 15 Hydrogen shielding a) plot of the normalized shear stress as a function of separation distance for two edge dislocations on the same slip plane with and without hydrogen b) dislocation pileup at a grain boundary in 310s stainless steel c) effect of introducing 90 (torr) of H gas on the dislocation pileup d) comparison image [34].

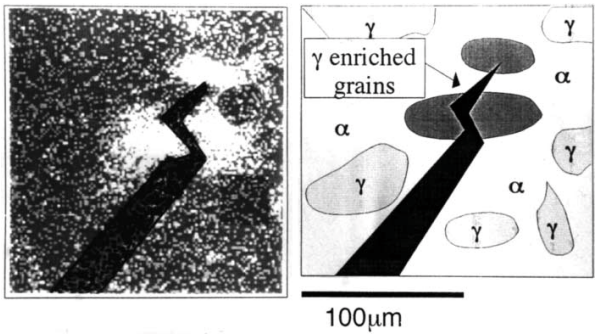

Figure 16 Ion probe image and schematic microstructure and hydrogen path in austenite grains concerned with a crack. Hydrogen appears white in the ion probe image [35].

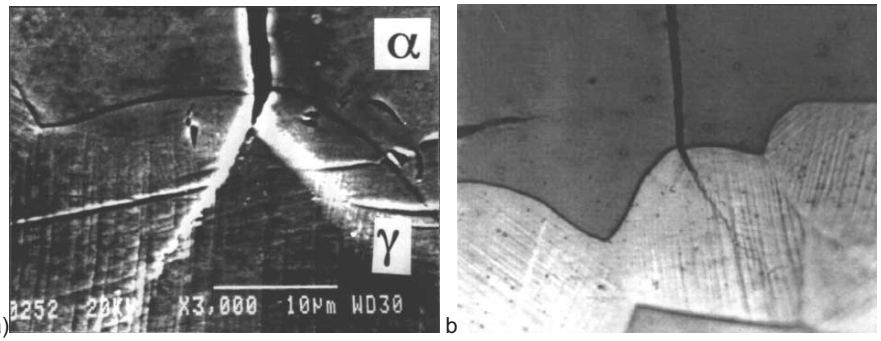

Figure 17 Micrograph of crack path at the α/γ transition - straight cleavage crack in ferrite and zigzag micro cracking along the slip planes in austenite a) optical b) SEM [35].

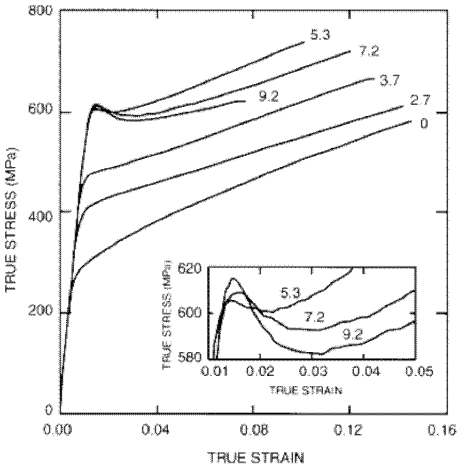

Figure 18 Stress-strain curves for 310s stainless steel at various hydrogen content (at%) at 22°C and a strain rate of $5.5x10^{-5}$ 1/s [35].

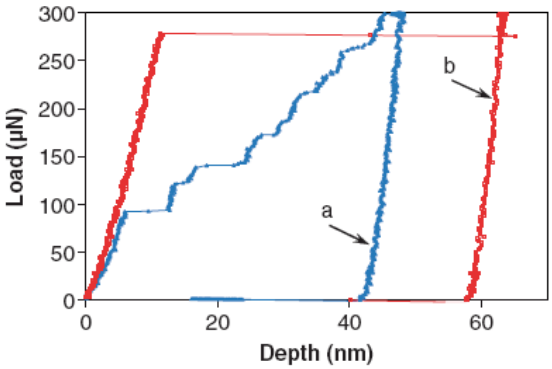

Figure 19 Effect of cathodic charging of hydrogen on the nano-mechanical load displacement curve of Nickel: Curve a: cathodic potential of -1000mV, curve b: anodic potential of 500 mV [37].

6 Recent approaches in FE modelling of hydrogen assisted fracture

Most models attempting to describe hydrogen accumulation in front of a crack tip addresses a loaded stationary notch or crack. Few attempts are made in describing the hydrogen distribution in connection to a moving crack. Cohesive zone modelling (CZM) offers this possibility, and has recently been proposed as a suitable method to handle the modelling of hydrogen assisted cracking.

Cohesive elements are useful in modelling bonded interfaces. The elements can be pictured as two faces separated by a thickness, which is close to zero. The relative motion of the top and bottom faces in the thickness direction represents opening or closing of the interface [10].

The CZM approach is appealing due to the fact that it do not require a response in the bulk of the material as in the traditional damage mechanics approach. The only material response that has to be defined is the traction separation law (TSL) in a thin strip or a small zone of interface cohesive elements ahead of the crack. The TSL represents the relationship between the cohesive stress (σ) and the crack opening (δ), see Figure 20. The area below the curve is known as the cohesive energy (Γ_c).

By definition the cohesive interface separation energy for a pure grain boundary is as described by Dugdale [38]:

$$(2\gamma)_0 = 2\gamma_s - \gamma_b. \tag{36}$$

Where γ_s is the free surface energy and γ_b is the grain boundary energy.

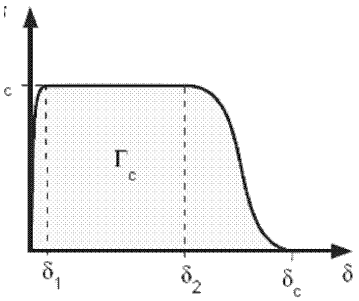

Figure 20 Example of traction separation law used in cohesive zone modelling.

A recent approach (2004) is made by Serebrinsky, Carter and Ortiz [39], using cohesive zone elements governed by a linear atomic-level TSL in a quantum continuum model. The approach combines a stress assisted Fick's law with a cohesive law formulation representative of brittle decohesion. Resulting stepwise cracking is shown in Figure 21. The following relation for the coupling between hydrogen coverage, θ, and the surface energy with hydrogen influence, $\gamma(\theta)$, for bcc Fe is suggested:

$$\gamma(\theta) = (1 - 1.0467\theta + 0.1687\theta^2)\gamma(0) \quad (37)$$

$\gamma(0)$ is the surface energy without hydrogen. The relation is based on a fitting of surface energy values calculated by Jiang and Carter for seven layers of bcc steel atoms [40]. The surface energy without hydrogen influence, $\gamma(0)$, is 2.43 J/m^2. Based on this relation and given a constant critical opening δ_c, the expression given for the local critical hydrogen dependent cohesive stress, σ_c (θ), yields:

$$\sigma_c(\theta) = (1 - 1.0467\theta + 0.1687\theta^2)\sigma_c(0) \quad (38)$$

σ_c (0) is the local critical cohesive stress without hydrogen influence. Hydrogen coverage is defined as a function of the hydrogen concentration and the Gibbs free energy difference between the interface and the surrounding material as expressed in the Langmuir-McLean isotherm [41]:

$$\theta = \frac{C}{C + \exp(-\Delta g_b^0 / RT)} \quad (39)$$

Where C is the hydrogen concentration (ppm), Δg_b^0 is Gibbs free energy-difference between surface and bulk.

Wang [42] treated the interfacial region with the impurities as a thermodynamic system in local equilibrium; introducing the separation energy as a function of the chemical potential, μ, and the crack opening δ, see Figure 22. For reversible change in this state one has:

$$du = Tds + \sigma d\delta + \mu d\Gamma \quad (40)$$

u and s are the excesses of energy and entropy per unit area of interface, T is the temperature where separation occurs, σ is the stress acting perpendicular to the interface, δ is the excess interfacial separation. Here Γ is the interfacial hydrogen concentration and μ is an equilibrating chemical potential associated with the hydrogen on the interface.

The required cohesive stress is expressed by two limiting cases, fixed hydrogen concentration and fixed chemical potential, named fast separation and slow separation respectively. The fast separation case represents cleavage fracture without substantial dislocation activity, and can be regarded as close to the HEDE view of hydrogen fracture. The slow separation case represents a situation closer to HELP where there is large plastic deformation in the material surrounding the fracture and the separation is slow compared to the diffusion rate. The slow separation stress is always lower than the stress necessary for fast separation.

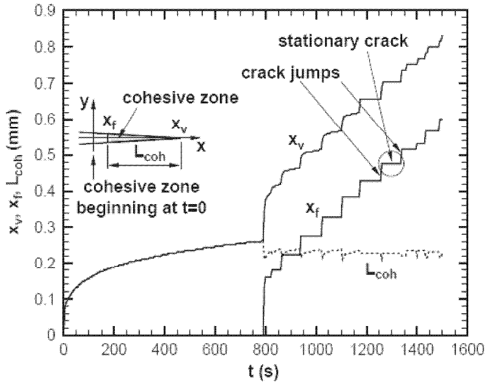

Figure 21 Cohesive zone modelling of step-wise hydrogen induced cracking [39].

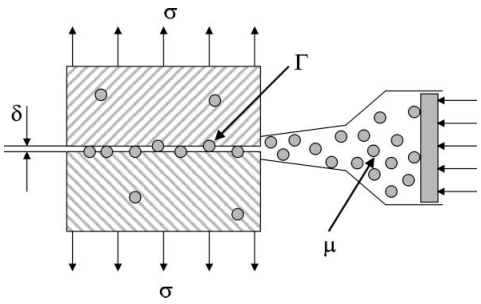

Figure 22 Interfacial region with impurities illustrated as a thermodynamic system in equilibrium with the bulk phase. μ is the chemical potential and Γ is solute concentration of the interface [42].

Given by a polynomial shaped TSL the maximum cohesive stress with hydrogen influence can be expressed as:

$$\text{Fast separation: } \sigma_c(\Gamma) = \left(\frac{16}{9\delta} \left[(2\gamma_{\text{int}})_0 - (\Delta g_i^0 - \Delta g_s^0)\Gamma_0 / \Gamma_{\max} \right] \right) \cdot \sigma_0 \tag{41}$$

$$\text{Slow sep.: } \sigma_c(\mu) = \left(\frac{16}{9\delta} \left[(2\gamma_{\text{int}})_0 - RT\Gamma_{\max} \ln\left\{ \frac{\left[1 + (m+1)(\Gamma_0 / \Gamma_{\max})\right]^2}{1 - (\Gamma_0 / \Gamma_{\max})} \right\} \right] \right) \cdot \sigma_0 \tag{42}$$

$m = \exp\left[(\Delta g_i^0 - \Delta g_s^0)/RT\right]$, where Δg_i^0 and Δg_s^0 are Gibbs energy for the interface and free surface respectively. Γ_0 is the initial and $\Gamma_{\max}$ the maximum interfacial concentration of hydrogen. By applying material specific values for the separation energy, Gibbs free energy, initial coverage of hydrogen $\Gamma_0/\Gamma_{\max}$ and a constant critical opening δ, relations for the hydrogen influenced cohesive stress are retrieved. Liang and

Sofronis [43] applied these equations for separation along a chromium carbide/fcc matrix (Nickel alloy 690). A range of polynomial TSLs for different hydrogen segregate concentration levels are presented in Figure 23.

Application of TSLs that vary with time as a function of the hydrogen content offers the possibility of doing transient calculations of the separating energy by taking the successive diffusion towards the crack tip into account.

To account for an additional softening effect of hydrogen on the surrounding material Liang & Sofronis [43] introduced a softening correction ($\xi \leq 1$) to the von Mises yielding in the bulk material to account for the hydrogen influence, ref. Eq. 28. Their results indicate that there is a synergistic effect of decohesion and softening of the adjacent material on the stress required for crack growth.

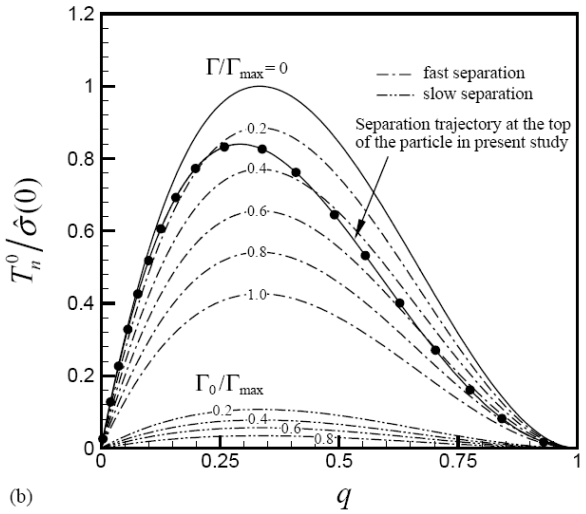

Figure 23 Hydrogen influenced traction separation laws. T^0_n is the normal component of the opening, q is an non-dimensional separation parameter and Γ/Γ_{max} the hydrogen coverage [43].

Based on the reviewed cohesive zone literature, a cohesive zone model with appropriate TSLs is regarded as suited to reproduce hydrogen assisted cracking. It must be emphasized that the method does not copy the actual micromechanisms but rather is a continuum based way of representing a complicated micromechanical situation. The main challenge will presumably be to identify the right TSLs for the material at hand.

For materials with different phase constituents, as SMSS and DSS representative TSL's for the ferrite and austenite phase should be aimed for. Atomistic calculations of the hydrogen induced effect on the required separation energy as performed by Jiang & Carter [40] are a first principle approach. Nano-mechanical testing during in situ charging as performed by Barnoush and Vehoff [37] can be an alternative method of retrieving local hydrogen influenced mechanical properties.

7 Summary

Reported hydrogen diffusion coefficients in supermartensitic, duplex and superduplex stainless steels from electrochemical permeation laboratory measurements, reflect large scatter in results. The diffusion coefficient is influenced by a range of external and internal parameters, as cathodic potential, temperature, surface oxide and deposit, material composition and microstructure. However, as long as the external parameters are carefully controlled and the material is well characterized, material specific relations for the diffusion coefficient as a function of these parameters can be established.

More scarcely reported is the effect of variations of material parameters on the hydrogen diffusion. It is however well known that the austenite – ferrite balance and the (rolling) direction of the austenite islands influences the diffusivity. Other material specific parameters as the austenite size, the austenite shape and the amount of precipitations are discussed but not systematically studied and needs further research effort.

The materials in question are often mechanically loaded under hydrogen exposure, introducing stresses and strains in the material. When sharp notches or cracks are present, the local stresses and strains can be very high. No present technique is established to measure the local hydrogen diffusion or content in such areas. However, if the "unloaded diffusion coefficient" is known, a modification of Fick's law introducing the effect of hydrostatic stress and strain can be used to calculate the local hydrogen concentration. The influence of hydrostatic stress on mass diffusion is included in commercial available FE-codes; the influence of strain is not.

The amount and localization of hydrogen in a sharp notch or crack will influence the mechanisms causing initiation of fracture. The dominating micro-mechanisms discussed in literature are hydrogen enhanced decohesion (HEDE) and hydrogen enhanced local Plasticity (HELP). HEDE favours brittle decohesion along grain boundaries or crystallographic planes and can be described by local elastic fracture mechanics criteria. HELP is a mechanism initiated by enhanced dislocation movement along crystallographic planes due to local softening by the atmosphere (stress field) surrounding the H-atoms. While HEDE represents the traditional view of hydrogen assisted fracture occurring in for instance high strength structural steel, HELP is more pronounced in ductile materials as stainless steels. However, several micro-mechanisms are probably working together during a hydrogen assisted fracture process. Knowledge of the actual hydrogen distribution along a crack front would help to identify the critical load parameters, whether it is the local plastic strain or the hydrostatic stress.

Fracture mechanics FE analysis couples the mechanical properties and/or fracture resistance to the local hydrogen content. Recent cohesive zone models, implements hydrogen by gradually decreasing the cohesive forces in the crack path due to increasing hydrogen content. If thoroughly verified by experimental testing, the cohesive zone modelling approach offers a possibility to bridge the gap between micro-mechanisms and global fracture.

Acknowledgements

This review was supported by an international joint industry project "Hydrogen Induced Stress Cracking II", founded by, Statoil, Norsk Hydro, Shell, BP, Chevron Texaco, ConocoPhillips, Total, Tenaris NKK Tubes, Outokompu, JFE, ATI Allegheny Ludlum and Sumitomo.

References

[1] Norsok M630, Material data sheets for piping, rev. 4, January 2004
[2] E. Owzcarek and T. Zakroczymski, Hydrogen transport in a duplex stainless steel, Acta Materiala 48 (2000) 3059-3070
[3] E. L. Beylegaard, Hydrogen transport in duplex stainless steels", PhD thesis, NTNU, 1996
[4] T. Zakroczymski, E. Owzcarek, Electrochemical investigation of hydrogen absorption in a duplex stainless steel, Acta Materiala 50 (2002) 2701-2713
[5] C P.D. Bilmes, M. Solani, C.L. Llorente, Characteristics and effects of austenite resulting from tempering of 13%Cr-NiMo martensitic steel weld metal, Materials Characterization 46 (2001) 285-296
[6] O. Akselsen and R. Aune, Cathodic Hydrogen effects in welding of Supermartensitic stainless steel, International Conference: Advanced Metallic Materials and their Joining, 25-27. October, 2004, Bratislava, Slovakia
[7] J. D. Fast, Gases in metals, Philips Technical Library, 1976
[8] J. Crank, The mathematics of diffusion, 2.ed, Clarendon Press, Oxford, 1975
[9] Ø. Grong, Metallurgical Modelling of Welding -2nd edition, The institute of Materials, 1997
[10] ABAQUS Version 6.5, Hibbit, Karlson & Sorensen, inc.
[11] Comprehensive Structural Integrity – Fracture of Materials from nano to macro, Vol. 6, Elsevier (2003) 65-101
[12] Y.D Park et al., Retained Austenite as a Hydrogen Trap in Steel Welds, Welding Journal, February (2002) 27-35
[13] P. Sofronis, R. M. McMeeking, Numerical analysis of hydrogen transport near a blunting crack tip, Journal of the Mechanics and Physics of Solids 37 (3), (1989) 317-350
[14] A.H.M. Krom, R.W.J. Koers, A. Bakker: Hydrogen transport near a blunting crack tip, Journal of the Mechanics and Physics of Solids, 47 (1999) 971-992
[15] R.A. Oriani, The diffusion and trapping of hydrogen in steel, Acta. Metall. Vol. 18 (1970) 147-157
[16] A. J. Kumnick, H.H. Johnson, Deep trapping states for hydrogen in deformed iron, Acta Materiala, Vol. 28 (1980) 33-39
[17] M. A. V Devanathan, Z. Stachurski, Adsorption and Diffusion of Electrolytic Hydrogen in Palladium, Proceedings of the Royal Society of London Series A, 270 (1962), p90 -
[18] British Standard BS 7886, Method of measurement of hydrogen permeation and the determination of hydrogen uptake and transport in metals by an electrochemical technique, uncontrolled licensed copy to Roy Johnsen, 2004

[19] A. Turnbull, E. L. Beylegaard and R. B. Hutchings, Hydrogen Transport in SAF 2205 and SAF 2507 Duplex Stainless Steels, Hydrogen transport and cracking in metals, Conference Proceedings, (1994) 268-279, The Institute of Materials,

[20] L. Scoppio, M. Bartheri, Methods of Hydrogen Uptake Measurements by Electrochemical Permeation Test on Low Alloy Steels, Hydrogen transport and cracking in metals, Conference Proceedings, The Institute of Materials, (1994) 204-215

[21] K. Banerjee and U.K. Chatterjee, Hydrogen permeation and hydrogen content under cathodic charging in HSLA 80 and HSLA 100 steels, Scripta Materiala 44 (2001) 213-216

[22] S. Mollan, Hydrogen embrittlement in 13 Cr Supermartensitic stainless steel due to cathodic protection, Diploma thesis, NTNU, 2003

[23] T. Hemmingsen et al., Hydrogen diffusion in 13%Cr Supermartensitic stainless steels. Experiences with the electrochemical hydrogen permeation cell, Stavanger University College, 1994

[24] P. Woolin and A. Gregori; Avoiding hydrogen embrittlement stress cracking of ferritic austenitic stainless steels under cathodic protection, in conference proceedings of OMAE04 Vancouver, Canada, 2004

[25] Gesnouin et al, Effect of post-weld heat treatment on the microstructure and hydrogen permeation of 13%CrNiMo steels, Corrocion Science 46 (2004) 1633-1647

[26] A.R. Troiano, The role of hydrogen and other interstitials in the mechanical behaviour of metals, 1959 Edward De Mille Campbell Memorial Lecture, Transactions of the ASM, Vol. 52 (1960) 54-80

[27] W.W. Gerberich, P. G. Marsh, J.W. Hoehn, Hydrogen induced cracking mechanism-are there critical experiments?, Hydrogen Effects in Materials, The Minerals, Metals & Materials Society, (1996) 539-551

[28] Y. Katz, N. Tymiak, W. W. Gerberich, Nanomechanical probes as new approaches to hydrogen/deformation interaction studies, Engineering Fracture Mechanics 68 (2001) 619-646

[29] H.K. Birnbaum , P. Sofronis, Hydrogen-enhanced localized plasticity-a mechanism for hydrogen-related fracture, Materials Science and Engineering, A176 (1994) 191-202

[30] Sofronis et al., Hydrogen induced shear localization of the plastic flow in metals and alloys, European Journal of Mechanics and Solids, 20 (2001) 857-872

[31] D. Delafosse, T. Magnin, Hydrogen induced plasticity in stress corrosion cracking of engineering systems, Engineering Fracture Mechanics 68 (2001) 693 – 729

[32] A. Taha and P. Sofronis, A micromechanics approach to the study of hydrogen transport and embrittlement, Engineering Fracture Mechanics 68 (2001) 803-837

[33] Y. Liang, P. Sofronis, N. Aravas, On the effect of hydrogen on plastic instabilities in metals, Acta Materiala 51 (2003) 2717-2730

[34] I.M. Robertson, The effect of hydrogen on dislocation dynamics, Engineering Fracture Mechanics 68 (2001) 671-692

[35] Oltra R., Bouillot C. and Magnin T., Scripta Mat., 35, 9, (1996), p. 1101.

[36] D. P. Abraham and C.J. Altstetter, The effect of Hydrogen on the Yield and Flow Stress of an Austenitic Stainless Steel, Metallurgical and materials transaction, 26A (1995) 2849-2858

[37] A. Barnoush, H. Vehoff: "Electrochemical nanoindentation: A new approach to probe hydrogen/deformation interaction, Scripta Materialia 55, 2006, p. 195-198

[38] D.S. Dugdale, Yielding of steel Sheets containing Slits, Journal of the Mechanics and Physics of Solids, 8 (1960) 100-104

[39] S. Serebrinsky, E.A. Carter, M. Ortiz, A quantum-mechanically informed continuum model of hydrogen embrittlement, Journal of the Mechanics and Physics of Solids 52 (2004) 2403-2430

[40] D.E. Jiang, E.A. Carter, "First principles assessment of ideal fracture energies of materials with mobile impurities: implications for hydrogen embrittlement of metals", Acta Materialia 52, 2004, p 4801-4807

[41] E. D. Hondros, M. P. Seah, "The theory of Grain Boundary Segregation in Terms of Surface Adsorption Analogues", Metallurgical Transactions A, Vol 8A, 1977, pp. 1363-1371

[42] J-S Wang, The thermodynamics aspect of hydrogen induced embrittlement, Engineering Fracture Mechanics 68 (2001) 647-669.

[43] Y. Liang, P. Sofronis, Toward a phonological description of hydrogen induced decohesion at particle/matrix interfaces, Journal of the Mechanics and Physics of Solids, 51 (2003) 1509-1531

Paper II

COHESIVE ZONE MODELING OF HYDROGEN INDUCED STRESS CRACKING IN 25%CR DUPLEX STAINLESS STEEL

Vigdis Olden/NTNU [1]/Sintef [2] **Christian Thaulow/NTNU [1]**

Roy Johnsen/NTNU [1] **Erling Østby/ Sintef [2]**

[1] Norwegian University of Science and Technology, Department of Engineering Design and Materials
[2] Sintef Materials and Chemistry, Department of Applied Mechanics and Corrosion

Hydrogen influenced cohesive zone elements are implemented in finite element models of rectangular notched tensile specimens of 25% Cr stainless steel. A three step procedure consisting of stress analysis, diffusion analysis and cohesive zone fracture initiation analysis is performed. A linear traction separation law gives good fit with experimental results for stress levels just below the material yield stress. Hydrogen concentration of 40 ppm at the surface and 1 ppm in bulk always gives crack initiation at the surface.

Keywords: Stainless steels; Cohesive zone modeling; Environmentally assisted cracking; Structural assessment; Pipelines

The occurrence of cracks in offshore structures and pipelines can cause catastrophic failures. Over the last years several incidents of hydrogen induced failure have been reported in subsea oil and gas pipelines and installations in the North Sea. There is a need of establishing reliable and practical test methods and implementing robust requirements in standards and guidelines for materials under hydrogen influence in oil and gas industry. An extra challenge in testing of hydrogen induced stress cracking (HISC) is the time aspect. Due to very slow hydrogen diffusion rates in stainless steel, laboratory testing aimed for material qualification can be a demanding task.

The present work describes how hydrogen diffusion modeling and cohesive zone modeling (CZM) can offer a supplement to laboratory material qualification.

Two of the most established micromechanical models of hydrogen assisted fracture are the hydrogen enhanced decohesion model (HEDE) and the hydrogen enhanced local plasticity model (HELP). In both models hydrogen fracture is regarded as a result of a critical combination of stress, strain and hydrogen concentration, but the proposed mechanisms for crack initiation and growth are basically different.

The hydrogen enhanced de-cohesion mechanism was first proposed by Troiano in 1960 [1] and further developed by Oriani et al [2] and Gerberich et al [3]. HEDE is based on the hypothesis that interstitial hydrogen lowers the cohesive strength by dilatation of the

This paper is written in letter format i.e. without headings which is the format applied by Scripta Materialia

atomic lattice and hence lowers the fracture energy. This implies that hydrogen decreases the energy barrier for either grain boundary or cleavage plane decohesion.

Hydrogen enhanced local plasticity (HELP) is characterized by atomic hydrogen that enhances the mobility of dislocations through an elastic shielding effect in preferred crystallographic planes at the crack tip causing locally reduced shear strength. This "local softening" results in cracking by micro void coalescence along these planes. The mechanism was first introduced by Birnbaum and co-workers in 1990 [4].

The cohesive element can be pictured as two faces separated by a thickness, which is close to zero. The relative motion of the top and bottom faces in the thickness direction represents opening or closing of the interface. The relevant constitutive "material" response is a traction-separation description; an evaluation which gives the amount of energy required to create new surfaces. A traction separation law (TSL) is a function described by the cohesive stress (σ) and separation (δ). The area below the curve represents the separation energy, Γ_c. There are a variety of shapes of the TSL reported by different authors. [5]. Hydrogen influence can be build into the TSL represented by a gradually decrease in the separation energy with increasing hydrogen content.

Recent approaches in cohesive modeling of hydrogen assisted fracture are represented by Serebrinsky, Carter & Ortiz [7] who have implemented the HEDE approach with a brittle TSL response. In the present work the approach as described by Serebrinsky et al. has been applied for the prediction of hydrogen induced crack initiation a 25% Cr stainless steel. A linear law for separation of the atomic lattice is applied [9].

$$\sigma(\delta) = \sigma_c\left(1-\frac{\delta}{\delta_c}\right) \; for\; \delta \langle\; \delta_c, \;\; otherwise\; 0 \tag{1}$$

This implies that the TSL (on an atomic level) is rigid up to a critical stress σ_c and subsequently drops linearly down to zero upon the attainment of a critical δ_c. Serebrinsky, Carter & Ortiz [7] suggests the following relation for the coupling between hydrogen coverage, θ, and the critical hydrogen dependent cohesive stress, σ_c (θ):

$$\frac{\sigma_c(\theta)}{\sigma_c(0)} = 1 - 1.0467\theta + 0.1687\theta^2 \tag{2}$$

The relation is based on a fitting of surface energy values calculated by Jiang and Carter [10]. σ_c (0) is the critical cohesive stress without hydrogen influence. Hydrogen coverage is defined as a function of the hydrogen concentration and the Gibbs free energy difference between the interface and the surrounding material as expressed in the Langmuir-McLean isotherm [10]:

$$\theta = \frac{C}{C + \exp(-\Delta g_b^0 / RT)} \tag{3}$$

Where C is the hydrogen concentration (ppm), Δg_b^0 is Gibbs free energy-difference between surface and bulk (kJ/mol), R is the gas-constant (8.3142 J/mol K) and T is the temperature (K).

The hydrogen influenced TSL is implemented as a 2D user defined cohesive element and described in a FORTRAN sub routine. A modification of the cohesive element developed by Scheider [11] is applied. The element definition requires a nonzero value for the opening at the critical traction stress, hence a very small value $\delta_1 = 1.0 \cdot 10^{-7}$mm is set, see Figure 2. Crack initiation is defined as the achievement of zero stress and critical opening (δ_c) in the first cohesive element.

The ruling equation for stress driven diffusion given in ABAQUS [12] is:

$$J = -sD\left(\frac{\partial \phi}{\partial x} + \frac{\kappa_p \partial p}{\partial x}\right) \tag{4}$$

Where J is the hydrogen flux, s is the solubility of hydrogen in Fe, D is the hydrogen diffusion coefficient ϕ is the normalized hydrogen concentration C/s and x is the position in the body. κ_p is the stress factor linked to gradients in equivalent stress ($\partial p/\partial x$). The mass conservation equation requires:

$$-\frac{\partial}{\partial x} \cdot J = \frac{\partial C}{\partial t} \tag{5}$$

Inserting Eq. (4) into Eq. (7) and using ϕ=C/s gives a modified Ficks' law with respect to hydrostatic stress:

$$\frac{\partial C}{\partial t} = D \cdot \left[\frac{\partial^2 C}{\partial x^2} + \kappa_p \cdot \frac{\partial C}{\partial x} \cdot \frac{\partial p}{\partial x} + \kappa_p \cdot C \cdot \frac{\partial^2 p}{\partial x^2}\right] \tag{6}$$

As far as possible material and diffusion data representative of 25% Cr duplex stainless steel are used in the FE model. Supplementary input data for other types of steel are used when no data for 25% Cr duplex steel are available.

The cohesive model is calibrated using data from laboratory testing of 25% Cr duplex steel [13]. A comparison between the predicted time to fracture and the time to fracture observed in the laboratory specimens is the main objective.

The simulations are performed in three steps: 1) Stress analysis without hydrogen influence to generate stress fields to be read by diffusion model, 2) Transient diffusion analysis with stress driven diffusion. The analyses give the hydrogen distribution to be read into the cohesive elements, 3) Stress analysis using hydrogen dependent user defined cohesive elements in the crack path.

The material model represents a 25% Cr duplex stainless steel. Young's modulus is taken as 200000MPa and Poisson's ratio ν is 0.3. The yield stress is 600MPa defined at 0.5% total strain.

The samples thickness is 12 mm, the width 9 mm and the length 120 mm. The notch depth is 1.5 mm for the V-notch and 2.0 mm for the U-notch. In the cohesive model 4-node linear cohesive elements with a length of Δ=10μm are defined at a path along the x-axis starting from the bottom of the notch through the cross-section of model. The element mesh in the notch area is presented in Figure 1.

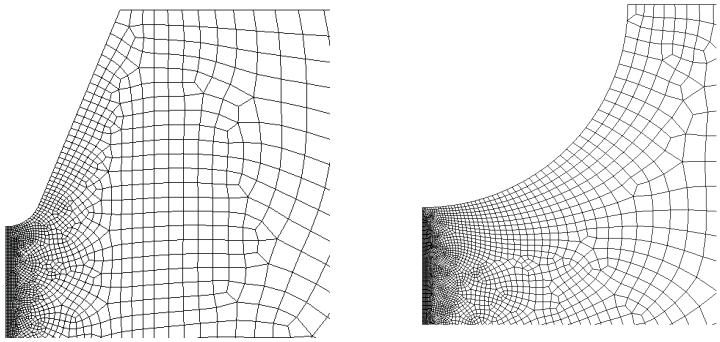

Figure 1 Element mesh in notch area a) V-notch b) U-notch

In the elastic plastic stress analysis and the cohesive analyses a constant uniaxial tension stress of 485, 510, 540 and 570MPa are used, which represents from 80% to 95% of the yield stress. As a reference also zero stress level cases are investigated in the diffusion analyses.

Selected input parameters for the diffusion analyses are presented in Table 1. Note that solubility of hydrogen in ferritic steel is chosen. This is based on the assumption that cracking initiates in ferrite. The diffusion coefficient is calculated from regression equations for lattice diffusion in a 25%Cr steel published by Turnbull et al.[14].

Table 1 Input parameters for the diffusion analyses.

Solubility s ppm·mm·N^{-} $^{1/2}$	Diff. coeff. D mm^2·s^{-1}	Gibbs free energy Δg_b^0 kJ/mol	H. bulk conc. c_0 ppm	H. surf. conc. c_s ppm	Temp T °C	Stress. conc. factor κ_p mm· N$^{-1/2}$
0.033 [1)]	3.6·10^{-11} [2)]	30 [7]	1	40	4	8.68·10^{-4}· ϕ

1) Value given for 2.25Cr-1Mo steel [16]
2) Lattice diffusion in SDSS at 4°C, A. Turnbull [14]

A bulk hydrogen concentration of 1ppm is chosen. A constant hydrogen concentration of 40ppm is applied on all outer surfaces. The temperature of 4°C is representative of the pipes outer surface in subsea conditions. The value of κ_p refers to Eq. (6). The maximum diffusion time is 10000 hours (~416 days). The diffusion time is chosen based on the maximum duration of the laboratory tests.

The laboratory samples were submerged in 4°C 3.5 wt% NaCl solution with a cathodic potential (CP) of -1050 mV $_{SCE}$.

The applied linear cohesive law described by Eqs. (1), (2) and (3) (see Figure 2.) requires values for critical traction stress, critical separation and knowledge of the hydrogen distribution in the prescribed crack path. With reference to Serebrinsky et al. [7] and Tvergaard & Hutchinson [15] the critical cohesive strength $\sigma_c(0)$ without hydrogen influence is taken as $3.5 \cdot \sigma_y$ giving 2100MPa. A critical opening (δ_c) of $2.0 \cdot 10^{-4}$ mm is chosen based on a fitting procedure to the experimental results. Remember also the initial onset value $\delta 1 = 1.0 \cdot 10^{-7}$mm at the critical stress.

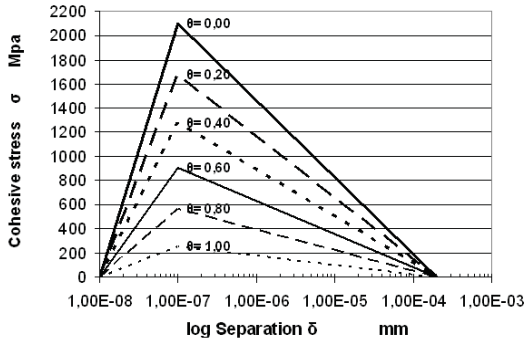

Figure 2 Traction separation law for different levels of hydrogen coverage.

The resulting normal stress distributions in front of the notches for different load levels are given in Figure 3. The stress peak is higher and is observed closer to the surface for the V-notch (0.31-0.33mm) than for the U-notch (1.0-1.4mm). This is consistent with the higher stress concentration for this geometry.

Minimal difference in the calculated hydrogen profile is observed for the two models and the four different stress levels after 100 hours; see Figure 4. The effect of the load levels on the hydrogen distribution is marginal also for l0000 hours.

Time to crack initiation is calculated as a function of stress level for both geometries. The overall results are presented as a function of net section stress in Figure 3. As expected the V-notch initiates after a shorter time than the U-notch and time to initiation decreases with increasing stress level.

At the time when cracking initiates the activated cohesive zone length is 0.05-0.06 mm. Figure 6 shows the opening of the cohesive elements near the surface ranging from the

chosen maximum critical opening value of δ_c=0.0002mm at the surface down to a minimum value below $1.0 \cdot 10^{-7}$ mm about 0.05 mm into the material. Despite that the stress peak is localized a distance ahead of the notch tip, crack initiation always occur in the element closest to the surface. This is due to the high surface hydrogen concentration that lowers the critical traction stress.

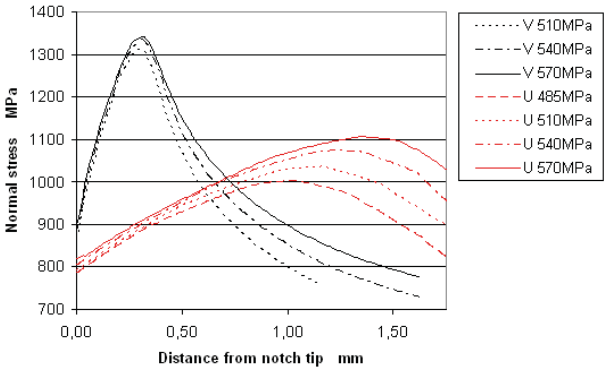

Figure 3 Normal stress distribution in front of the V-notch and U-notch tip for gross stress levels of 485-570MPa.

According to Eq. (3) an applied hydrogen concentration of 40 ppm represents a coverage of θ=0.948. In accordance with Eq. (2) this amount of coverage gives a critical traction stress of 335 MPa. This implies that separation in the first element starts as soon as the surface hydrogen is applied in the model. The neighboring elements are activated successively by the diffusing hydrogen. The simulations clearly indicate that the surface hydrogen rather than the hydrostatic stress controls the crack initiation.

The situation differs completely if the bulk material is pre-charged with hydrogen. This is illustrated in Figure 7, where a simulated case of the U-notch at 570 MPa gross stress is plotted for a constant bulk level of 10 ppm hydrogen. The critical separation is now reached below the surface at the location of the normal stress peak. This indicates that in a combined situation with hydrogen pre-charging and surface hydrogen during tensile loading, a competition between surface and sub surface crack initiation will occur.

It may be argued that a hydrogen level of 40 ppm is not representative of the initiation of fracture in the ferrite phase. Supersaturated ferrite seldom contains more than 10 ppm hydrogen [17] and hence, this would be a more realistic value for the effective hydrogen that contributes to the lowering of the critical traction stress.

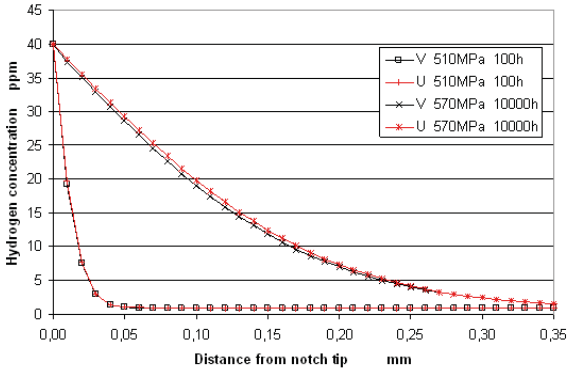

Figure 4 Distribution of calculated hydrogen concentration in front of the V- and U-notch after 100 and 10000 hours.

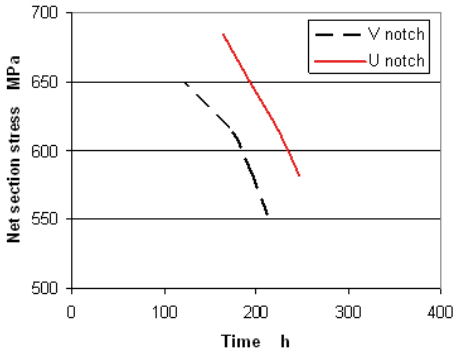

Figure 5 Time to crack initiation as a function of geometry and net section stress.

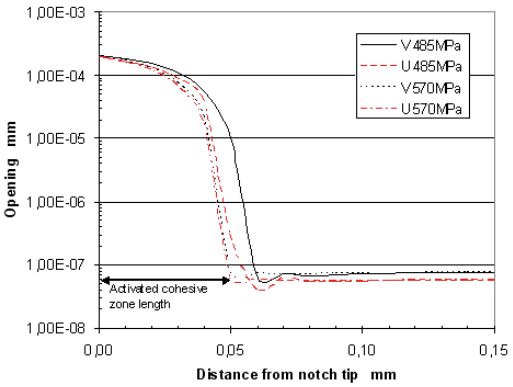

Figure 6 Separation along the cohesive element path for the U- and V-notch at the highest and lowest applied gross stress level.

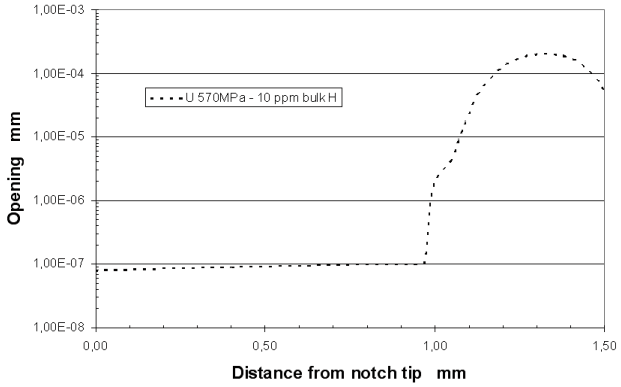

Figure 7 Separation along the cohesive element path for the U-notch 570 MPa case with 10 ppm hydrogen in bulk.

The hydrogen influenced fracture initiation energy can be calculated from the TSL:

$$G_{HISC} = \frac{1}{2}\sigma_c \cdot \delta_c \tag{7}$$

Further, the hydrogen influenced fracture initiation toughness can be found by the established relation:

$$G_{HISC} = \frac{K_{HISC}^2}{E/(1-\nu^2)} \tag{8}$$

Recall that 40 ppm hydrogen yields a 335 MPa critical initiation traction stress at the surface. The critical separation value is 0.0002 mm, giving a K_{HISC} of 2.7 MPa$\sqrt{}$m. 10 ppm hydrogen gives σ_c= 536 MPa and a K_{HISC} of 3.4 MPa$\sqrt{}$m. These very low values represent the required stress intensity for the initiation of a 10μm surface micro-crack in the ferrite.

The values correspond well with measured and predicted K_{Ith} for hydrogen charged Fe-3%Si sheet reported by Gerberich and colleagues [3]. Note however that in an experimental situation a micro crack is not necessarily a critical event. The crack may be arrested in the austenite. However, more likely is a stepwise cracking process until final fracture at a critical crack length occurs.

Figure 8 shows a picture of surface cracks in a U-notch specimen. The middle and upper right crack have been arrested in the austenite while the lower left crack has propagated in the ferrite.

Time to surface crack initiation is compared to experimental results in Figure 9. The simulations reveals a steeper negative slope than the experiments, hence there is a reasonable good estimation for the 510 MPa and the 540 MPa cases, while it tend to overestimate the time to fracture for the 570MPa case and to underestimate the 485MPa

case. However, the presented results indicate that the applied TSL with small adjustments of $\sigma_c(0)$ and δ_c can be applied to predict the time to failure for the presented material.

The presented study have shown that hydrogen dependent cohesive elements can be implemented in the crack path of ABAQUS models of U- and V-notched tensile specimens.

Hydrogen diffusion modeling with a hydrogen source of 40 ppm applied evenly on the specimen surfaces and a tension stress level in the range 485-570 MPa reveals little effect of the stress level on the hydrogen distribution within the simulated time range of 10000 hours. There is a tendency that the U-notch yields higher concentration values in the crack path than the V-notch.

A linear traction separation law, with an initial traction stress of $\sigma_c(0)$= 3.5·yield stress and a critical separation of 0.0002 mm gives reasonably good fit with experimental results for gross stress levels of 0.85 – 0.9 times the yield stress.

A hydrogen concentration of 40 ppm at the surface and 1 ppm in bulk always gives crack initiation at the surface despite the peak normal stress localized a short distance in front of the notch tip. The hydrogen influenced critical traction stress is 335 MPa giving initiation fracture toughness K_{HISC} of 2.7 MPa$\sqrt{m}$, which represents the initiation of a surface micro-crack.

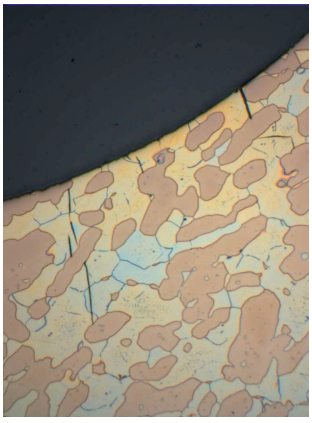

Figure 8 Surface cracks in a U-notch specimen.

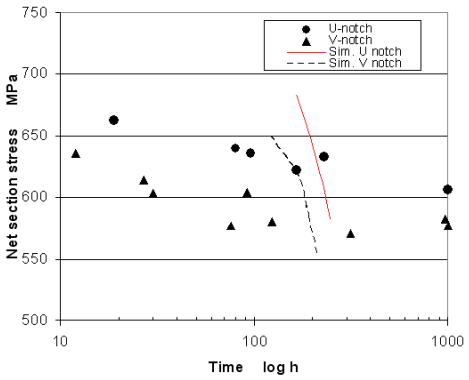

Figure 9 Time to crack initiation and fracture – comparison between experiments and simulations.

The authors wish to express their thanks to the HISCII project for access to internal project reports and results. HISCII is funded by, Statoil, Norsk Hydro, Shell, BP, Chevron Texaco, Conoco Phillips, Total, Tenaris NKK Tubes, Outokompu, JFE, ATI Allegheny Ludlum and Sumitomo.

[1] A.R. Troiano, Transactions of the ASM, Vol. 52, 1960, pp 54-80
[2] R.A. Oriani, Acta. Metall. 18, 1970, pp 147-157,
[3] W.W. Gerberich, P. G. Marsh, J.W. Hoehn, Hydrogen Effects in Materials, The Minerals, Metals & Materials Society, 1996, pp 539-551
[4] H.K. Birnbaum , P. Sofronis, Materials Science and Engineering, A176, 1994, pp 191-202
[5] W. Brocks, A. Cornec and I. Scheider, Comprehensive Structural Integrity , Vol 3: Numerical and Computational Methods, 2003, pp 127-209
[6] V. Olden, C. Thaulow and R. Johnsen,:, Sintef Report STF80MK A07026, 2007
[7] S. Serebrinsky, E.A. Carter, M. Ortiz, Journal of the Mechanics and Physics of Solids, 52, 2004, pp 2403-2430
[8] Y. Liang, P. Sofronis, Journal of the Mechanics and Physics of Solids, 51, 2003, pp 1509-1531
[9] O. Nguyen, M. Ortiz, Journal of the Mechanics and Physics of Solids, 50, 2002, pp 1727-1741
[10] D.E. Jiang, E.A. Carter, Acta Materiala 52, 2004, pp 4801-4807
[11] I. Scheider, Technical report, GKSS internal report no WMS/2000/19.
[12] ABAQUS, Version 6.5, Users' manual, ABAQUS Inc. 2004
[13] R. Johnsen,B. Nyhus, S. Wästberg and G. Ø. Lauvstad, paper no. 07496, NACE 07, Nashville, March 2007
[14] Turnbull, E. Lembach-Beylegaard, R.B. Hutchings, In A. Turnbull (Ed.), Hydrogen Transport and Cracking in Metals, The Institute of Materials, Cambridge, UK, pp 268-279
[15] V. Tvergaard, J.W. Hutchinson, Journal of the Mechanics and Physics of Solids, 40 (6), 1992, pp 1377-1397
[16] ABAQUS, Version 6.3, Example problems manual, Hibbitt, Karlsson & Sorensen Inc., 2002
[17] Ø. Grong: Metallurgical Modelling of Welding, 2 ed., The Institute of Materials, 1997, pp 513-14

Paper III

APPLICATION OF HYDROGEN INFLUENCED COHESIVE LAWS IN THE PREDICTION OF HYDROGEN INDUCED STRESS CRACKING IN 25%CR DUPLEX STAINLESS STEEL

Vigdis Olden[1,2] **Christian Thaulow**[1]

Roy Johnsen[1] **Erling Østby**[2] **Torodd Berstad**[2]

[1] NTNU, Norwegian University of Science and Technology, Faculty of Engineering Science and Technology, Department of Engineering Design and Materials, NO-7465 Trondheim, Norway
[2] Sintef, Institute of Materials and Chemistry, Department of Applied Mechanics and Corrosion, NO-7465 Trondheim, Norway

Abstract

Cohesive zone finite element modeling is applied in the simulation of hydrogen induced stress cracking in 25%Cr duplex stainless steel. Hydrogen influence is implemented in linear and polynomial cohesive laws. Suitability of the laws in prediction of hydrogen induced stress cracking is investigated by applying models of U and V-notched tensile specimens representing a 25%Cr duplex stainless steel component submerged in sea water under cathodic protection (CP). Fracture prediction is performed by a three step procedure; elastic plastic stress analysis, stress assisted hydrogen diffusion and cohesive stress analysis. Local cohesive stress fields as well as the time to fracture initiation are investigated as a function of the shape of the traction separation laws and the element size for three levels of tensile stress. Simulated results are also compared with results from laboratory tensile tests and discussed with respect to the suitability of describing fracture initiation and fracture mechanism of the steel. The results show that the polynomial law and a mesh size of 0.5 μm gives the most accurate description of the local cohesive stress field. The simulated time to fracture is closest to laboratory test results for stresses of 0.85-0.9 times the yield strength.

Keywords: Stainless steels; Cohesive zone modeling; Environmentally assisted cracking; Structural assessment; Pipelines

1 Introduction

A challenging problem in the framework of finite element analysis is the prediction of failure in materials and structures. In later years the cohesive zone modeling (CZM) technique has become greatly facilitated and gained renewed interest in the field of fracture modeling.

Nomenclature

bcc	body centred cubic crystallographic structure
CP	cathodic protection
CZM	cohesive zone modelling
FE	finite element
HEDE	hydrogen enhanced decohesion
HELP	hydrogen enhanced local plasticity
HISC	hydrogen induced stress cracking
SCE	saturated calomel electrode
TSL	traction separation law
C, C_E, C_{Ni} c_0, c_s	hydrogen concentration: general, average in FE element, in nodes, in bulk, sub-surface
D	diffusion coefficient
E	Young's modulus
Δg_b^0	Gibbs free energy difference
J	hydrogen flux
k_{IH}	local hydrogen induced stress intensity/fracture toughness
K_{IC}	limit stress intensity
K_{Ith}, K_{HISC}	threshold stress intensity: general, HISC-induced
p	hydrostatic stress
R	gas constant
s	solubility
t	time
T, T^Z	temperature, absolute temperature
V_H	partial molar volume of hydrogen in iron
α	ferrite
α'', β'	fitting parameters
δ, δ_1, δ_N, δ_T,	separation of cohesive element: general, at critical stress of linear law, normal, transverse,
δ_c, δ_M	critical separation in normal direction, maximum value for transverse separation
Δ	element mesh length
ϕ, ϕ_0	normalized hydrogen concentration: in stressed state, in unstressed state
γ	austenite
γ(0), γ(θ)	surface energy: without hydrogen influence, with hydrogen influence
Γ, Γ_c, Γ_{HISC}	cohesive energy: general, critical, HISC related
κ_p	stress factor in diffusion
ν	Poisson's ratio
σ_y	yield stress
σ, σ(δ), σ_N, σ_T, σ_M	cohesive stress, general, normal, transverse, maximum value for transverse stress
σ_c, $\sigma_c(0)$, $\sigma_c(\theta)$	critical cohesive stress: general, without hydrogen influence, with hydrogen influence
θ	hydrogen coverage

Fracture takes place at an interface of cohesive zone elements embedded in a finite element model; no continuum elements are damaged in a cohesive model. In this respect the method is effective in fracture modeling of large geometries. The cohesive elements can be pictured as two faces separated by a thickness, which is close to zero. The relative motion of the top and bottom faces in the thickness direction represents opening or closing of the interface.

The relevant constitutive "material" response is a traction-separation description; an evaluation which gives the amount of energy required to create new surfaces. A traction separation law (TSL) is a function described by the cohesive stress (σ) and separation (δ). The area below the curve represents the cohesive energy, Γ_c. There are a variety of shapes of the TSL proposed by different authors. Two TSL's will be applied in the present paper, see Figure 1. Nguyen & Ortiz [1] has suggested a linear decreasing law for separation of the atomic lattice of steel. The 1D formulation is:

$$\sigma(\delta) = \sigma_c\left(1 - \frac{\delta}{\delta_c}\right) \; for\, \delta \langle\, \delta_c, \;\; otherwise \; 0 \tag{1}$$

This implies that the TS is rigid up to a critical stress σ_c and subsequently drops linearly down to zero upon the attainment of a critical δ_c, see Figure 1a. The linear TSL was initially introduced by Hillerborg et al. [2] in 1976 for brittle fracture in concrete and rock. The separation energy for the cohesive element is simply described by:

$$\Gamma_c = \frac{1}{2}\sigma_c\delta_c \tag{2}$$

The other TSL is a polynomial function (Figure 1b) proposed for fracture in ductile materials first introduced by Needleman in 1987 [3] and further developed by Tvergaard [4]:

$$\sigma(\delta) = \frac{27}{4}\sigma_c\frac{\delta}{\delta_c}\left(1 - \frac{\delta}{\delta_c}\right)^2 \; for\, \delta \langle\, \delta_c, \;\; otherwise \;\; 0 \tag{3}$$

The separation energy for the polynomial description is calculated from:

$$\Gamma_c = \frac{9}{16}\sigma_c\delta_c \tag{4}$$

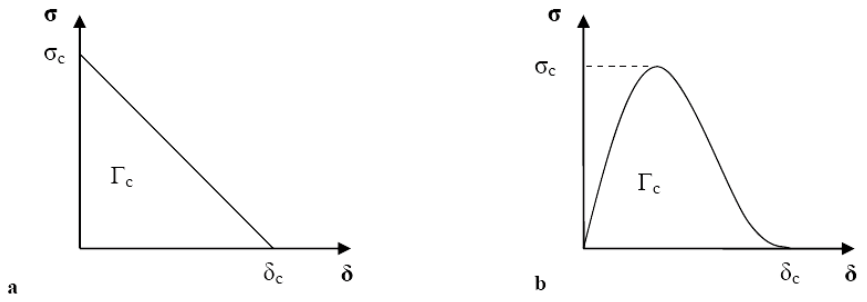

Figure 1 Traction separation laws a) linear b) polynomial.

Control of hydrogen induced stress cracking (HISC) is of major importance in keeping the structural integrity of oil and gas sub-sea pipelines and structures under acceptable risk level. Absorbed hydrogen developed from cathodic protection has contributed to a large amount of cracking incidents in recent years. What makes the CZM technique especially interesting in this respect is the possibility of implementing hydrogen affected TSL's that represents hydrogen degradation of the material. This offers the possibility of simulating processes that are extremely time-consuming to reproduce in the laboratory.

HISC fracture is a result of interconnected mechanisms involving electrochemistry, diffusion, metallurgy, fracture micro mechanisms and external load. Up to the present date the hydrogen assisted local fracture mechanisms in the vicinity of a crack are not well understood. It is important to point out that CZM does not in itself describe complex micromechanical and hydrogen interactions. The fracture energy of the TSL must represent the effect of these complex processes. However, if correct input is given, CZM represents a possible way of bridging the gap between micromechanical processes and macroscopic behavior of a structure.

This article proposes a method including CZM for prediction of HISC fracture in a 25%Cr duplex stainless steel. First a short presentation of two micromechanical views of hydrogen assisted fracture is presented. Further, a description of the model including the theoretical background of the diffusion and cohesive formulations related to hydrogen will be presented. In the final part a comparison between simulations and experimental test results will be discussed. The main objective of the presented work is to investigate the influence of the TSL-shape and the cohesive element size on the description of the local stress field and the time to fracture initiation. The suitability of the method in the prediction of fracture initiation in 25%Cr duplex stainless steel will also be evaluated.

2 Micro-mechanisms of hydrogen assisted fracture

Two of the most established micromechanical models of hydrogen assisted fracture are the hydrogen enhanced decohesion model (HEDE) and the hydrogen enhanced

local plasticity model (HELP). In both models hydrogen fracture is regarded as a result of a critical combination of stress, strain and hydrogen concentration, but the proposed mechanisms for crack initiation and growth are basically different.

2.1 Hydrogen enhanced de-cohesion - HEDE

The HEDE mechanism was first proposed by Troiano in 1960 [5] and further developed by Oriani et al. [6] and Gerberich et al. [7]. HEDE is based on the hypothesis that interstitial hydrogen lowers the cohesive strength by dilatation of the atomic lattice and hence lowers the fracture energy. This implies that hydrogen decreases the energy barrier for either grain boundary or cleavage plane decohesion. The notion is that fracture will initiate in the area of maximum hydrostatic stress some distance ahead of the crack tip. Gerberich et al. [7] introduced the concept of local hydrogen induced fracture toughness k_{IH} at the crack tip that scales with the yield stress, $\sigma_{y,}$ and the hydrogen induced threshold stress intensity K_{Ith} :

$$K_{I_{th}} = \frac{1}{\beta'} \exp\left\{ \frac{\left(k_{IH}\right)^2}{\alpha'' \sigma_y} \right\} \tag{5}$$

Values β’ and α’’ are fitting parameters determined by finite element (FE)-calculations and fracture mechanical tests.

2.2 Hydrogen enhanced local plasticity - HELP

HELP is characterized by atomic hydrogen that enhances the mobility of dislocations through an elastic shielding effect in preferred crystallographic planes at the crack tip causing locally reduced shear strength. This “local softening” results in cracking by micro void coalescence along these planes. A HELP crack will tend to initiate from slip planes at the crack tip.

The mechanism was first introduced by Birnbaum and co-workers in 1990 [8]. Later Sofronis [9] and Delafosse & Magnin [10] have quantified the stress field surrounding the hydrogen atoms causing enhanced dislocation glide. Robertson [11] has reported experimental “evidence” of HELP by in situ observations of plastic deformation of thin samples in a high voltage transmission electron microscope and found an increasing amount of dislocation pile ups in AISI 310s stainless steel when introducing hydrogen.

3 Cohesive zone modeling approach to hydrogen assisted stress cracking

Hydrogen influence can be build into the TSL represented by a gradually decrease in the separation energy with increasing hydrogen content. Recent approaches in cohesive modeling of hydrogen assisted fracture are represented by Serebrinsky et al. [14] who have implemented the HEDE approach using the brittle linear decreasing TSL.

Liang and Sofronis [15] use a polynomial TSL and also introduce a hydrogen dependant softening parameter to the material surrounding the cohesive elements in an effort to combine local softening and de-cohesion (HELP+HEDE).

Serebrinsky et al. [14] suggest the following relation for the coupling between hydrogen coverage, θ, and the surface energy with hydrogen influence, γ(θ), for bcc Fe:

$$\gamma(\theta) = (1 - 1.0467\theta + 0.1687\theta^2)\gamma(0) \tag{6}$$

γ(0) is the surface energy without hydrogen. The relation is based on a fitting of surface energy values calculated by Jiang and Carter [16], where the surface energy without hydrogen influence, γ(0), is 2.43 J/m^2. Based on this relation and given a constant critical opening δ_c, the expression given for the local critical hydrogen dependent cohesive stress, σ_c (θ), yields:

$$\frac{\sigma_c(\theta)}{\sigma_c(0)} = 1 - 1.0467\theta + 0.1687\theta^2 \tag{7}$$

σ_c (0) is the local critical cohesive stress without hydrogen influence. Hydrogen coverage is defined as a function of the hydrogen concentration and the Gibbs free energy difference between the interface and the surrounding material as expressed in the Langmuir-McLean isotherm [17]:

$$\theta = \frac{C}{C + \exp(-\Delta g_b^0 / RT)} \tag{8}$$

Where C is the hydrogen concentration (ppm), Δg_b^0 is Gibbs free energy-difference between surface and bulk (kJ/mol), R is the gas constant (8.3142 J/mol K) and T is the temperature (K).

Based on the assumption that hydrogen assisted fracture in duplex stainless steel initiates in the ferrite (bcc), eq. (7) and (8) are implemented in the model. Crack initiation is defined as the achievement of zero stress and critical opening (δ_c) in the first cohesive element.

3.1 Implementation of hydrogen assisted cohesive elements in ABAQUS

Two dimensional user defined cohesive elements are implemented in ABAQUS Standard using a FORTRAN sub-routine initially developed by Scheider [13].

In the cohesive stress analysis the hydrogen concentration must be given for the nodes connected to the cohesive elements as part of the input to the finite element analysis. Based on the hydrogen concentration for the four nodes C_{Ni} connected to an element a mean concentration C_E for the cohesive element can be calculated as

$$C_E = \frac{1}{4}\sum_{i=1}^{4} C_{Ni} \tag{9}$$

The hydrogen coverage in the element is then calculated by Eq. (8) (C is replaced with C_E) and the critical cohesive stress in pure tension for the element is calculated by Eq. (7). Based on the normal separation δ_N in the cohesive element, which is the difference of the displacement of the adjacent continuum elements, a normal stress in the cohesive element is calculated by Eq. (3) for the polynomial TSL and by a modification of Eq. (1) for the linear TSL. The modification of the linear TSL is given by an initial "stiffness" defined by a linear increasing part up to a separation value of δ_1 followed by the linear decreasing part until the critical separation δ_c is reached resulting in a bi-linear shape (see also Figure 5a).

$$\sigma_N = \begin{cases} \sigma_c \dfrac{\delta_N}{\delta_1} & \delta_N < \delta_1 \\ \sigma_c \left(\dfrac{\delta_c - \delta_N}{\delta_c - \delta_1} \right) & \delta_1 < \delta_N < \delta_c \end{cases} \tag{10}$$

To obtain a shape of the TSL as similar to the linear one as possible a value of δ_1 close to zero is chosen. When the normal separation δ_N has reached the value of δ_c, the element looses the ability to carry load in both the normal and the transverse direction. In the current work the stresses in the normal and transverse direction for the cohesive element are calculated independent of each other. The shear traction is calculated from the tangential separation and given as a linear law:

$$\sigma_T = \sigma_M \frac{\delta_T}{\delta_M} \tag{11}$$

where δ_T is the transverse separation, σ_M and δ_M are input parameters for the actual TSL. The shear traction is independent of the hydrogen concentration and in the current work no unloading in the shear direction of the cohesive element are implemented.

3.2 Stress-assisted hydrogen diffusion

The governing equation for the stress driven diffusion given in ABAQUS [18] is:

$$J = -sD\nabla\left(\phi + \kappa_p \cdot p\right) \tag{12}$$

Where J is the hydrogen flux, s is the solubility of hydrogen in Fe, D is the hydrogen diffusion coefficient ϕ is the normalized hydrogen concentration C/s. κ_p is the stress factor to be linked with gradients in hydrostatic stress , ∇ p , and is expressed as:

$$\kappa_p = \frac{\bar{V}_H \phi}{R(T - T^z)} \tag{13}$$

Where $\overline{V}_H$ =2.0x10^3 mm^3/mol is the partial molar volume of hydrogen in iron-based alloys [19]. T^Z is the absolute zero temperature (0K or -273°C). The normalized concentration ϕ is dependent on the hydrostatic stress p:

$$\phi = \phi_0 \exp\left(\frac{-\overline{V}_H p}{R(T - T^Z)}\right) \tag{14}$$

ϕ_0 is the normalized hydrogen concentration in the unstressed state.

The mass conservation equation requires:

$$\frac{\partial C}{\partial t} = -J \cdot \nabla \tag{15}$$

Inserting Eq. (12) into Eq. (15) and applying s · ϕ = C gives a modified Ficks' law with respect to hydrostatic stress:

$$\frac{\partial C}{\partial t} = D\nabla^2 C + D \cdot \frac{V_H}{R \cdot \left(T - T^Z\right)} \nabla C \nabla p + D \cdot \frac{V_H}{R \cdot \left(T - T^Z\right)} C \nabla^2 p \tag{16}$$

4 Finite element case study

The geometries representing rectangular tensile specimens with a single U-shaped and V-shaped notch are investigated. Whenever possible, material and diffusion data representative of 25% Cr duplex stainless steel are used in the FE models. These data are retrieved partly from laboratory material testing [20] and partly from literature [14][19][21]. Supplementary input data for other types of relevant steel are used when no data for 25% Cr duplex stainless steel were available.

The finite element simulations are performed in three steps in ABAQUS Standard:

1. Elastic plastic stress analysis without hydrogen influence to generate stress fields to be used as input in the diffusion model.
2. Transient diffusion analysis with stress driven diffusion. The analyses give the hydrogen distribution to the cohesive elements.
3. Elastic plastic stress analysis using hydrogen dependent user defined cohesive elements in the crack path.

The same mesh is applied in all three steps. In the stress analysis 4 node bilinear plane strain elements are used. In the cohesive analysis user defined cohesive elements are added in the crack path perpendicular to the surface, describing a 1.5-2 mm path into the material from the notch tip. For the diffusion analysis 4 node linear mass diffusion

elements are applied. The investigated cohesive element mesh lengths in the crack path are Δ=0.5 μm, 5 μm, 10μm and 20 μm.

4.1 Material

The material model represents a typical 25% Cr duplex stainless steel. The yield stress defined at 0.5% total strain, is 600MPa. Young's modulus is taken as 200000MPa and Poisson's ratio ν is 0.3.

4.2 Geometry

The thickness of the modeled specimens is 12 mm and the length 120 mm. The V-notch depth is 1.5 mm and the notch radius 0.25 mm. Notch depth (and radius) for the U-notch is 2.0 mm. Due to symmetry only half the sample is modeled, see Figure 2. Close up of the mesh in the notch tip area of the V-notch model with a cohesive element size of 0.5 μm is shown in Figure 3. The location of the cohesive elements is marked with crosses. The total number of nodes/elements ranges from approx. 10500/10250 for the coarser mesh models up to 27800/26000 for the 0.5μm models.

4.3 Load

In the elastic plastic stress analysis and cohesive analyses constant gross uniaxial tension stresses of 485, 540 and 600MPa are applied, which represents from 80% to 100% of the yield stress. Typical service stress levels for sub-sea oil and gas pipelines are in the range 60% – 80% of the yield stress.

4.4 Hydrogen related parameters

Selected input parameters for the diffusion analyses are presented in Table 1. Note that solubility of hydrogen in ferrite steel is chosen. This is based on the assumption that cracking initiates in ferrite. The solubility of hydrogen in austenite steel is about 1000 times higher than the solubility of hydrogen in ferrite steel [19]. The diffusion coefficient is calculated from regression equations for lattice diffusion in a 25%Cr duplex stainless steel published by Turnbull et al. [21].

A bulk hydrogen concentration of 1 ppm is chosen. This value represents the hydrogen level in the steel in the as delivered condition. A constant hydrogen concentration of 10 ppm is applied on all outer surfaces. This hydrogen level is based on an assumed maximum supersaturated level in the ferrite [22]. The temperature of 4°C is representative of the outer surface of the pipes in sub-sea conditions. The value of κ_p refers to Eq. (13). The maximum simulated diffusion time in the diffusion analysis is 1000 hours.

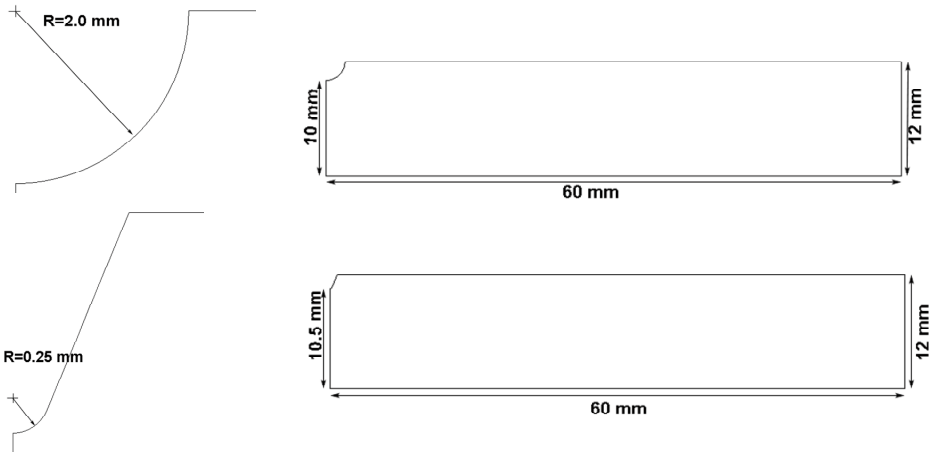

Figure 2 Geometry of the U and V-notched tensile specimen models.

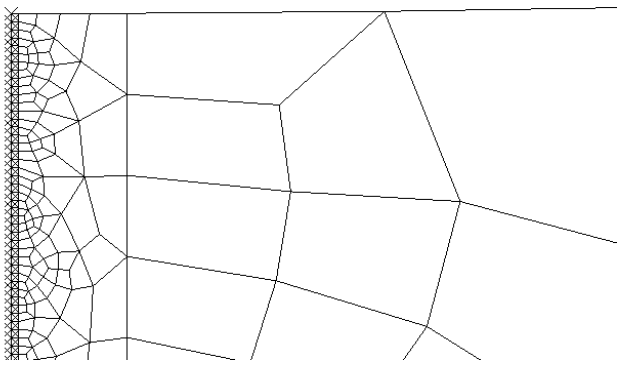

Figure 3 Close up of mesh at the V-notch tip with a cohesive element size of 0.5 μm.

4.5 Traction separation law (TSL)

The applied cohesive laws described by equations (3), (7), (8) and (10) require values for separation and critical cohesive stress and knowledge of the hydrogen distribution in the prescribed crack path. With reference to Serebrinsky et al. [14] and Tvergaard & Hutchinson [23] the critical cohesive strength $\sigma_c(0)$ without hydrogen influence is taken as $3.5 \cdot \sigma_y$ giving 2100MPa. Based on a fitting procedure to the experimental results separation values of $\delta_c = 2.0 \cdot 10^{-4}$ mm for the linear law and $\delta_c = 1.78 \cdot 10^{-4}$ mm for the polynomial law were chosen. For the linear law a "stiffness" value δ_1 of $1.0 \cdot 10^{-7}$ mm was applied. (Varying δ_1-values in the range $1.0 \cdot 10^{-10}$- $1.0 \cdot 10^{-6}$ mm gave no influence on the results). The initial cohesive energy for both applied TSL's is Γ_c = 210 J/m^2. The critical separation values represent a δ_c/Δ ratio in the range of

0.0089 - 0.4 for the applied cohesive mesh sizes. The relation between the hydrogen surface concentration and hydrogen coverage in Eq. (8) is graphically shown in Figure 4. Figure 5 gives the traction separation laws for different levels of hydrogen coverage for the linear TSL (Figure 5a) and the polynomial TSL (Figure 5b).

Table 1 Input parameters for the diffusion analyses.

Solubility s ppm·mm·N$^{-1/2}$	Diffusion coefficient D mm^2·s^{-1}	Gibbs free energy Δg_b^0 kJ/mol	Hydrogen concentration in bulk c_0 ppm	Sub-surface hydrogen concentration c_s ppm	Temperature T °C
0.033 [1)]	2.9·10^{-10} [2)]	30 [14]	1	10	4

1) Value given for 2.25Cr-1Mo steel [19]
2) Lattice diffusion in 25%Cr duplex stainless steel at 4°C, A. Turnbull [21]

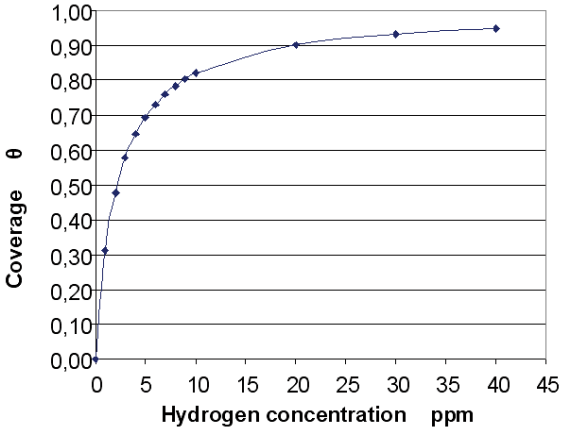

Figure 4 Relation between hydrogen concentration and hydrogen coverage.

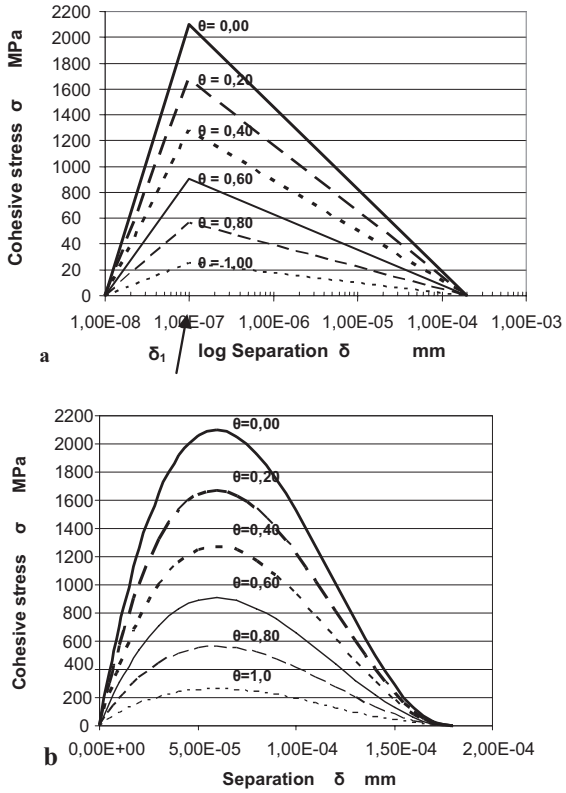

Figure 5 Applied traction separation laws for different levels of hydrogen coverage. a) Linear law b) Polynomial law

5 Results

5.1 Stress analyses

The normal stress is extracted from the nodes in the symmetry plane. The stress distributions in front of the notch tip for different levels of gross stress are given in Figure 6 a. The stress peak is higher and is observed closer to the notch tip for the V-notch (0.31-0.33mm) than for the U-notch (1.0-1.5mm). This is consistent with the higher stress concentration for the V- notch geometry. There is a small mesh size effect on the notch tip stress level, see Figure 6 b.

5.2 Diffusion analyses

The diffusion analyses are evaluated for the influence of stress level, geometry and mesh size. The resulting hydrogen profiles in a 0.05 mm linear path in front of the notch are plotted for the 485 MPa, and the 600 MPa case after 100 and 1000 hours (see Figure 7).

There is no visible effect of the stress level on the hydrogen distribution for the evaluated load cases. A small effect is however present when comparing with the unloaded case; the nonzero stress cases produce a somewhat higher hydrogen concentration than the unloaded case after 1000 hours, see Figure 9.Minimal difference in the calculated hydrogen profiles is also observed between the two geometries, see Figure 8.

The effect of mesh size on the hydrogen concentration is presented for the V-notch model and element sizes 10 μm and 0.5 μm in Figure 9. The only visible effect after 100 hours of diffusion is in the resolution of the curves.

The fact that there is no significant influence of stress on the diffusion of hydrogen concentration is due to the large gradients of hydrogen concentration close to the surface. This is far more influential than the gradients of equivalent stress, see Eq. (12). Eq. (13) gives a pressure stress factor κ_p of 0.26 $mmN^{-1/2}$ for a hydrogen concentration of 10 ppm, which illustrates the insignificant influence of the pressure part of the diffusion equation.

The effect of plastic strain rate on trapping of hydrogen is not incorporated in the present diffusion analyses but will also influence the hydrogen distribution. Taha and Sofronis [24] performed FE simulations of hydrogen diffusion in front of a rounded notch (R=0.25 mm) of four-point bend fracture toughness specimen of high and low strength steel. The initial bulk and surface hydrogen concentrations were identical in these simulations. The authors found that trapping due to plastic strain close to the surface and trapping in lattice due to hydrostatic stress were competing mechanisms. Because hydrogen needs time to diffuse towards the hydrostatic stress field, trapping due to plastic strain was the dominating mechanism for all cases after short times of diffusion (in their case seconds). When the applied nominal stress was above the yield stress and the strain was equal to or larger than 2.3%, trapping was the ruling mechanism also for longer times. The diffusion driven by the hydrostatic stress field was the most influential mechanism at lower stresses and strains and longer diffusion times. When the nominal stress was close to the yield stress, as in our study, the resulting maximum hydrogen concentration due to trapping and hydrostatic stress was about 3 times the initial concentration in both cases.

Based on the study of Taha and Sofronis [24], we may assume that the plastic strain effect will add to the effect of a large chemical potential at the surface. In the present analyses the hydrogen level given at the surface is already at a maximum concentration level for ferrite and it can be argued that due to the much higher solubility of hydrogen in this phase the increase in hydrogen level will primarily take place in the austenite. In our model cracking is defined to initiate in the ferrite, hence an increased trapping of hydrogen in the surface austenite will not be relevant to the present cohesive analysis.

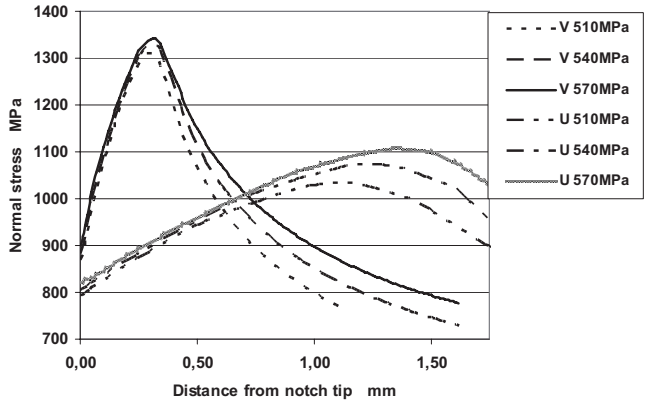

a)

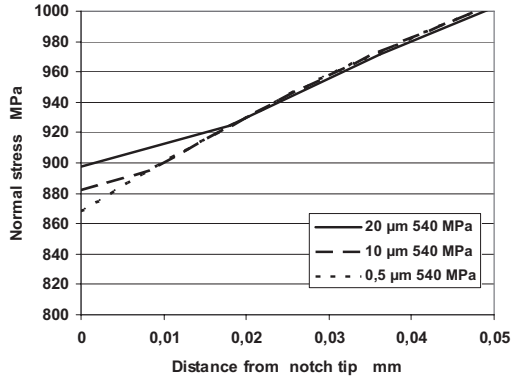

b)

Figure 6 Normal stress distribution in front of the notch. a) U and V-notch model, gross stress levels of 485-600 MPa b) Effect of mesh size close to the surface for the V-notch model at 540 MPa gross stress.

Very different levels of sub surface concentrations for duplex steel are reported in literature. Turnbull et al [21] report a hydrogen level of approx. 0.0014 ppm at 25°C in the ferrite phase of a duplex stainless steel. This is close to the theoretical solubility of atomic hydrogen in the iron lattice. For similar steel under comparable conditions Zakroczymski and Owczarek [24] have determined a value that is about 60000 times higher. Adding the uncertainty regarding the effect of surface stress and strain on the hydrogen uptake, correct sub-surface hydrogen content for the model is not a simple pick. The basis for our choice is the range of analytical hydrogen content in ferrite steel of 1-10 ppm given by Grong [22].

Due to the lack of suitable methods of local hydrogen measurements the assumed subsurface hydrogen levels and calculated local hydrogen concentrations near a notch or a crack tip can not be verified. This is a main obstacle that should be addressed to improve the accuracy in FE simulations of hydrogen diffusion.

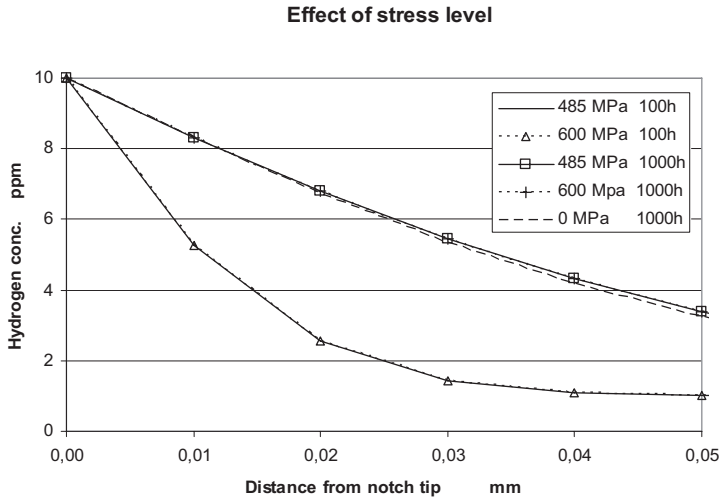

Figure 7 Hydrogen concentration profile in a linear path in front of the notch - effect of gross stress level

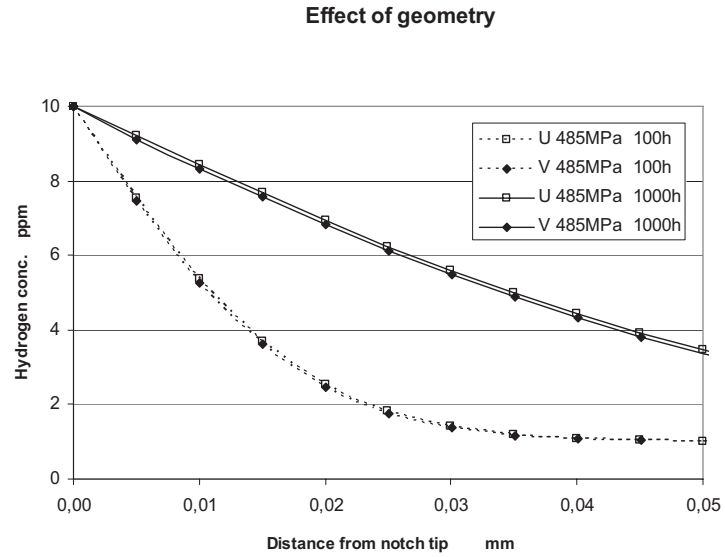

Figure 8 Hydrogen concentration profile in a linear path in front of the notch - effect of geometry.

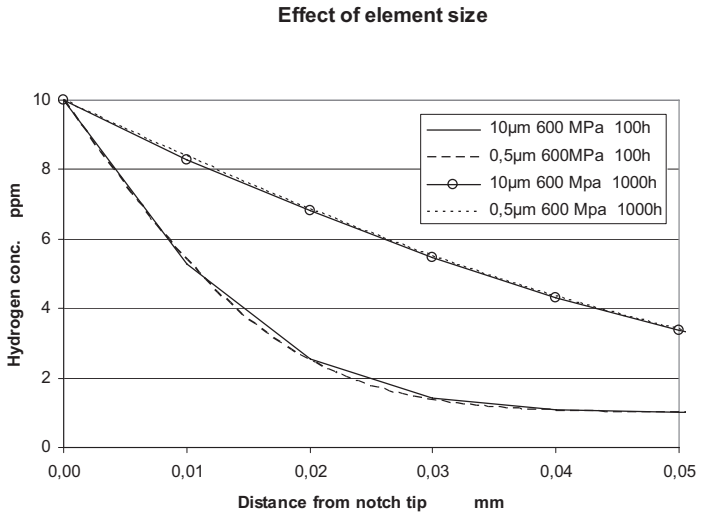

Figure 9 Hydrogen concentration profile in a linear path in front of the notch - effect of element size.

5.3 Cohesive analyses

A summary of the cohesive results are presented in Figure 10 a-b. Times to fracture are plotted as a function of applied stress, for both TSL formulations and all mesh sizes. Note that the results are plotted as a function of the net section stress, i.e. the stress in the cross-sectional area below the notch. The U-notch (Figure 10 a) yields a higher net section stress for the same applied gross stress than the V-notch (Figure 10 b) due to a smaller net sectional area (notch depth: U =2.0 mm, V=1.5 mm).

The overall tendency for both geometries is that the fracture initiation time decreases with an increase in stress level. The effect is more pronounced for the U-notch than the V-notch. It is also evident that the U-notch yields longer initiation times than the V-notch. The initiation always occurs at the surface.

For the U-notch model, the polynomial TSL increases the time to fracture initiation compared to the linear TSL. For the V-notch however, a clear tendency in this respect can not be observed.

The mesh size also affects the results. A 20 µm mesh clearly yields the earliest fracture for both geometries. For the U-notch there is however little influence from mesh size on the time to fracture initiation for Δ=10 µm or smaller. There is somewhat more scatter in the V-notch results, but it can be argued that the results for Δ=5 µm and Δ=0.5 µm only yield insignificant differences.

Evaluation of the cohesive stress fields show that at the point of fracture initiation, the cohesive zone is activated reaching 0.02 – 0.03 mm from the notch tip into the material. A local stress peak is observed at the end of the activated zone. It is evident that a 0.5

μm mesh gives the best resolution of the local stress peak. See Figure 11-12 for plots of the local stress field of the U- and V-notch. Mesh sizes of 5 μm and above do not sufficiently resolve the local stress peak. For the linear TSL and mesh sizes larger than 5 μm fluctuations in the cohesive stress that is not observed for the polynomial TSL appear. Finally, the plots show that except for the 20 μm mesh results the linear TSL exhibits higher maximum cohesive stresses than the polynomial TSL.

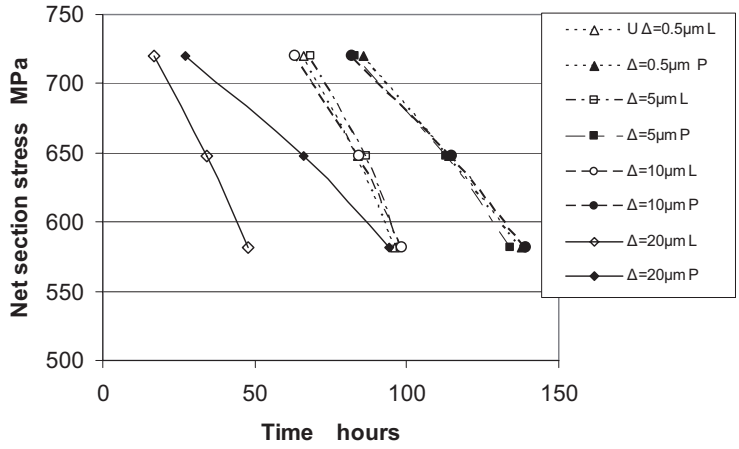

a)

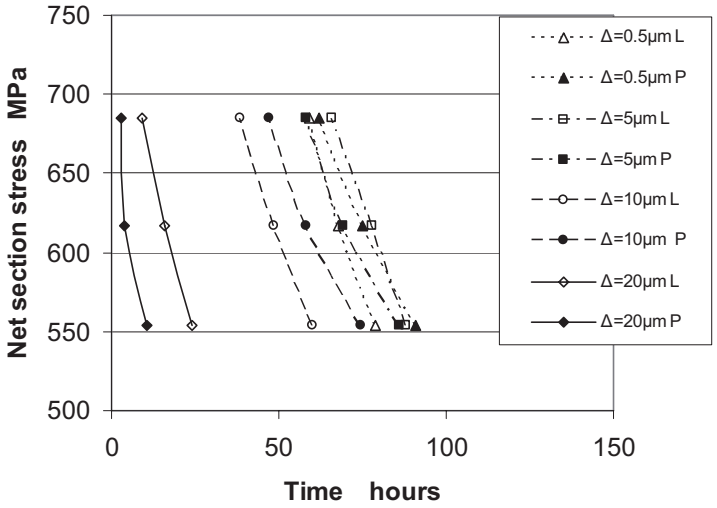

b)

Figure 10 Time to fracture initiation as a function of stress level for linear TSL (L) and polynomial TSL (P) and mesh sizes Δ=0.5 μm, 5 μm, 10 μm and 20 μm. a) U-notch b) V-notch

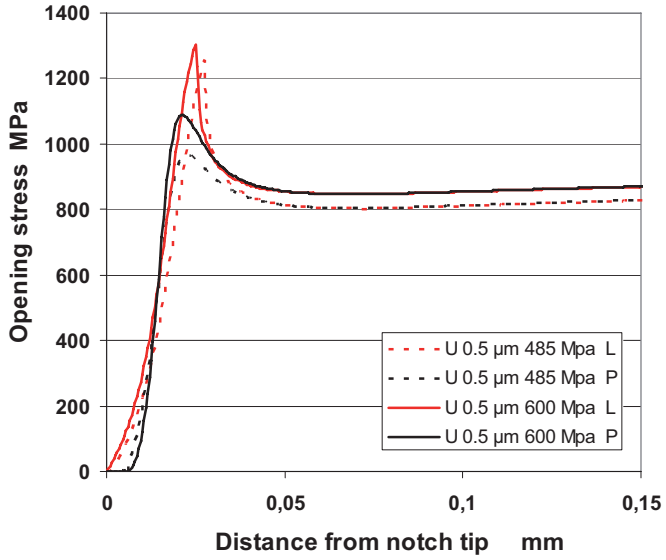

a)

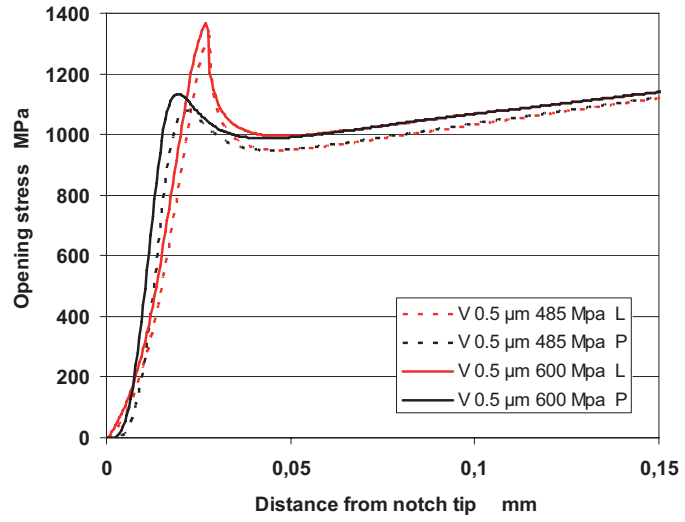

b)

Figure 11 Opening stress in the cohesive zone at the initiation of fracture at gross stress levels of 485 MPa and 600 MPa using linear (L) and polynomial (P) TSLs and a mesh size of Δ=0.5 µm. a) U-notch b) V-notch

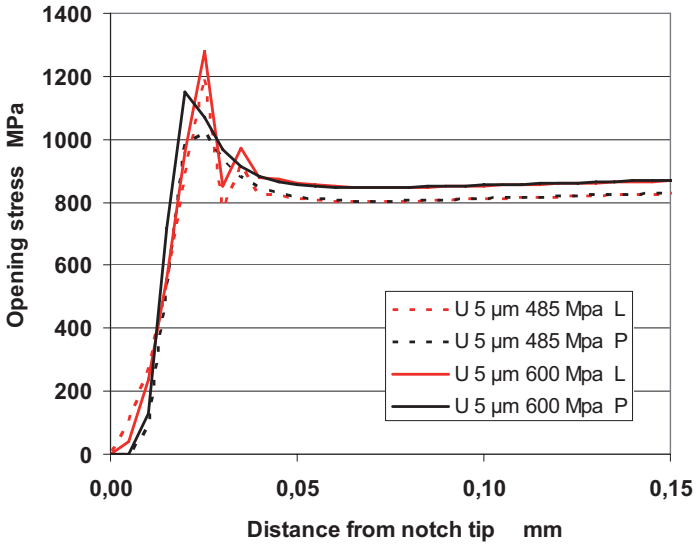

Figure 12 Opening stress in the cohesive zone of the U-notch at the initiation of fracture at gross stress levels of 485 MPa and 600 MPa using linear (L) and polynomial (P) TSLs and a mesh size of Δ=5 µm.

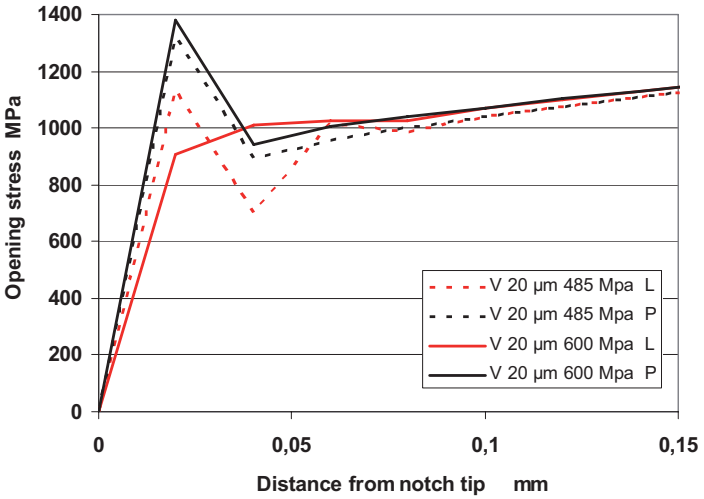

Figure 13 Opening stress in the cohesive zone at the initiation of fracture of the V-notch at gross stress levels of 485 MPa and 600 MPa using linear (L) and polynomial (P) TSLs and a mesh size of Δ=20 µm.

The fact that the fracture initiation occurs at the surface even if the gross stress peak is located ahead of the notch is due to the lowering of the critical stress caused by the

high hydrogen concentration. According to Eq. (7) and (8) a hydrogen concentration of 10 ppm yield a critical stress of σ_c= 536 MPa, which is well below the stress level at the notch tip, see Figure 6. At the location of the stress peak, the hydrogen concentration is not high enough to lower the critical hydrogen induced stress below the maximum level from the stress analyses. This implies that separation of the first element initiates at the notch tip as soon as hydrogen is applied on the model surface. The neighboring elements are successively activated by the diffusing hydrogen. The simulations clearly indicate that the surface hydrogen rather than the hydrostatic stress controls the crack initiation.

The reduction in initiation time with increasing stress and increasing stress concentration (U→V-notch) is as expected. Note that the dependency of applied stress is somewhat weaker in the V-notch, which can be related to the smaller difference in stress level close to the surface for the different levels of applied stress in this geometry, see Figure 6.

Extensive studies of the influence of the shape of cohesive elements have not been found in the literature. However, the shape effect is generally reported to be weak [12]. The difference in initiation time between the two TSL's in the U-notch model is therefore somewhat surprising. A main difference between the applied linear and polynomial law is the larger separation value at the point of critical cohesive stress in the polynomial law; hence more time is needed to reach σ_c. This will also affect the maximum cohesive stress level; longer available diffusion time yield higher hydrogen concentration and a lower maximum cohesive stress. The reason that the tendency is much clearer for the U-notch than the V-notch is connected with the general effect of a lower surface stress level; longer time is needed to obtain the sufficient energy to initiate fracture.

It is likely that the local stress field fluctuations observed using the linear TSL and $\Delta \geq$ 5 μm affect the time to crack initiation. The scatter in results for the V-notch model is an indication of this. The polynomial TSL seems more stable and hence a better choice for prediction of HISC cracks within the present model.

The very poor resolution of the cohesive stress field for the 20 μm mesh probably explains the discrepancy in the 20 μm results, see Figure 13. The tendency for the V-notch model to be more mesh dependent can be explained by the higher stress concentration in the local stress field ahead of the activated cohesive zone, requiring a better resolution of the local stress field than in the larger notch. In their cohesive crack analyses Tvergaard and Huchinson [23] used a δ_c/Δ ratio of 0.1. In the present case this would imply an element size of 2 μm. Our results suggest that the element size should be smaller than 5 μm (or $\delta_c/\Delta > 0.04$) to sufficiently resolve the local cohesive stress field. The results are in line with a study by Camacho and Ortiz [26] suggesting that the element size should be smaller than the cohesive zone length to achieve a satisfactory resolution of the crack tip stresses and a correct description of the damage process.

6 Comparison with laboratory tensile HISC testing

Test specimens with U and V-notch made from 25%Cr duplex stainless steel with dimensions similar to the models described above, were exposed in 3.5% NaCl solution at 4°C. The specimens were cathodically protected to -1050 mV $_{SCE}$ and kept under constant tensile load [20]. Measured time to fracture for the U and V-notched specimens are plotted in Figure 14 along with the simulated result using a polynomial TSL and Δ= 0.5 μm. Simulated results for 10 ppm and 7 ppm surface hydrogen concentration are compared with the experiments. The experimental results are plotted as open (V-notch) and filled (U-notch) diamond shaped dots and a logarithmic trend curves.

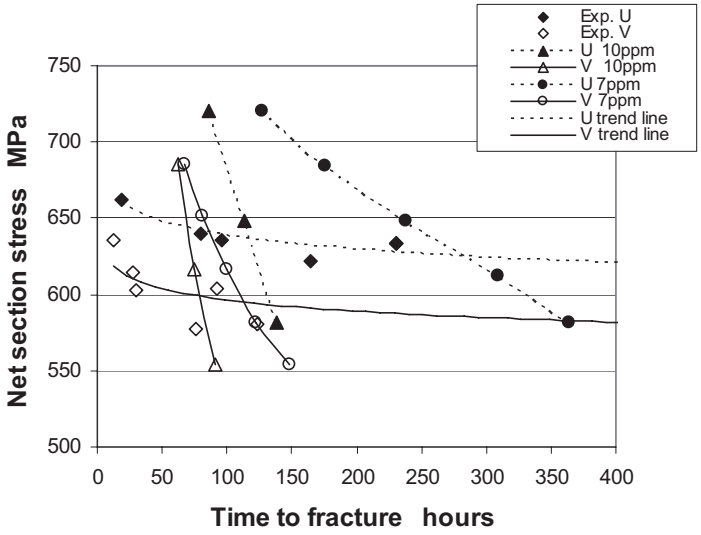

Figure 14 Comparison between simulated and experimental results of time to fracture (polynomial TSL and Δ=0.5 μm).

The simulated results for 10 ppm hydrogen exhibit a steeper negative slope than the experiments; hence they show less sensitivity to stress level and time. Somewhat better estimates are obtained for a hydrogen concentration of 7 ppm. The stress sensitivity is however still is too low compared with the experiments.

7 Discussion

The critical hydrogen influenced separation energy calculated from Eq. (5) using σ_c= 536 MPa (for 10 ppm H) and δ_c=0.000178 mm yields Γ_{HISC} = 53.6 J/m^2. Using the well established relation between fracture energy and stress intensity for the plane strain condition:

$$\Gamma_{HISC} = \frac{K_{HISC}^2}{E/(1-\nu^2)} \tag{17}$$

a K_{HISC} value of 3.4 MPa√m is calculated. This very low value represents the threshold stress intensity for the initiation of a surface micro-crack in the ferrite. Reported hydrogen influenced threshold stress intensities for duplex stainless steel in sea water has not been found. However, the value corresponds well with measured and predicted K_{Ith} (by eq. 5) for hydrogen charged Fe-3%Si single crystals reported by Gerberich and colleagues [7].

It is important to point out that in an experimental situation a micro crack in duplex stainless steel is not necessarily a critical event. The crack may be arrested in the more ductile austenite or more likely propagate in a stepwise manner until final fracture at a critical crack length occurs. This can be illustrated by the cracks in a U-notch specimen registered as "not failed" in the laboratory tests, see Figure 15. Note also that all micro-cracks are located close to or at the surface, whereas no cracks are present at the location of the global stress peak approx. 1 mm in front of the notch tip. This strongly suggests that the micro cracking have initiated at the surface in the ferrite phase (light phase). If the whole model (both bulk and surface) is given an even 10ppm hydrogen concentration, representing a pre-charged case, the initiation is predicted to occur at the location of the stress peak, see Figure 16. This was investigated by the authors in a previous paper [27].

The laboratory samples registered as failed (and plotted in Figure 14) were either totally fractured or had visible surface cracks and therefore are more representative of a fracture limit state. This also can also be taken as an indication that brittle HEDE description not alone induces hydrogen fracture in duplex stainless steel. As proposed by Delafosse and Magnin [10] it is likely that coexistence between the two mechanisms is present in the sense that HEDE rules fracture in ferrite and HELP is the main fracture mechanism in austenite.

To obtain a better match between the simulated and experimental results and thus be able to predict fracture for a duplex stainless steel on larger scale, modifications of the relation between critical stress and hydrogen coverage, (Eq. 7), should probably be performed. Laukkanen et al. [28] have simulated the hydrogen assisted crack susceptibility of multi-pass steel welds using an exponential TSL and a critical cohesive stress taken as a function of hardness (from Vickers hardness indentations) and the calculated hydrogen content.

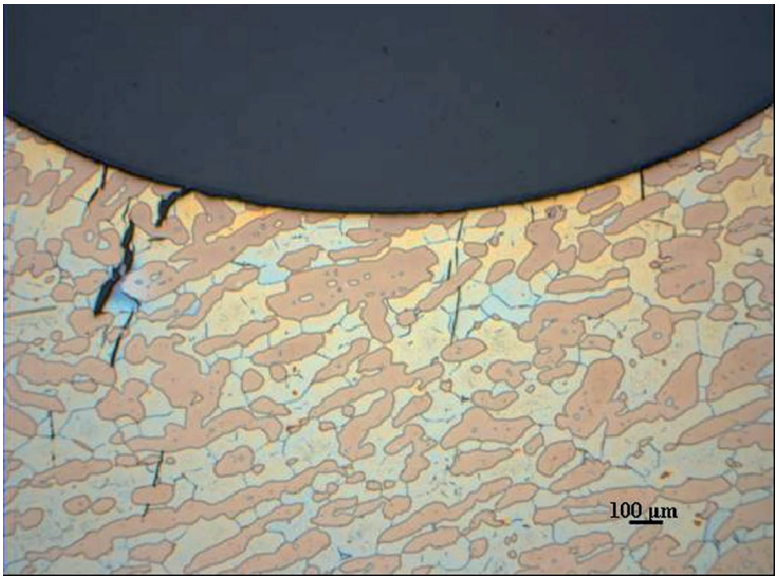

Figure 15 Surface cracks in ferrite (light phase) in a U-notch specimen of a 25%Cr duplex stainless steel regarded as “not failed” after constant tensile loading with hydrogen exposure for 44 hours. Net section stress: 540 MPa, Environment: 3.5% NaCl solution, 4°C, -1050 mV_{SCE}

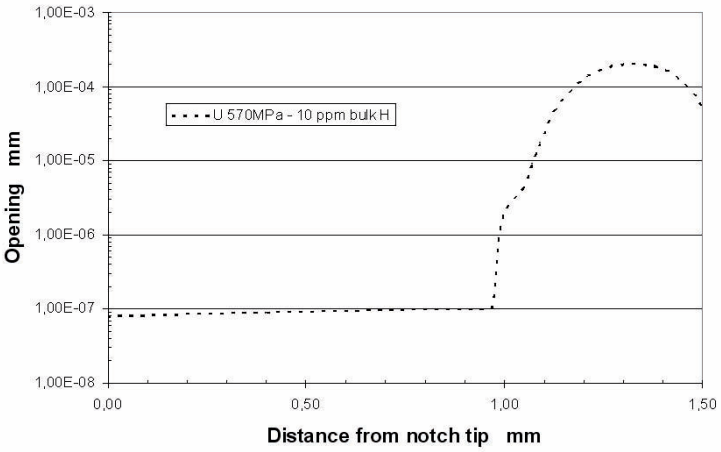

Figure 16 Distribution of the opening of the cohesive elements in front of the crack tip of a pre-charged U-notch specimen loaded at 570MPa. The critical opening of $2.0 \cdot 10^{-4}$ mm is obtained at the stress peak, approximately 1.35 mm ahead of the notch tip [27].

This approach is clearly based on a larger view of the material properties compared to the first principles relation in Eq. (7). In our case a relation that is able to take into account the effect of hydrogen on the critical hydrogen influenced cohesive stress of austenite would be preferable. A suitable approach may be offered by using the nano

mechanical indentation technique. With this method the local hydrogen affected mechanical properties in ferrite and austenite can be measured separately. Controlled nano indentations of the ferrite and austenite phase in duplex stainless steel have not been found in literature.

Further, reported results from nano mechanical testing of austenite material exposed to hydrogen are somewhat divergent. Katz et al. [29] have found an *increase* in the yield strength as well as a tendency of fewer but larger localized slip bands in stainless AISI 316 with increasing pre exposure to hydrogen. The authors argue however that the increased yield strength for AISI 316 may be due to martensite transformation caused by the indentations and may therefore not be representative for the actual yield. By performing nano indentations on nickel exposed to hydrogen in situ Barnoush and Vehoff [30] have found a 28% reduction in the local shear strength. It seems that further experiments can be helpful in quantifying the effect of hydrogen on the yield strength of ferrite and austenite. Simulating the HELP mechanism by including softening of the elasto-plastic constitutive law due to hydrogen as proposed by Sofronis [9] may also be a possible approach to improve the model.

Changing parameters such as the diffusion rate and the surface hydrogen content will also have a major effect on the time to fracture initiation. Especially better knowledge of the absorbed surface hydrogen concentration level is crucial for the accuracy of the simulations.

Since the presented numerical results to a large degree is based on input from literature, they must be viewed as a first approximation showing that hydrogen influenced cohesive elements can be applied to predict HISC fracture in duplex stainless steel. The method can be improved by implementing a relation between hydrogen content and critical stress representative of the actual duplex stainless steel and by acquiring a solid basis for the choice of boundary conditions.

8 Conclusions

Hydrogen dependent cohesive elements are implemented in the crack path of ABAQUS models of U- and V-notched tensile specimen representative of 25%Cr duplex stainless steel. The effect of two different traction separation formulations as well as the influence of mesh size on the local stress field and time to fracture initiation are investigated and discussed. Gross stress levels of 485 MPa - 600 MPa and surface hydrogen concentrations of 10 ppm and 7 ppm are applied. The simulated results of time to fracture initiation are also compared to laboratory experiments.

A polynomial traction separation law and a mesh size of 0.5 μm (δ_c/Δ=0.4) gives the best resolution of the local stress field and the most stable results for both notch geometries. For mesh sizes of 5 μm and above, the linear traction separation law gives fluctuating behavior in the local stress field that may influence the fracture initiation.

References

[1] Nguyen, O., Ortiz, M. Coarse-graining and renormalization of atomistic binding relations and universal macroscopic cohesive behavior , J. of the Mechanics and Physics of Solids, 50, 2002, p. 1727-1741

[2] Hillerborg, A., Modeer ,M.and Petersson, P. E. Analysis of crack formation and crack growing in concrete by means of fracture mechanics and finite elements , Cement and Concrete Research, Vol 6**,** 1976, p. 773–782.

[3] Needleman, A. A Continuum Model for Void Nucleation by Inclusion Debonding, Journal of Applied Mechanics, Vol. 54, 1987, p. 525-531.

[4] Tvergaard, V. Effect of fiber debonding in a whisker-reinforced metal , Materials Science and Engineering A, Vol. 125 (2), 1990, p. 203-213

[5] Troiano, A.R. The role of hydrogen and other interstitials in the mechanical behavior of metals , (1959 Edward De Mille Campbell Memorial Lecture), Transactions of the ASM, Vol. 52, 1960, p. 54-80

[6] Oriani, R.A. The diffusion and trapping of hydrogen in steel, Acta Metall. 18, p. 147-157, 1970.

[7] Gerberich, W.W., Marsh, P. G, Hoehn, J.W. Hydrogen induced cracking mechanism-are there critical experiments? , Hydrogen Effects in Materials, The Minerals, Metals & Materials Society, 1996, p. 539-551

[8] Birnbaum, H.K. Sofronis, P. Hydrogen-enhanced localized plasticity-a mechanism for hydrogen-related fracture , Materials Science and Engineering, A176, 1994, p. 191-202

[9] Sofronis, P. et al Hydrogen induced shear localization of the plastic flow in metals and alloys , European Journal of Mechanics and Solids, 20, 2001, p. 857-872

[10] Delafosse, D., Magnin, T. Hydrogen induced plasticity in stress corrosion cracking of engineering systems, Engineering Fracture Mechanics 68, 2001, p. 693-729.

[11] Robertson, I.M. The effect of hydrogen on dislocation dynamics , Engineering Fracture Mechanics 68, 2001, p. 671-692

[12] Brocks, W., Cornec A., Scheider, I. Computational Aspects of Nonlinear Fracture Mechanics , in Comprehensive Structural Integrity , Vol 3 Numerical and Computational Methods, 2003, p. 127-209

[13] Scheider, I. Cohesive model for crack propagation analyses of structures with elastic-plastic material behavior – Foundations and implementation, Technical report, GKSS internal report no WMS/2000/19.

[14] Serebrinsky, S., Carter, E.A., Ortiz, M. A quantum-mechanically informed continuum model of hydrogen embrittlement , Journal of the Mechanics and Physics of Solids, 52, 2004, p. 2403-2430

[15] Liang, Y., Sofronis, P. Toward a phenomenological description of hydrogen induced decohesion at particle/matrix interfaces , Journal of the Mechanics and Physics of Solids, 51, 2003, p. 1509-1531

[16] Jiang, D.E., Carter, E.A. First principles assessment of ideal fracture energies of materials with mobile impurities implications for hydrogen embrittlement of metals , Acta Materialia 52, 2004, p. 4801-4807

[17] Hondros, E. D., Seah, M. P. The theory of Grain Boundary Segregation in Terms of Surface Adsorption Analogues , Metallurgical Transactions A, Vol 8A, 1977, p. 1363-1371
[18] ABAQUS, Version 6.5, Users' manual, ABAQUS Inc. 2004
[19] ABAQUS, Version 6.3, Example problems manual, Hibbitt, Karlsson & Sorensen Inc., 2002
[20] Johnsen, R., Nyhus, B. ,Wästberg S. , Lauvstad, G. Ø. New improved method for HISC testing of stainless steels under cathodic protection , conference paper no. 07496, published at NACE 07, Nashville, March 2007
[21] Turnbull, A., Lembach-Beylegaard, E., Hutchings, R.B. Hydrogen Transport in SAF 2205 and SAF 2507 duplex stainless steel , In A. Turnbull (Ed.), Hydrogen Transport and Cracking in Metals, The Institute of Materials, Cambridge, UK, p. 268-279
[22] Grong, Ø. Metallurgical Modelling of Welding, 2 ed. , The Institute of Materials, 1997, p. 513 -514
[23] Tvergaard, V., Hutchinson, J.W. The relation between crack growth resistance and fracture process parameters in elastic-plastic solids , Journal of Mechanics Physics and Solids, 40 (6), 1992, p. 1377-1397
[24] Taha, A., Sofronis P. A micromechanics approach to the study of hydrogen transport and embrittlement , Engineering Fracture Mechanics 68, 2001, p. 803-837
[25] Zakroczymski, T. Owzcarek, E. Electrochemical investigation of hydrogen absorption in a duplex stainless steel , Acta Materialia 50, 2002, p. 2701-2713
[26] Camacho, G.T., Ortiz, M. Computational modeling of impact damage in brittle materials , International Journal of Solids and Structures, 33, 20-22, 1996, p. 2899-2938
[27] Olden, V., Thaulow, C., Johnsen, R. Østby, E., Cohesive zone modeling of hydrogen-induced stress cracking in 25% Cr duplex stainless steel, Scripta Materialia 57, 2007, p. 615-618.
[28] Laukkanen, A., Nevasmaa, P. Constitutive Modeling of Hydrogen Cracking , Proceedings of the 6th International Conference on Life Management and Maintenance for Power Plants (Baltica IV) , Helsinki-Stockholm, 8-10 June 2004, The Finnish Maintenance Society (FMS), 2004, Vol 2. p. 419-429
[29] Katz, Y., Tymiak N., Gerberich, W.W. Nanomechanical probes as new approaches to hydrogen/deformation interaction studies , Engineering Fracture Mechanics 68, 2001, p. 619-646
[30] Barnoush, A., Vehoff H. Electrochemical nanoindentation A new approach to probe hydrogen/deformation interaction, Scripta Materialia 55, 2006, p. 195-198

Paper IV

INFLUENCE OF HYDROGEN FROM CATHODIC PROTECTION ON THE FRACTURE SUSCEPTIBILITY OF 25%CR DUPLEX STAINLESS STEEL - CONSTANT LOAD SENT TESTING AND FE-MODELLING USING HYDROGEN INFLUENCED COHESIVE ZONE ELEMENTS

Vigdis Olden[1,2] Christian Thaulow [1]

Roy Johnsen [1] Erling Østby [2] Torodd Berstad [2]

[1] NTNU, Norwegian University of Science and Technology, Faculty of Engineering Science and Technology, Department of Engineering Design and Materials, NO-7465 Trondheim, Norway
[2] Sintef, Institute of Materials and Chemistry, Department of Applied Mechanics and Corrosion, NO-7465 Trondheim, Norway

Abstract

Laboratory experiments and cohesive zone simulation of Hydrogen Induced Stress Cracking in SENT tests specimens of 25% Cr duplex stainless steel have been performed. A polynomial formulation of the traction separation law and hydrogen dependent critical stress was applied. Best agreement with the experiments was found for an initial critical stress of 2200 MPa and a critical separation of 0.005 mm. Proposed threshold stress intensity factor and lower bound net section stress is 20 MPa$\sqrt{m}$ and 480 MPa. High crack growth rates and typical hydrogen influenced fracture topography suggest large influence of the stress and strain in the fracture process zone on the hydrogen diffusion rate.

Keywords: Stainless steels; Cohesive zone modelling; Environmental cracking; Crack growth threshold: Structural assessment

1 Introduction

Hydrogen produced during cathodic corrosion protection has in recent years been found to cause cracking and failure in stainless steel subsea pipelines and fittings. Duplex stainless steel is traditionally regarded as safe due to the duplex structure of ferrite and austenite with the ductile austenite acting as a crack stopper. However, at the low corrosion protection potentials applied in the North Sea, hydrogen production is considerable. Combined with stresses during production hydrogen induced stress cracking, HISC is observed also in 25%Cr duplex stainless steel.

Diffusion in duplex stainless steel mainly takes place in the ferrite phase [1]. At subsea temperatures diffusion in the austenite phase is very slow and has an insignificant influence on the effective diffusion coefficient. However, the austenite concentration of hydrogen may be high, representing a local hydrogen “supply” if the duplex steel is brought up to a certain temperature, or under highly stressed/strained conditions. Still, the diffusion in the ferrite phase is much slower than in plain ferrite steels. This is an effect of an increased diffusion length in the ferrite due to the austenite islands and

NOMENCLATURE

bcc	body centred cubic crystallographic structure
CMOD/CTOD	crack mouth/crack tip opening displacement
CP	cathodic protection
CZM	cohesive zone modelling
fcc	face centred cubic crystallographic structure
FE	finite element
HEDE	hydrogen enhanced decohesion
HELP	hydrogen enhanced local plasticity
HISC	hydrogen induced stress cracking
SCE	saturated calomel electrode
SENT	single edge notch tensile
SIMS	secondary ion mass spectroscopy
TSL	traction separation law
C, C_E, C_L, C_{Ni}, C_T	hydrogen concentration: total, average in FE, in lattice, in nodes, in traps
D	diffusion coefficient
da/dt	crack growth rate
E	Young's modulus
E_L, E_T	activation energy for: lattice diffusion of hydrogen, hydrogen in traps
Δg_b^0	Gibbs free energy difference
J	hydrogen flux
k_{IH}	local hydrogen induced stress intensity/fracture toughness
K_I, K_{IC}	stress intensity, limit stress intensity
K_{Ith}, K_{HISC}	threshold stress intensity: general, HISC-induced
K_T	$e^{-ET/(RT)}$
N_L, N_T	number of sites for hydrogen in: lattice, traps
p	hydrostatic stress
r	cohesive fracture process zone
R	gas constant
t	time
T, T^Z	temperature, absolute temperature
V_H	partial molar volume of hydrogen in iron
α	ferrite
α'', β'	fitting constants
δ, δ_1, δ_N, δ_T,	separation of cohesive element: general, at critical stress of linear law, normal, transverse
δ_c, δ_M	critical separation in normal direction, maximum value for transverse separation
Δ	element mesh length
ε_p	equivalent plastic strain
γ	austenite
$\gamma(0)$	surface energy without hydrogen influence
Γ, Γ_c, Γ_{HISC}	cohesive energy: general, critical, HISC related
ν	Poisson's ratio
σ, σ_y, σ_{net}	stress, yield stress, net section stress
$\sigma(\delta)$, σ_N, σ_T, σ_M	cohesive stress: general, normal, transverse, maximum transverse
σ_c, $\sigma_c(0)$, $\sigma_c(\theta)$	critical cohesive stress: general, without and with hydrogen influence
θ, θ_L, θ_T	hydrogen coverage, occupancy of hydrogen in: lattice sites, trap sites

trapping at the austenite phase boundaries. The shape, size and spacing of the austenite islands will influence both diffusion length and trapping. Fine dispersed austenite islands will typically promote more tortuous diffusion paths and trapping compared to a structure consisting of coarse austenite island and larger intermediate ferrite paths" [2]. Hydrogen causes marginal reduction of the crack resistance in this phase, whereas hydrogen is prone to brittle cracking even at low hydrogen concentrations. A typical hydrogen crack in duplex stainless steel is characterized by cleavage in the {001} plane in ferrite with change of direction and stepwise zig-zag micro cracking along the <111> direction when entering the austenite [3].

The effect of local stress and strain fields on the hydrogen diffusion in front of a crack tip is a topic of special interest related to the mechanical properties and fracture toughness.

A notch or crack subjected to a plane opening stress (mode I) will, in mechanical terms, be described by a local stress and strain field ahead of the notch tip, see Fig. 1. The equivalent plastic strain ε_p is at it's highest at the notch tip and then gradually decreases with increasing distance from the notch and hydrogen will be trapped at dislocation clusters close to the notch tip. The hydrostatic stress σ reaches its maximum a short distance ahead of the crack tip and the diffusible lattice hydrogen accumulates at sites of increased stress due to the dilatation of the lattice [4]. One of the main challenges is to link the micromechanical and diffusion processes present in the fracture process zone, with the global behaviour of the component or structure.

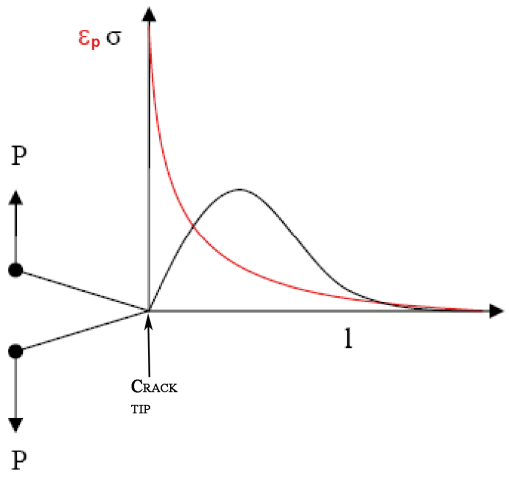

Fig. 1 Distribution of hydrostatic stress and equivalent plastic strain ε_p ahead of a crack tip loaded in mode I.

There are a wide range of proposed analytical and finite element models aiming to describe hydrogen assisted micromechanical behaviour in front of a crack tip. In general, the models are based on established elastic-plastic fracture mechanics theory. Since the hydrogen influence is active within the highly deformed area (process zone)

close to the crack tip, and hence outside the range where classical small strain theory is valid, descriptions of strain based plasticity should be included. However, no complete fracture mechanics model describing both the crack tip stress and strain within the hydrogen affected process zone exists. This is due to the fact that the mechanisms within the process zone are complex and still not very well understood.

Therefore, some assumptions regarding the micromechanical behaviour in front of the crack are required. The most cited approaches in this respect are the hydrogen enhanced decohesion (HEDE) and the hydrogen enhanced local plasticity (HELP) models.

The HEDE mechanism was first proposed by Troiano in 1960 [5] and further developed by Oriani et al. [6] and Gerberich et al. [7]. HEDE is based on the hypothesis that interstitial hydrogen lowers the cohesive strength by dilatation of the atomic lattice and with this lowers the fracture energy. This implies that hydrogen decreases the energy barrier for either grain boundary or cleavage plane decohesion. The notion is that fracture will initiate in the area of maximum hydrostatic stress some distance ahead of the crack tip. Gerberich introduced the concept of local hydrogen induced fracture toughness k_{IH} at the crack tip that scales with the yield stress, $\sigma_{y,}$ and the hydrogen induced threshold stress intensity K_{Ith}:

$$K_{I_{th}} = \frac{1}{\beta'} \exp\left\{ \frac{\left(k_{IH}\right)^2}{\alpha'' \sigma_y} \right\} \tag{1}$$

The constants β’ and α’’ are fitting parameters determined by finite element (FE) calculations and fracture mechanical tests.

HELP is characterized by atomic hydrogen that enhances the mobility of dislocations through an elastic shielding effect in preferred crystallographic planes at the crack tip causing locally reduced shear strength [8] [9]. This “local softening” results in cracking by microvoid coalescence along these planes. A HELP crack will tend to initiate from slip planes at the crack tip.

The mechanism was first introduced by Birnbaum and co-workers in 1990 [10]. Later Sofronis [8] and Delafosse & Magnin [11] quantified the stress field surrounding the hydrogen atoms causing enhanced dislocation glide. Robertson [12] reported experimental “evidence” of HELP by in situ observations of plastic deformation of thin foils in a high voltage transmission electron microscope and found an increasing amount of dislocation pile ups in AISI 310s stainless steel when introducing gaseous hydrogen at pressures ranging from 0 to 95 Torr (0 – 12,6 kPa) .

Increased hydrogen concentration at a crack tip promotes crack propagation whether it is by the HEDE or the HELP mechanism. In that sense it can be argued that the crack tip response to stress under hydrogen influence is a competition between atomic lattice decohesion and dislocation emission, between the brittle and ductile response, but always at a lower local stress level than without hydrogen influence.

In recent years the cohesive zone modelling (CZM) approach has gained interest in finite element modelling of hydrogen induced fracture. The method is appealing due to the possibility of modelling the fracture without taking the detailed micromechanism into account; it simply addresses the reduced energy threshold due to the presence of hydrogen. Fracture takes place at an interface of cohesive zone elements embedded in a finite element model; no continuum elements are damaged in a cohesive model. The cohesive elements can be pictured as two faces separated by a thickness, which is close to zero. The relative motion of the top and bottom faces in the thickness direction represents opening or closing of the interface. The relevant constitutive "material" response is a traction-separation description; an evaluation which gives the amount of energy required to create new surfaces. A traction separation law (TSL) is a function described by the cohesive stress (σ) and separation (δ). The area below the curve represents the critical separation energy, Γ_c.

Perhaps the most frequently used TSL is the polynomial function proposed for fracture in ductile materials first introduced by Needleman in 1987 [13] and further developed by Tvergaard [14]:

$$\sigma(\delta) = \frac{27}{4}\sigma_c \frac{\delta}{\delta_c}\left(1-\frac{\delta}{\delta_c}\right)^2 \quad for\ \delta \langle\ \delta_c,\ \ otherwise\ \ 0 \tag{2}$$

σ_c denotes the critical cohesive stress, δ_c the critical opening of the cohesive element. The separation energy for the polynomial description is calculated from:

$$\Gamma_c = \frac{9}{16}\sigma_c \delta_c \tag{3}$$

From the separation energy the stress intensity factor K_I can be calculated:

$$K_I = \left[\frac{E \cdot \Gamma_c}{1-\nu^2}\right]^{1/2} \tag{4}$$

E is the Young's modulus and *v* is Poisson's rate.

Hydrogen influence can be build into the TSL represented by a gradually decrease in the separation energy with increasing hydrogen content. Liang and Sofronis [15] used a polynomial TSL and also introduced a hydrogen dependant softening parameter to the material surrounding the cohesive elements in an effort to combine local softening and de-cohesion (HELP+HEDE). Serebrinsky et al. [16] used a linear TSL and an assumption of brittle decohesion based on first principles calculations of atomic plane decohesion representing a HEDE approach. Ahn, Sofronis and Dodds [17] introduced a void cell based (Gurson model based) cohesive law with hydrogen and triaxiality influence representing a ductile fracture mode in the cohesive zone as well as in the adjacent material to fulfil the HELP approach in hydrogen assisted cracking.

A mode I fracture mechanics curve of hydrogen assisted cracking is characterized by three stages of crack growth and two limit values of the stress intensity factor [16], see Fig. 2. K_{HISC} is the threshold value below which cracking will not occur or be subcritically slow. In stage I the crack initiates until stable crack growth or stage II is reached. K_{IC} is the limit value at which final unstable fracture stage III starts.

In the present paper the hydrogen distribution from transient stress and strain driven diffusion is implemented into cohesive elements defined by a polynomial TSL. FE models representing a single edge notch tension (SENT) specimen are used in diffusion, elastic plastic- and cohesive stress analyses. Time to fracture for different levels of applied stress will be calculated and compared with laboratory experiments. The comparison will also include an evaluation of the fracture topography, crack growth rate and the threshold stress intensity factor.

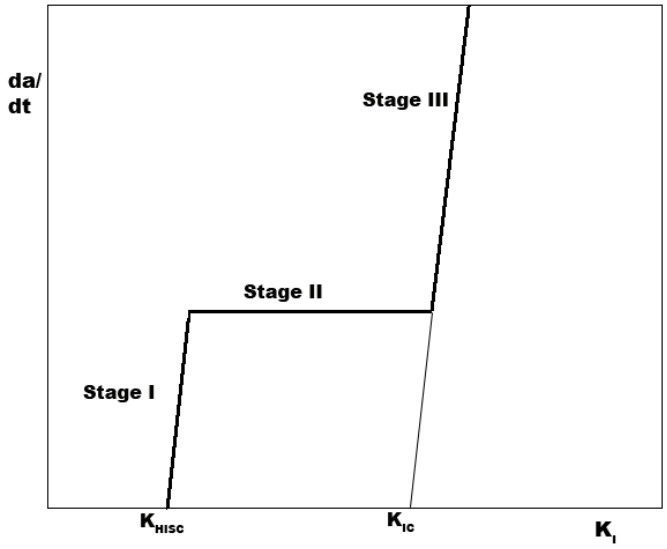

Fig. 2 Fracture mechanics curve for HISC.

2 Description of the model

The applied model consists of a three step FE simulation procedure including elastic-plastic stress analysis, diffusion analysis and finally elastic-plastic stress analysis with hydrogen influenced cohesive elements implemented in the crack path. The applied FE code is ABAQUS Standard 6.5 [18].

2.1 Elastic plastic stress analyses

The elastic plastic stress analysis is performed using the standard Mises material model in ABAQUS Standard with a material specific stress-strain curve for the duplex stainless steel. A Ramberg-Osgood power law fitting to the tensile test results gave best

fit for a hardening exponent of n=17. The resulting stress field at each applied stress level is given as an initial condition to the diffusion analysis.

2.2 Diffusion analysis

Stress driven diffusion given in ABAQUS is represented by a modified Ficks' law with respect to the hydrostatic stress, p:

$$\frac{\partial C}{\partial t} = D\nabla^2 C + D\cdot\frac{V_H}{R\cdot\left(T-T^Z\right)}\nabla C\cdot\nabla p + D\cdot\frac{V_H}{R\cdot\left(T-T^Z\right)}C\nabla^2 p \tag{5}$$

Where C is the hydrogen concentration, D is the diffusion coefficient, $\overline{V}_H$ is the partial molar volume of hydrogen in iron-based alloys, R the gas constant (8.3142 J/mol K), T the actual and T^Z the absolute zero temperature, see ABAQUS manuals or earlier work [19] for details.

The treatment of crack tip hydrogen concentration has traditionally been based on Eq. 5 representing an accumulation of hydrogen in areas of high hydrostatic stress. Sofronis and McMeeking [4] and later Krom and Bakker [20] described diffusion models reflecting a competition between the hydrostatic stress field and the highly strained area at the notch tip. The models are based on the principle by Oriani [6] that populations of hydrogen in trapping sites and in lattice always are in equilibrium, as described by:

$$\frac{\theta_T}{1-\theta_T} = \frac{\theta_L}{1-\theta_L}K_T \tag{6}$$

θ_L denotes the occupancy of hydrogen on interstitial lattice sites, θ_T the occupancy of hydrogen on trapping sites and $K_T = e^{\frac{-E_T}{RT}}$. The concentration in lattice C_L and traps C_T can be written

$$C_L = \theta_L N_L \tag{7}$$

$$C_T = \theta_T N_T \tag{8}$$

C_L is the diffusible hydrogen concentration calculated by Eq. 5, while C_T is the additional hydrogen concentration in reversible traps. N_L and N_T is the number of sites for hydrogen in the lattice and at reversible traps respectively. From Eq. 7 and 8 and assuming $\theta_L << \theta_T$, the equilibrium concentration of hydrogen can be written:

$$C_T = \frac{N_T}{1+\frac{1}{K_T\theta_L}} \tag{9}$$

Sofronis and McMeeking [4] proposed a relation between N_T and plastic strain ε_p based on experimental data for iron from Kumnick and Johnson [21]:

$$\log N_T = 23.26 - 2.33e^{-5.5\varepsilon_p} \tag{10}$$

Regarding the lattice sites N_T a constant, the partial derivative of the hydrogen concentration in traps as a function of time becomes:

$$\frac{\partial C_T}{\partial t} = \frac{\partial C_T}{\partial C_L} \cdot \frac{\partial C_L}{\partial t} + \frac{\partial C_T}{\partial N_T} \cdot \frac{dN_T}{d\varepsilon_p} \cdot \frac{\partial \varepsilon_p}{\partial t} \tag{11}$$

Representing $\frac{\partial C_T}{\partial C_L}$ with $\frac{C_T(1-\theta_T)}{C_L}$, $\frac{\partial C_T}{\partial N_T}$ with θ_T and implementing it into Eq. 11, Fick's law including both the effect of hydrostatic pressure and trapping becomes:

$$\frac{C_L + C_T(1-\theta_T)}{C_L} \frac{\partial C_L}{\partial t} = \nabla \cdot (D_L \nabla C_L) - \nabla \cdot \left(\frac{D_L C_L V_H}{R(T - T^Z)} \nabla p \right) - \theta_T \frac{dN_T}{d\varepsilon_p} \frac{\partial \varepsilon_p}{\partial t} \tag{12}$$

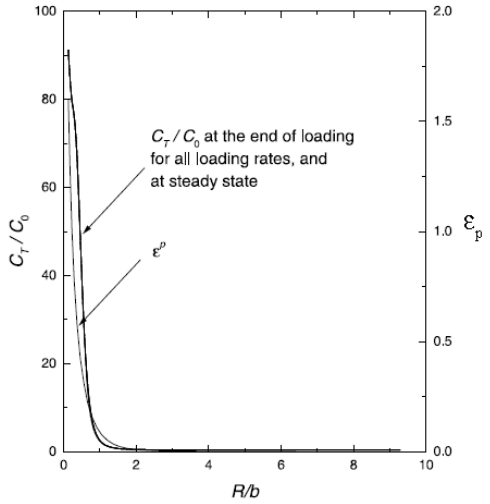

Fig. 3 Normalized hydrogen concentration (C_T/C_0)in trapping sites and equivalent plastic strain as a function of the normalized distance (R/b) from a blunted crack tip in steel as reported by Taha & Sofronis [22].

In the present work an approach based on the work by Taha & Sofronis [22] is proposed. FE calculations for high and low strength steel based on Eq. 12 revealed that the shape of the plastic strain distribution and of the hydrogen concentration in traps in front of a crack tip when exposed to surface hydrogen were almost similar, Fig. 3. A marginal influence of the strain rate due to the easy access of hydrogen from the surface was observed. Based on the reported data in [22] we propose a linear correlation between the trapped hydrogen concentration and the plastic strain:

$$C_T = (49.0 \cdot \varepsilon_p + 0.1) \cdot C_L \tag{13}$$

The relation implies that when the plastic strain is larger than ~ 2%, trapping will yield the dominating influence on the hydrogen concentration. The correlation is implemented in a user defined cohesive element subroutine. By reading the plastic strain in the neighbouring continuum elements C_T is calculated and added to C_L for each increment and node before giving the total hydrogen concentration C to the TSL.

2.3 Hydrogen influenced traction separation law

A polynomial TSL is chosen based on previous research suggesting better stability in the simulations compared to a bilinear TSL [19]. A relation for the coupling between hydrogen coverage, θ, and the local critical hydrogen dependent cohesive stress, σ_c (θ) for bcc Fe proposed by Serebrinsky et al. [16] is applied:

$$\frac{\sigma_c(\theta)}{\sigma_c(0)} = 1 - 1.0467\theta + 0.1687\theta^2 \tag{14}$$

where $\sigma_c(0)$ is the local critical cohesive stress without hydrogen influence. The relation is based on a fitting of surface energy values reported by Jiang and Carter [23], where the surface energy for α-Fe without hydrogen influence, γ (0), is 2.43 J/m^2. A plot of the cohesive law with hydrogen influence according to Eq. 14 is shown in Fig. 4.

Hydrogen coverage is defined as a function of the hydrogen concentration and the Gibbs free energy difference Δg_b^0 between the interface and the surrounding material as expressed in the Langmuir-McLean isotherm [24]:

$$\theta = \frac{C}{C + \exp(-\Delta g_b^0 / RT)} \tag{15}$$

Crack initiation is defined as zero cohesive stress and critical opening (δ_c) in the first cohesive element.

2.4 Implementation of hydrogen assisted cohesive elements

Two dimensional user defined cohesive elements are implemented in ABAQUS Standard using a FORTRAN sub-routine initially developed by Scheider [25].

To add this strain influence on the hydrogen concentration the effective plastic strain in the nearest element to the cohesive elements need to be found and the information transferred to the cohesive elements. To find the strain in certain points the user subroutine UVARM in ABAQUS is used to gather the effective plastic strain for elements where the material definition includes specification of user-defined output variables. An array containing the coordinates and the effective plastic strain for the integration point is created and communicated to the cohesive elements as a FORTRAN Common block. The effective plastic strain ε_p in the nearest integration points to the surrounding element is transferred to the cohesive element. An extra term

in the hydrogen concentration is defined as $C = C_L + C_T$ where C_L is the hydrogen concentration calculated from the diffusion analysis and C_T is the addition to the hydrogen concentration due to plasticity calculated by Eq. 13.

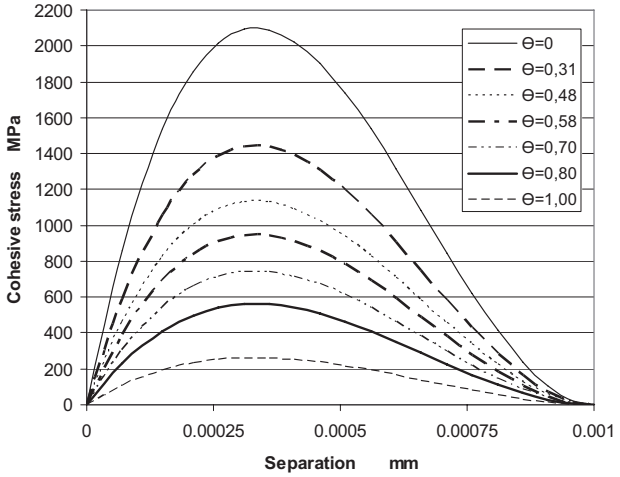

Fig. 4 Hydrogen influenced cohesive law for σ_c (0) = 3.7·σ_y.

In the cohesive stress analysis the hydrogen concentration must be given for the nodes connected to the cohesive elements as part of the input to the finite element analysis. Based on the hydrogen concentration for the four nodes C_{Ni} connected to an element a mean concentration C_E for the cohesive element can be calculated as

$$C_E = \frac{1}{4}\sum_{i=1}^{4} C_{Ni} \tag{16}$$

The hydrogen coverage in the element is then calculated by Eq. 15 (C is replaced with C_E) and the critical cohesive stress in pure tension for the element is calculated by Eq. 14. Based on the normal separation δ_N in the cohesive element, which is the difference of the displacement of the adjacent continuum elements, a normal stress in the cohesive element is calculated by Eq. 2. When the normal separation δ_N has reached the value of δ_c, the element looses the ability to carry load in both the normal and the transverse direction. In the current work the stresses in the normal and transverse direction for the cohesive element are calculated independent of each other. The shear traction is calculated from the tangential separation and given as a linear law:

$$\sigma_T = \sigma_M \frac{\delta_T}{\delta_M} \tag{17}$$

where δ_T is the transverse separation, σ_M and δ_M are input parameters for the actual TSL. The shear traction is independent of the hydrogen concentration and in the current work no unloading in the shear direction of the cohesive element are implemented.

3 Experiments

3.1 Material

The material at hand is cut from a forged 25% Cr duplex stainless steel pipe with an outer diameter of 273 mm and a wall thickness of 21.44 mm. Chemical composition in weight % is C: 0.016, Si: 0.23, Mn: 0.79, P: 0.021, S: 0.001, Cr: 25.0, Ni: 6.98, Mo: 3.82, Cu: 0.32. Ferrite content according to ASTM E562 is 46% and the average austenite spacing is 13μm. A representative micrograph of the microstructure in the longitudinal direction is shown in Fig. 5. Yield ($Re_{0.5\%}$) and ultimate tensile strength are 600 MPa and 800 MPa.

3.2 Sample geometry and test conditions

Rectangular 9 mm x12 mm samples were machined parallel with the length axis of the pipe. A 2 mm deep notch was prepared by a combination of spark erosion (1 mm) and fatigue cracking (1mm). Sample length between the grips was 60 mm. A picture of a sample and a drawing of the notch geometry including clip gauge grips are shown in Fig. 6.

A designed test rig for constant load testing under CP conditions was used for the experiment. The test rig has four parallel axes, each with separate load control. The samples were submerged in circulating artificial sea water at 4°C with a cathodic protection potential of -1050 mV_{SCE}. The applied stress level ranged from 450 – 550 MPa representing net section stresses between 540 and 660 MPa or 90 – 110% of the materials yield strength. Fig. 7 shows a picture of samples mounted in the test rig. Net section stress and the crack mouth opening displacement (CMOD) were recorded until global fracture occurred.

Fig. 8 show plots of the recorded data for all fractured specimen. A sharp rise in CMOD implies the onset of final unstable fracture (stage III crack growth, see Fig. 2). Duration of stable crack growth (stage II) is retrieved by using the linear part of the CMOD curve. Cut off is marked by a long dashed line. Two samples without fracture loaded at lower stresses were unloaded during stage II crack growth and taken out of the rig.

Initial CMOD was also calculated based on a 3D elastic plastic simulation of the samples during uploading without hydrogen charging and compared with measured initial CMOD, see Fig. 9. Reasonably good fit between measured and simulated values was obtained.

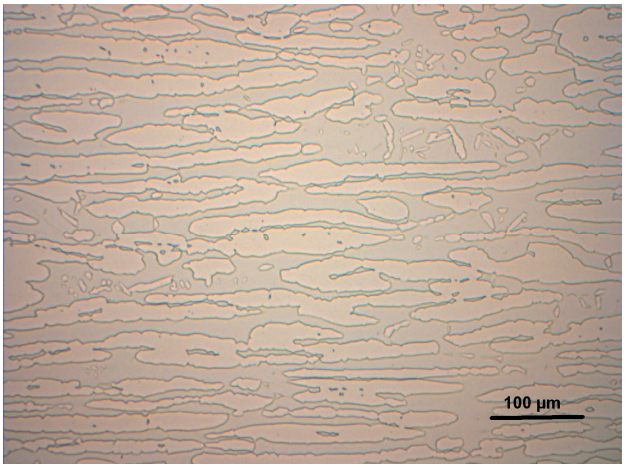

Fig. 5 Microstructure of the 25% Cr duplex stainless steel; austenite is light.

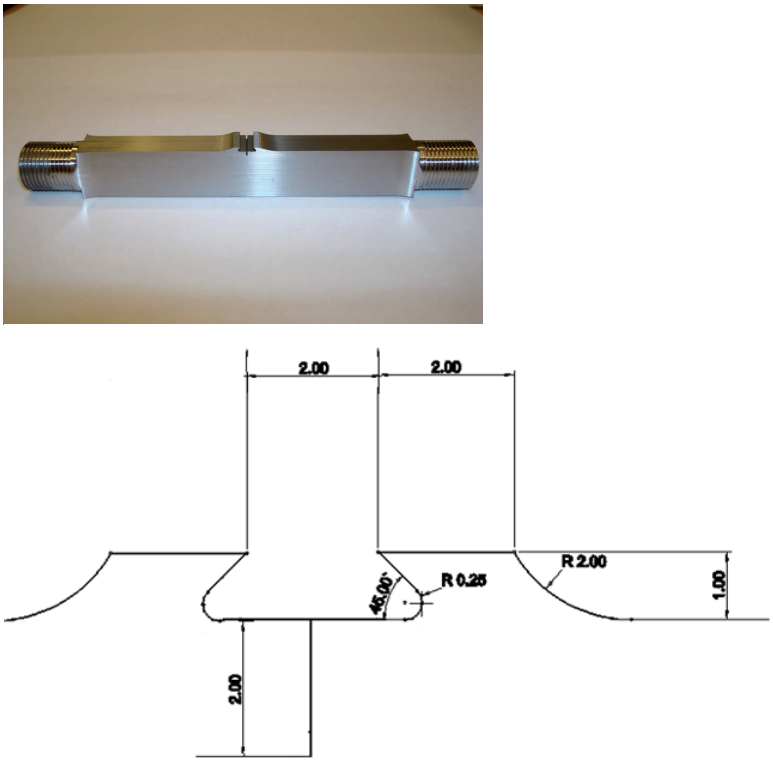

Fig. 6 Test sample and a close up of the notch area with clip gauge grips (dimensions in mm).

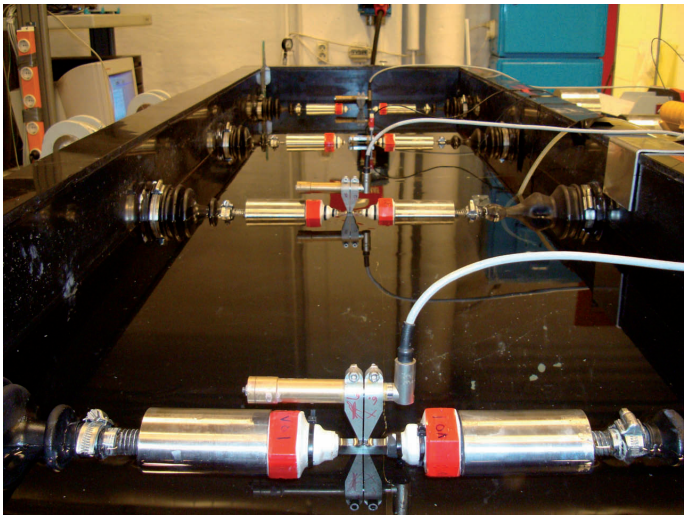

Fig. 7 Test rig for constant load testing with cathodic protection. Samples were submerged in slowly circulating artificial sea water at 4°C. CP potential was -1050 mV_{SCE}.

3.3 Stress and hydrogen concentration analyses

Due to the 2D nature of the implemented cohesive elements a 2D model of the samples was applied for the further analyses. The model has a total number of 6553 elements and 6797 nodes and the continuum elements are a four node bilinear plain strain type. Due to symmetry only half of the sample is modelled. The element size along the symmetry axis, which also is the crack path, is 10 µm. A sharp notch represents the fatigue crack tip. Fig. 10 gives an overview and a detail view of the elements in the notch tip area.

The net section stress is within the same range as the laboratory experiments between 480MPa and 650 MPa. The diffusion coefficient is $3.7 \cdot 10^{-12}$ m^2/s based on data from diffusion measurements on duplex stainless steel reported by Zackroczymski and Owczarek [1]. Since their experiments were performed at 25°C a temperature correction representing the difference between 25°C and 4°C using the Arrhenius equation $D = D_0 \cdot \exp(-E_L/RT)$ was performed. The chosen value of D is high compared to values reported by Turnbull et al [2], which is close to the diffusion rate of austenite steel; in the area of 10^{-16} m^2/s. Turnbull et al performed their experiments on samples with the microstructure parallel to the hydrogen exposed surface which increases the diffusion path. In the SENT specimens hydrogen will have easy access to ferrite since the microstructure is perpendicular to the crack surface, which was also the case in Zackroczymski's and Owczarek's measurements. The lattice solubility of hydrogen is taken as 0.033 $ppm \cdot mm \cdot N^{-1/2}$. This value originates from for 2.25Cr-1Mo steel [26] based on the assumption that initial cracking occurs in the ferrite phase. The applied subsurface hydrogen concentration is 1ppm. This is the same value as applied by Serebrinsky et al. [16] corresponding to a 3% NaCl solution.

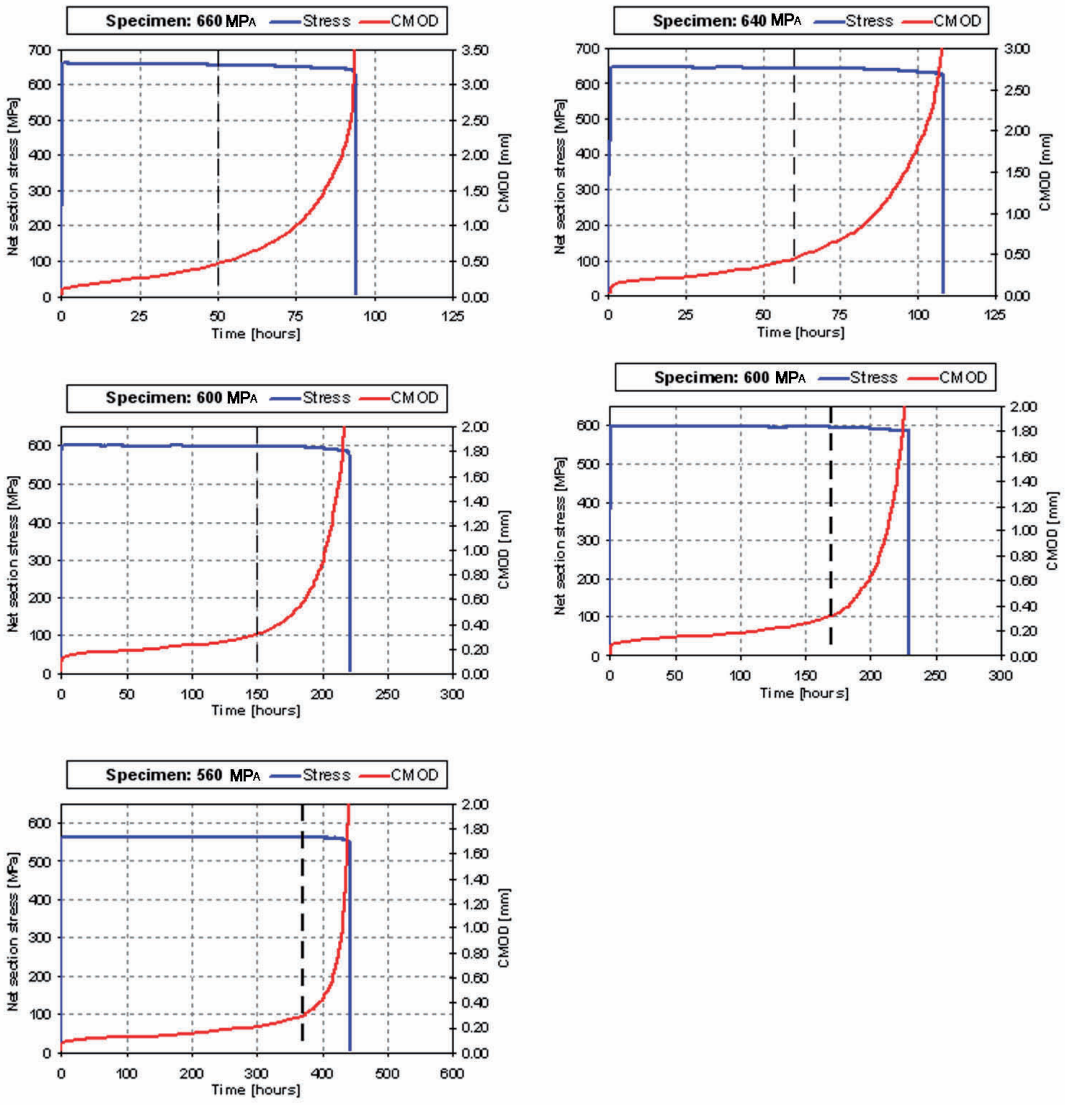

Fig. 8 Log data of net section stress and CMOD for fractured SENT specimens. Long dashed line denotes cut off at initiation of stage III crack growth.

Normal stress and equivalent plastic strain in front of the crack tip for three levels of applied stress from the elastic plastic stress analyses are presented in Fig. 11. Note the difference in rank regarding the global and local stress level. Whereas the global net section stress is higher for the larger applied stresses the stress peaks for applied loads of 540 MPa and 500 MPa are lower and located further from the crack tip than for an

applied load of 400 MPa due to loss of constraint [27]. This is accompanied by higher levels of plastic strain for the larger applied loads. The plastic strain levels at the surface are all well above the 2 % value which is needed for trapping dominance according to Eq.13.

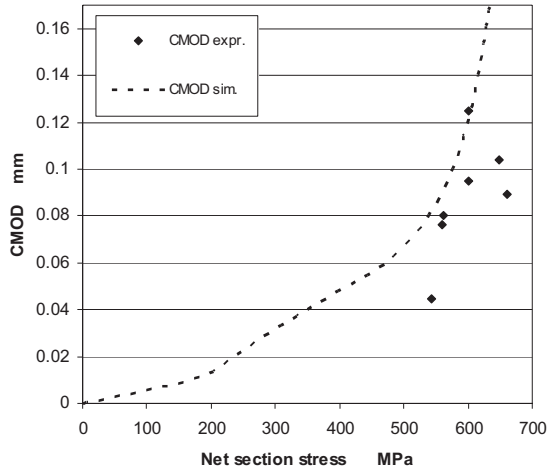

Fig. 9 Simulated CMOD plotted with measured initial CMOD from the laboratory experiments.

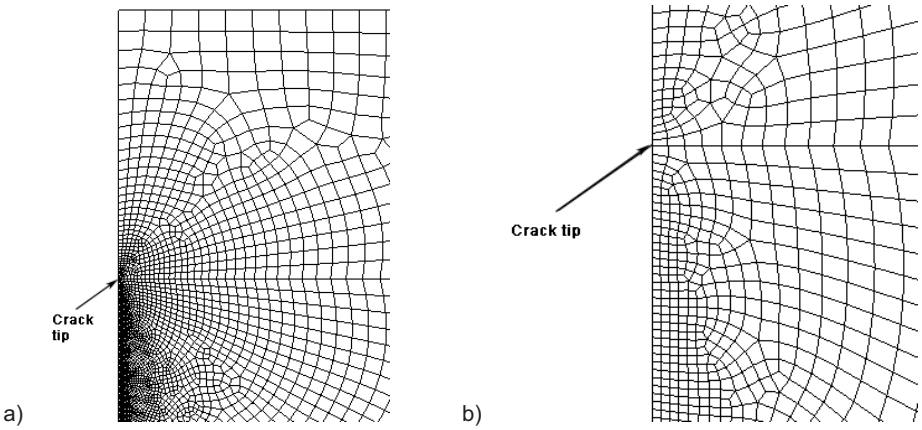

Fig. 10 FE model a) overview including the 2 mm notch b) close up of the crack tip area.

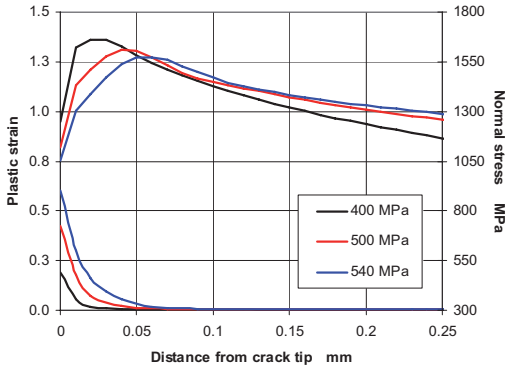

Fig. 11 Normal net section stress and equivalent plastic strain in front of the crack tip for three levels of applied stress.

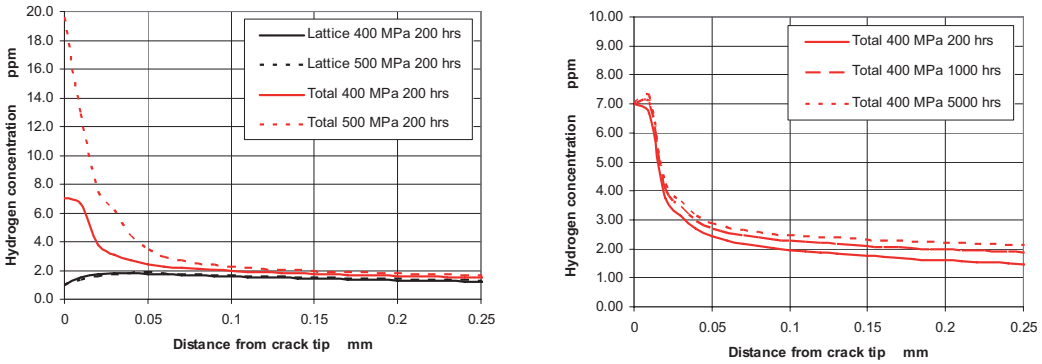

a) b)

Fig. 12 Hydrogen concentration in front of the crack tip for two levels of applied stress a) Lattice and total H concentration after 200 hours for the applied stresses 400 MPa and 500 MPa b) Total H concentration for an applied stress of 400 MPa after 200, 1000 and 5000 hours.

According to Eq. 13 the level of plastic strain has a strong influence on the distribution of trapped hydrogen. This is clearly illustrated in Fig. 12 where the lattice hydrogen (based on Eq. 5) is plotted together with the total concentration C including the effect of plastic strain (Eq. 13). C_L reaches a maximum at the local stress peak whereas C reaches much higher levels close to the surface due to the plastic strain. Maximum C is about three times higher for an applied stress of 500 MPa (max ε_p= 42%) compared to 400 MPa (max ε_p=19%), see Fig. 12. Maximum hydrogen concentration of 30 ppm is obtained for an applied stress of 540 MPa (max ε_p= 60%). The lattice concentration changes marginally with the stress level; a maximum concentration of about 2 ppm is reached at the location of the stress peak for all stress levels, see Fig. 12 a. This is in line with earlier observations for U- and V- notch samples [19]. Accordingly the hydrogen distribution near the crack tip also changes little by time. For an applied

stress of 400 MPa a weak build up at the local stress field can be observed about 0.01 mm in front of the crack tip. Further into the material the hydrogen concentration increases with time according to the lattice diffusion rate, see Fig. 12 b. In the following cohesive analysis the transient total hydrogen concentration will be used as input to the hydrogen influenced TSL. This implies that trapped hydrogen dominates the contribution to the reduction of the critical stress. Whether this is actually the case in HISC is an unanswered question, and will remain a topic for further investigation.

3.4 Comparison with laboratory experiments

In the cohesive FE analysis best fit to the laboratory results was obtained for the cohesive parameters: $\sigma_c(0)$= 2200 MPa (~3.7 times the yield strength) and δ_c=0.005 mm, see continuous line in Fig. 13. Red symbols represent the laboratory results; crosses denote samples unloaded before fracture. The simulated results indicate that fracture will not occur below a net section stress level of 480 MPa (80% of the yield strength). According to Eq. 3 and 4 the applied cohesive parameters yields a threshold stress intensity factor without the effect of hydrogen K_0 = 117 MPa$\sqrt{m}$. Maximum hydrogen concentration at a net section stress of 480 MPa is 7 ppm representing a hydrogen coverage of θ= 0.76, which according to Eq. 14 gives a critical hydrogen influenced cohesive stress of 660 MPa and hence a K_{HISC} value of 20 MPa$\sqrt{m}$. Calculating the corresponding crack tip opening displacement (CTOD) by the established relation $4/\pi\ [K_I^2/(\sigma_y E)]$ yields 0.0042 mm.

For comparison a dotted line shows the best fit without including the effect of trapping. Here the time to fracture is less sensitive to the stress level and a lower bound is not obtained within the applied stress range. An increase in subsurface hydrogen concentration to 1.5 ppm was necessary because 1 ppm H did not lower the critical hydrogen induced cohesive stress below the maximum crack tip stress and hence no initiation of fracture occurred.

Cohesive stress and separation of the cohesive elements at initiation of fracture for applied stresses of 416 MPa and 500 MPa and trapping is plotted in Fig. 14. Note that "softening" due to hydrogen has caused a reduction of the maximum stress of about 20% as well as a shift of the maximum stress peak about 0.20 mm into the material compared to the results in Fig. 11. The total cohesive fracture process zone R is roughly 0.25 mm and represents the cohesive elements that have passed the maximum stress described by the TSL, see Fig. 4. The ratio between the fracture process zone and the element size r/Δ gives an indication of how well the mesh resolves the stresses and strains. In our model r/Δ = 25, which according to Tvergaard & Hutcinson [29] and Camancho & Ortiz [30] gives a good resolution of the local stress and strain field.

As previously reported for U- and V- notch samples of the same material [19] the simulated fracture initiates in the surface element and not at the location of the maximum stress, which is consistent with the high hydrogen content near the surface. Also in the simulations without influence of trapped hydrogen fracture occurred in the surface element even if the H concentration is much lower. This is caused by a combined situation where the hydrogen concentration close to the surface is high enough to reduce σ_c below the normal stress and the stress peak being pushed into the

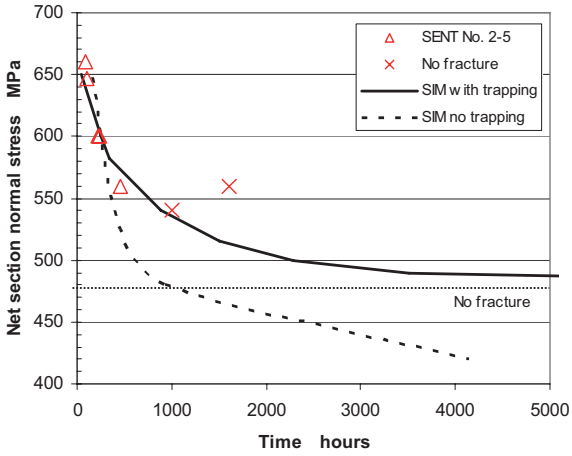

Fig. 13 SENT test results compared with cohesive FE simulation with and without the effect of trapping.

material by the hydrogen "softened" cohesive elements. In a situation with bulk hydrogen and no trapping representing precharged specimens, earlier work have shown that fracture occurs *at* the stress peak [28]. If this still will be the case when trapping is considered is yet to be investigated.

The fracture surfaces were investigated in a Scanning Electron Microscope (SEM). Fig. 15 a) presents an overview of the crack propagation area and Fig 15 b) a close up of the location of crack initiation for the 647 MPa specimen. The dominating fracture mode in the stable crack propagation area is trans-granular cleavage in ferrite with ductile tearing of austenite, which is typical HISC fracture topography in duplex stainless steel; see Fig. 16 a). Secondary cracks and branching lined up with intervals perpendicular to the direction of the crack indicates stepwise cracking, see Fig. 16 b). Some embrittled areas in austenite showing zig-zag cleavage fracture were also observed.

The lengths of the propagating (stage II) cracks were measured with an optical microscope; also samples without final fracture were included. Hydrogen induced crack lengths, measured at the mid section of the samples, ranged from 0.8 mm to 3.9 mm. Fig. 17 a) – b) show crack profiles of a fractured and not fractured specimen with identification of the different regions of the crack. By dividing the crack length with the stage II crack propagation time extracted from the CMOD plots in Fig. 8, crack propagation rates da/dt for the tested specimens were obtained. There is a linear increasing crack rate with the increasing stress; ranging from ~$2.2 \cdot 10^{-10}$ m/s to $1.5 \cdot 10^{-8}$ m/s; see logarithmic plot in Fig. 18.

Fig. 19 shows crack branching at the end of a stage-II crack for a fractured specimen. Close up of the marked area shows how the crack propagates along ferrite paths arrests at or changes direction when entering an austenite phase before propagating further in ferrite.

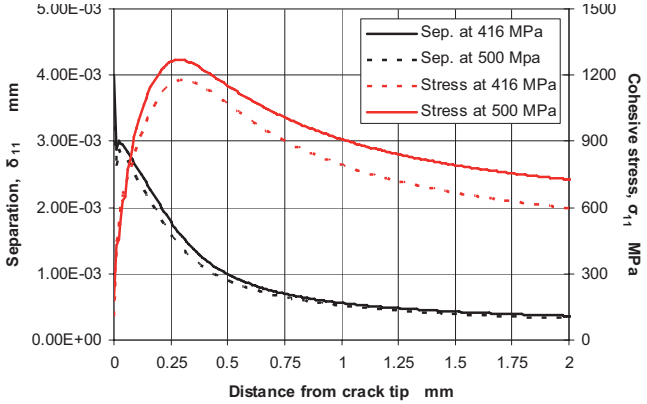

Fig. 14 Cohesive stress and separation in the cohesive elements plotted at the time of collapse of the first cohesive element.

a)

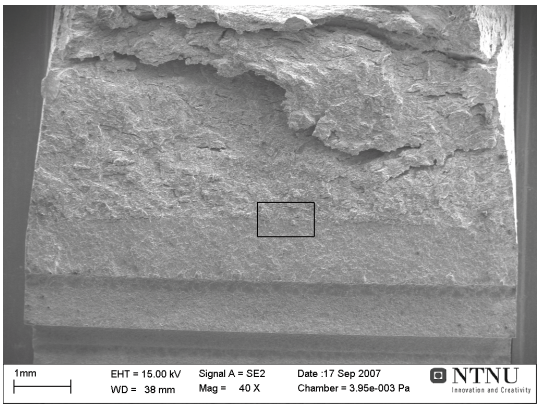

b)

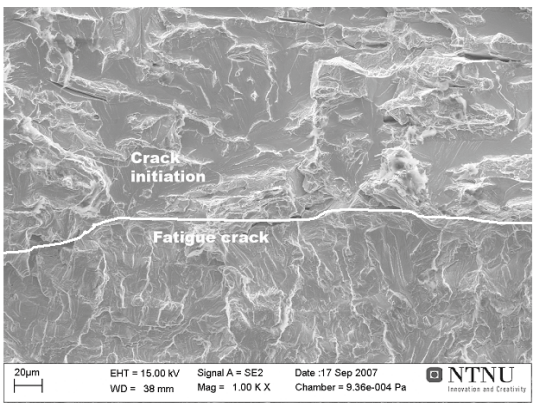

Fig. 15 SEM pictures of the crack propagation area of the σ_{net}= 647 MPa sample. a) Sample overview. Square indicates HISC fracture initiation area. b) HISC fracture initiation area. The fatigue crack front is denoted with white line.

a)

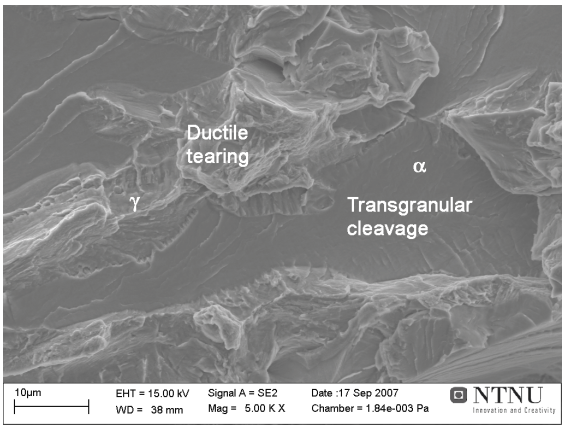

b)

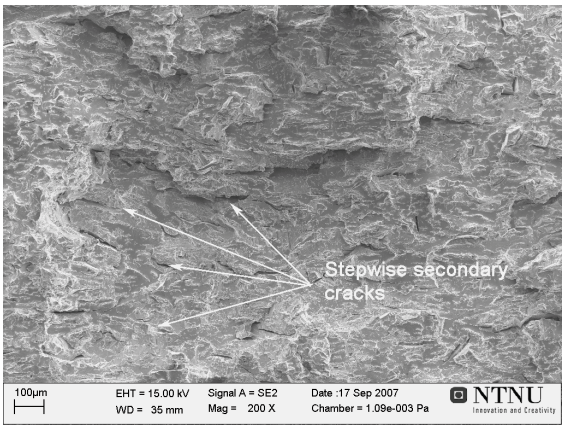

Fig. 16 Typical fracture modes a) Transgranular cleavage in ferrite, α and ductile tearing in austenite, γ. b) Secondary cracks perpendicular to the direction of the propagating crack.

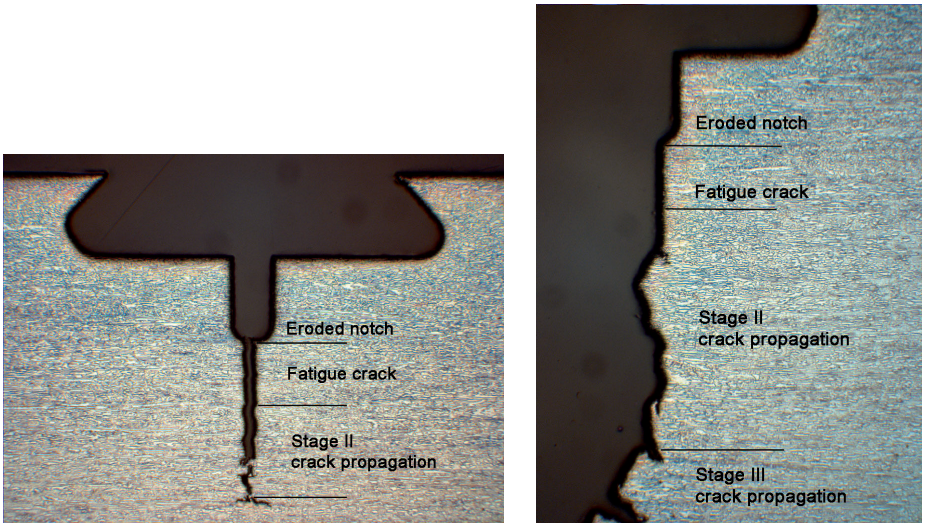

a) b)

Fig. 17 Crack profiles a) Not fractured sample, σ_{net}=560 MPa, magnification ~15x b) Fractured sample, σ_{net}=600 MPa, magnification ~10x.

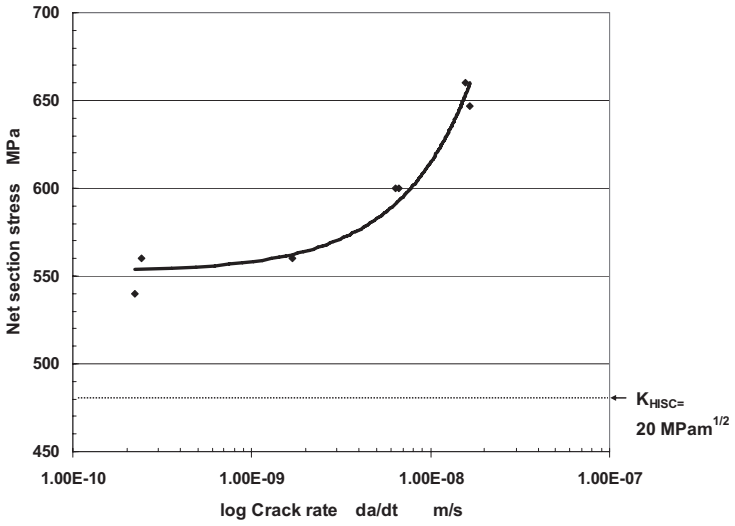

Fig. 18 Crack propagation rate as a function of net section stress.

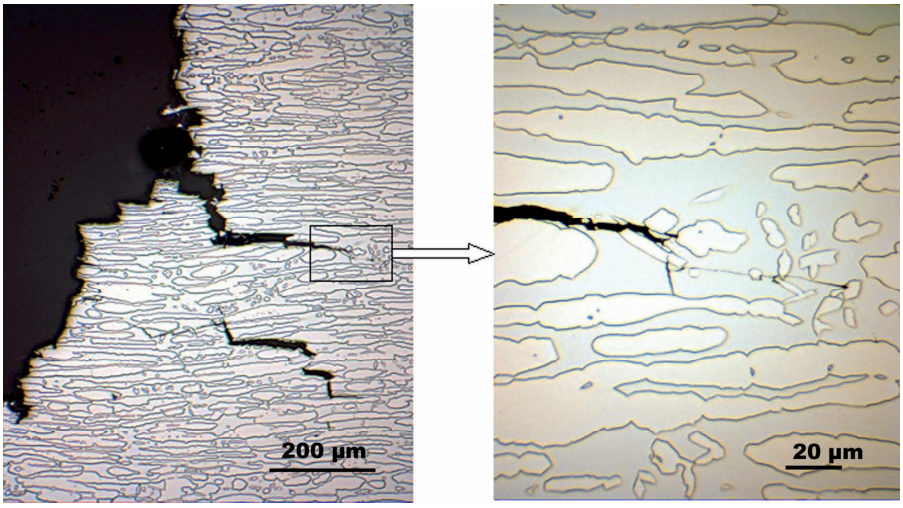

Fig. 19 Details of a branched part of a HISC crack at the end of Stage II crack propagation.

4 Discussion

The applied cohesive stress of $\sigma_c(0)= 3.7\cdot\sigma_y$ is in line with suggestions by Tvergaard and Huchinson [29] using $4\cdot\sigma_y$ as the critical cohesive stress in polynomial TSL without hydrogen influence. Later Serebrinsky et al. [16] applied the same critical stress in linear hydrogen influenced TSL's and found good agreement with fracture threshold stresses for high strength steel in aqueous solutions.

The suggested stress intensity for the 25%Cr duplex stainless steel below which cracking will not occur is K_{HISC} = 20 MPa√m at a net section stress of 480 MPa. This corresponds to $CTOD_{HISC}$ of 0.0042 mm. No relevant comparable data for duplex stainless steel is found in literature. Similar testing have however been reported for a large range of high strength steels. Lee and Gangloff [31] reported a threshold stress value of 9.3 MPa√m in high strength steel (AerMet^{TM} 100) based on SENT testing in 3.5%NaCl at a cathodic potential of -1100 mV_{SCE}. This is martensitic steel with yield strength above 1700 MPa, which implies higher sensitivity to HISC than in duplex steels. Serebrinsky et al [15] found threshold values in the range 25-75 MPa√m for AISI 4340 steel with yield strengths of 1600 to 1000 MPa using cohesive zone modelling and Eq. 14-15 for description of the hydrogen influence. They did not however include the effect of trapping.

For hydrogen assisted stepwise cracking there is a close relationship between the hydrogen diffusion rate and the crack propagation rate. Between each crack step hydrogen must be given time do diffuse into the process zone and build up to a critical level. Crack rates in these experiments vary from about $2.2\cdot10^{-10}$ m/s for the lowest stress up to $1.5\cdot10^{-8}$ m/s for the highest stresses which are clearly higher than the lattice diffusion rate of $3.7\cdot10^{-12}$ m^2/s applied in the diffusion analyses. The fracture

topography in the stable crack growth area of the fractured specimens revealed stepwise cracking and transgranular cleavage in ferrite, features which indicate the presence of hydrogen. This suggests that stresses and strains at the crack tip takes active part in driving the hydrogen into the material at a much higher rate than the pure lattice diffusion rate. The observation is supported by Oltra & Boillot [3] who by using SIMS proved an accumulation of hydrogen in austenite following the crack path in duplex stainless steel under hydrogen gas charging conditions.

Lee and Gangloff [31] suggest a subcritical crack growth rate of $2.5 \cdot 10^{-10}$ m/s which is in fact very similar to the slowest crack growth rate in the present study. However, since the lattice diffusion rate of hydrogen is slower in duplex stainless steel than in martensitic steel the subcritical crack growth will also presumably be slower. SENT testing at lower net section stresses can be performed to verify this. This would also help verifying the suggested net section lower bound of 480 MPa from the cohesive analyses.

The transgranular cleavage fracture in ferrite in the stable crack growth area strongly suggests hydrogen uptake, since duplex stainless steel tend to fracture in a completely ductile fashion without the presence of hydrogen. The presence of embrittled areas in austenite is clear evidence that hydrogen also has diffused into this phase, see Fig. 20. This observation is important because it implies that the hydrogen not only enters the ferrite phase, but also causes embrittlement of the austenite and hence reduces the crack arrest properties of the austenite phase. The observed stepwise cleavage fracture in austenite bares close resemblance to the fracture crystallography in AISI 316 stainless steel hydrogen charged in boiling $MgCl_2$ at free potential described by Delafosse & Magnin [11]. The average local crack plane is {110} with steps in the <111> direction, see Fig. 18. This fracture pattern is commonly observed in hydrogen charged face centred cubic single and poly-crystals.

Embrittled austenite is not a dominating feature of the investigated fracture surface in this study. However, considering the very low lattice diffusion rate of hydrogen in austenite in unstressed state it can be argued that the mere presence of brittle cleavage in austenite at the present crack rates indicates a strong influence of stresses and strains on the hydrogen diffusion in a crack tip zone.

The investigation of the fracture surface and the propagating cracks has also revealed that the cohesive zone simulations do not directly reproduce the actual crack. The length of the cohesive zone at failure is smaller than the measured crack lengths. The small “microcrack” as represented by separation of a 10 μm cohesive element is not sufficient for a real failure to occur. Therefore it must be emphasized that the suggested cohesive parameters are not meant to reproduce the micro-mechanisms but rather to be a representation of the onset of failure at the different stress levels and environment. Reading off the total H -concentration as a function of the plastic strain in the neighbour elements of the cohesive zone into the TSL represents a simplified procedure of taking the effect of changing plastic strain conditions during crack propagation into account. To be able to correctly reproduce stepwise HISC cracking in the cohesive elements an iterative coupling between both the stress and strain field

surrounding the cohesive zone and the diffusion analyses as performed by Ahn et al. [17] is required. However, it can be argued that if the main hydrogen source is at the surface, also including the crack tip, and the plastic strain values at the crack tip are above ~ 2% (as suggested by Taha and Sofronis [22]) the presented method is applicable.

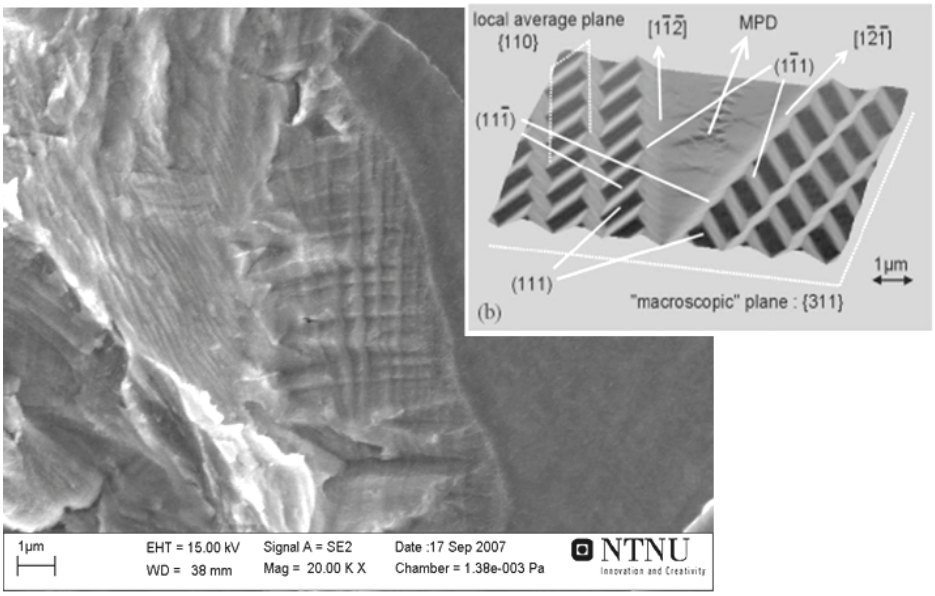

Fig. 20 Cleavage fracture in austenite phase of fractured sample compared to typical feature of zig-zag cleavage crack pattern of hydrogen charged AISI 316 stainless steel reported by Delafosse & Magnin [11].

Independent of whether the governing micro-mechanisms are HEDE, HELP or a combination the CZM will capture the onset of HISC fracture. There are however several aspects that can be addressed for better accuracy. The diffusion coefficient and the subsurface hydrogen content of duplex stainless steels published in literature varies significantly and should be established for the relevant conditions. The applied relation for trapping of hydrogen due to plastic strain is based on work on iron and may not be fully representative for duplex steel. Also an established relation for hydrogen induced critical stress in the actual ferrite phase of the duplex steel would be preferable. Last but not least, better knowledge of the role of trapped and lattice hydrogen in the HISC crack initiation and propagation process is needed. Atomistic simulations may be a suitable method of retrieving first principle relations like this.

5 Conclusions

Constant load SENT testing at applied stresses of 450-550 MPa of not precharged 25%Cr duplex stainless steel in 3.5% NaCl at 4°C and a corrosion protection potential of -1050 mV_{SCE} revealed hydrogen induced stress cracking prior to final fracture.

The stable crack growth rates ranged from $2.2 \cdot 10^{-10}$ m/s to $1.5 \cdot 10^{-8}$ m/s which is clearly higher than lattice diffusion rates for 25% Cr duplex stainless steel given in literature. This indicates that stresses and strains in the crack process zone have a strong influence on the diffusion rate.

For prediction of crack initiation a finite element simulation procedure with hydrogen dependant cohesive elements in the crack path was carried out. Best fit to experimental results was obtained for an initial critical cohesive stress of 2200 MPa ($\sigma_c=3.7 \cdot \sigma_y$) and a separation ($\delta_C$) of 0.005 mm. The simulations indicate a lower bound applied net section stress of 480 MPa giving a threshold stress intensity factor (K_{HISC}) of 20 MPa$\sqrt{m}$.

Crack initiation represented by collapse of the first cohesive element occurred in the element closest to the crack tip surface and not at the local crack tip stress peak. This is due to the surface hydrogen source that lowers the critical stress at the surface.

In the simulations both lattice and trapped hydrogen contributes to a lowering of the stress necessary for the onset of fracture. A direct relation between plastic strain and trapped hydrogen concentration based on work by Taha and Sofronis [22] is proposed and implemented in the cohesive elements. The relation implies that compared to stress driven lattice diffusion plastic strain is the main contributor to the simulated hydrogen concentration and crack initiation in the fracture process zone.

Acnowledgements

The authors want to express their thanks to Sintef for giving access to laboratory test equipment and especially Mrs. Lisbeth R. Støen for carefully carrying out the SENT testing and Dr. Odd Magne Akselsen for valuable discussions on the metallurgical topics. The laboratory work is partly sponsored by the NTNU project PETROMAKS.

References

[1] Zakroczymski, T., Owzcarek, E., Electrochemical investigation of hydrogen absorption in a duplex stainless steel , Acta Materialia, 50, 2002, pp 2701-2713

[2] Turnbull, A. , Lembach-Beylegaard, E., Hutchings, R.B., Hydrogen Transport in SAF 2205 and SAF 2507 duplex stainless steel , In A. Turnbull (Ed.), Hydrogen Transport and Cracking in Metals, The Inst. of Materials, Cambridge, UK, p. 268-279

[3] Oltra, R. and Bouillot, C., Experimental Investigation of the Role of Hydrogen in Stress Corrosion Cracking of Duplex Stainless Steels , Hydrogen transport and cracking in metals, Conf. Proceedings, The Inst. of Mater, 1994 p. 17- 26

[4] Sofronis, P., McMeeking, R. M., Numerical analysis of hydrogen transport near a blunting crack tip , Jrnl of the Mech. and Phys. of Solids 37 (3), 1989, p. 317-350
[5] Troiano, A.R., The role of hydrogen and other interstitials in the mechanical behaviour of metals , (1959 Edward De Mille Campbell Memorial Lecture), Transactions of the ASM, Vol. 52, 1960, p. 54-80
[6] Oriani, R.A., The diffusion and trapping of hydrogen in steel, Acta Metall. 18, 1970, p. 147-157.
[7] Gerberich, W.W., Marsh, J. W. Hoehn, P. G., Hydrogen induced cracking mechanism-are there critical experiments? , Hydrogen Effects in Materials, The Minerals, Metals & Materials Society, 1996, p. 539-551
[8] Sofronis et al, Hydrogen induced shear localization of the plastic flow in metals and alloys , Eur. Jrnl of Mech. and Solids, 20, 2001, p. 857-872
[9] Barnoush, A., Vehoff, H.: Electrochemical nanoindentation: A new approach to probe hydrogen/deformation interaction, Scripta Materialia 55, 2006, p. 195-198
[10] Birnbaum, H.K., Sofronis, P., Hydrogen-enhanced localized plasticity-a mechanism for hydrogen-related fracture, Mater. Sci. and Engng., A176, 1994, p. 191-202
[11] Delafosse, D. and Magnin, T.: Hydrogen induced plasticity in stress corrosion cracking of engineering systems, Engng Fracture Mech. 68, 2001, p. 693-729.
[12] Robertson, I.M.: The effect of hydrogen on dislocation dynamics , Engng Fracture Mech. 68, 2001, p. 671-692
[13] Needleman, A., A Continuum Model for Void Nucleation by Inclusion Debonding, Jrnl of Applied Mech., Vol. 54, 1987, p. 525-531.
[14] Tvergaard, V., Effect of fiber debonding in a whisker-reinforced metal, Mater. Sci. and Engng A, Vol. 125 (2), 1990, p. 203-213
[15] Liang, Y., Sofronis, P.: Toward a phenomenological description of hydrogen induced decohesion at particle/matrix interfaces , Jrnl of the Mech. and Phys. of Solids, 51, 2003, p. 1509-1531
[16] Serebrinsky, S., Carter, E.A., Ortiz, M., A quantum-mechanically informed continuum model of hydrogen embrittlement , Jrnl of the Mech. and Phys. of Solids, 52, 2004, p. 2403-2430
[17] Ahn, D. C, Sofronis., P., Dodds Jr., R., Modelling of hydrogen-assisted ductile crack propagation in metals and alloys , Int. Jrnl of Fracture, 145, 2007, p. 135-157
[18] ABAQUS, Version 6.5, Users' manual, ABAQUS Inc. 2004
[19] Olden, V., Thaulow, C., Johnsen, R., Østby, E., Berstad, T., Application of hydrogen influenced cohesive laws in the prediction of hydrogen induced stress cracking in 25%Cr duplex stainless steel , Engng Fracture Mech., 75 (8), 2008, p. 2333-2351
[20] Krom, A.H.M. , Koers, R.W.J., Bakker, A., Hydrogen transport near a blunting crack tip , Jrnl of the Mech. and Phys. of Solids, 47, 1999, p. 971-992
[21] Kumnick, A. J., Johnson, H.H., Deep trapping states for hydrogen in deformed iron, Acta Materialia , Vol. 28, 1980, p. 33-39
[22] Taha, A., Sofronis, P., A micromechanics approach to the study of hydrogen transport and embrittlement , Engng Fracture Mech. 68, 2001, p. 803-837

[23] Jiang , D.E., Carter, E.A., First principles assessment of ideal fracture energies of materials with mobile impurities: implications for hydrogen embrittlement of metals , Acta Materialia 52, 2004, p. 4801-4807

[24] Hondros, E. D., Seah, M. P. , The theory of Grain Boundary Segregation in Terms of Surface Adsorption Analogues, Metallurgical Trans. A, Vol 8A, 1977, p. 1363-1371

[25] Scheider, I., Cohesive model for crack propagation analyses of structures with elastic-plastic material behaviour – Foundations and implementation, Technical report, GKSS internal report no WMS/2000/19.

[26] ABAQUS, Version 6.3, Example problems manual, Hibbitt, Karlsson & Sorensen Inc., 2000, p. 6.1.2-1

[27] Anderson, T.L., Fracture Mechanics, Fundamentals and Application, 2. Ed., Texas, CRC Press, 1995

[28] Olden,V., Thaulow, C., Johnsen, R., Østby, E., Cohesive zone modelling of hydrogen-induced stress cracking in 25% Cr duplex stainless steel , Scripta Materialia 57, 2007, p. 615-618.

[29] Tvergaard, V., Hutchinson, J.W., The relation between crack growth resistance and fracture process parameters in elastic-plastic solids , Jrnl of Mech. Phys. and Solids, 40 (6), 1992, p. 1377-1397

[30] Camacho, G.T., Ortiz, M., Computational modelling of impact damage in brittle materials, Intern. Jrnl of Solids and Structures, 33, 20-22, 1996, p. 2899-2938

[31] Lee, Y., Gangloff, R.P., Measurement and Modelling of Hydrogen Environment-Assisted Cracking of Ultra-High-Strength Steel, Metallurg. and Mater. Trans. A, 38A, 2007, p. 2174-2190